

**SURROGATE MODELING FOR OPTIMIZING THE WING DESIGN OF A  
HAWK MOTH INSPIRED FLAPPING-WING MICRO AIR VEHICLE**

**by**

**WEI HUANG**

Submitted in partial fulfillment of the requirements for the degree of  
Master of Science

Department of Mechanical and Aerospace Engineering

**CASE WESTERN RESERVE UNIVERSITY**

January, 2023

**CASE WESTERN RESERVE UNIVERSITY**  
**SCHOOL OF GRADUATE STUDIES**

We hereby approve the thesis of

**Wei Huang**

candidate for the degree of **Master of Science**\*

Committee Chair

**Dr. Kenneth C. Moses**

Committee Member

**Dr. Roger D. Quinn**

Committee Member

**Dr. Bryan E. Schmidt**

Date of Defense

**November 8, 2022**

\*We also certify that written approval has been obtained  
for any proprietary material contained therein.

# Contents

<b>List of Tables .....</b>	<b>3</b>
<b>List of Figures.....</b>	<b>4</b>
<b>Acknowledgements .....</b>	<b>6</b>
<b>List of Abbreviations .....</b>	<b>7</b>
<b>Abstract.....</b>	<b>8</b>
<b>Chapter 1 Introduction.....</b>	<b>9</b>
1.1 Overview and Significance .....	10
1.2 Thesis Outline .....	11
<b>Chapter 2 Background .....</b>	<b>13</b>
2.1 Surrogate Modeling .....	14
2.2 <i>Manduca Sexta L.</i> Forewing Morphology .....	15
2.3 Flapping Wing Kinematics .....	16
<b>Chapter 3 Sampling Plan .....</b>	<b>17</b>
3.1 Chapter Overview .....	18
3.2 Forewing Geometry Modeling and Design Space .....	18
3.2.1 Two-Dimensional Wing Geometry.....	19
3.2.2 Three-Dimensional Wing Geometry.....	21
3.2.3 Design Space Sampling .....	25
3.3 Flapping Mechanisms .....	28
3.3.1 Biological Flapping.....	29
3.3.2 Scotch Yoke Mechanism Flapping Wing .....	36
3.3.3 Effective Airflow Velocity and Angle of Attack Calculations .....	45
<b>Chapter 4 Computational Aerodynamic Simulations .....</b>	<b>49</b>
4.1 Chapter Overview .....	50
4.2 CFD Simulation Setup .....	52
4.3 CFD Simulations on Three Flapping Cases.....	53

4.3.1 Wing Geometry and Fluid Domain Meshing.....	54
4.3.2 Fluent Setup .....	55
4.3.3 Post CFD Calculations .....	56
4.3.4 Grid Sensitivity Analysis .....	57
4.3.5 CFD Results for Three Flapping Cases .....	58
4.4 Training Data Experiments .....	66
<b>Chapter 5 Surrogate Modeling Approach.....</b>	<b>69</b>
5.1 Chapter Overview .....	70
5.2 Supervised Regression Learning.....	70
5.3 Quadratic Kernel Support Vector Regression Model .....	74
5.4 Optimal Wing Design using Interior Point Algorithm .....	77
<b>Chapter 6 Conclusion .....</b>	<b>82</b>
<b>Chapter 7 Future Work.....</b>	<b>87</b>
<b>Appendix A: Latin Hypercube Sampled Wing Geometries.....</b>	<b>90</b>
<b>Appendix B: CFD Results on Sampled Wing Geometries .....</b>	<b>97</b>
<b>Appendix C: Quadratic SVR Surrogate Model Results.....</b>	<b>108</b>
<b>Bibliography .....</b>	<b>112</b>



# List of Tables

<b>Table 3.1:</b> Minimum and maximum values of design space parameters.....	26
<b>Table 3.2:</b> Scotch yoke flapping mechanism parameters.....	40
<b>Table 4.1:</b> Time-average aerodynamic force comparison.....	64
<b>Table 5.1:</b> Top 3 performing surrogate models.....	73

# List of Figures

<b>Figure 1.1:</b> Diagram of design of experiment for obtaining training data.....	11
<b>Figure 3.1:</b> Two-dimensional models of forewing created using image binarization.....	19
<b>Figure 3.2:</b> Forewing mean camber as defined by surface function.....	21
<b>Figure 3.3:</b> Example airfoils created using NACA 4-digit convention.....	23
<b>Figure 3.4:</b> Three-dimensional model of forewing created after using NACA airfoils...	24
<b>Figure 3.5:</b> Completed wing geometry model.....	25
<b>Figure 3.6:</b> Latin Hypercube sampling of design space with 20 design points.....	27
<b>Figure 3.7:</b> Depiction of kinematic model variables on the wing.....	28
<b>Figure 3.8:</b> Local coordinate system defined on the wing.....	30
<b>Figure 3.9:</b> Hawk moth wingtip trajectory in hovering flight.....	32
<b>Figure 3.10:</b> Hawk moth wingtip trajectory in forward flight.....	33
<b>Figure 3.11:</b> Wing velocity results for hovering and forward flight.....	35
<b>Figure 3.12:</b> Scotch yoke flapping mechanism.....	37
<b>Figure 3.13:</b> Sweep angle comparison of engineered and hawk moth flapping.....	42
<b>Figure 3.14:</b> Scotch yoke flapping mechanism wingtip trajectory.....	43
<b>Figure 3.15:</b> Wing velocity for Scotch yoke and hawk moth hovering flight.....	44
<b>Figure 3.16:</b> Wing cross-sectional geometry in fixed frame.....	46
<b>Figure 3.17:</b> Effective airflow and angle of attacks for three flapping cases.....	47
<b>Figure 4.1:</b> Ansys Workflow.....	51
<b>Figure 4.2:</b> Fluid domain mesh structure and boundary conditions.....	54
<b>Figure 4.3:</b> Grid sensitivity results.....	58

<b>Figure 4.4:</b> Fluid velocity contour results for three flapping cases.....	59
<b>Figure 4.5:</b> CFD vertical and horizontal force results for three flapping cases.....	62
<b>Figure 4.6:</b> Vertical and horizontal force results for all sampled geometries.....	67
<b>Figure 5.1:</b> Training data set consisting of lift-to-drag ratios as the response variable...	72
<b>Figure 5.2:</b> Contours of quadratic SVR prediction on lift-to-drag ratio.....	75
<b>Figure 5.3:</b> Results of interior point optimal design search.....	79
<b>Figure 5.4:</b> Optimal wing design.....	80
<b>Figure 5.5:</b> Optimal wing design CFD results.....	81
<b>Figure 6.1:</b> Sample 11, lift-to-drag ratio optimal wing design.....	83

# Acknowledgements

To my committee members, Dr. Kenneth Moses, Dr. Roger Quinn, and Dr. Bryan Schmidt whose expertise and guidance have helped me tremendously through the course of my Master's program. The completion of this thesis would not be possible without their support. To Rhiannon Miller, who has supported me the whole way since moving to Ohio and pushed me to achieve my goals since the very beginning of the program.

I am very grateful to have friends and family who have devoted their time to show support through the completion of this work; my friend and work mentor, Douglas Marsh who has continuously supported my goals in this program, and my family members Catherine Grady, Michael Grady, Robert Towns, Vivian Towns, and Lizhu Xie who have always expressed an interest in my work and whose endless encouragement have inspired me to finish my thesis.

# List of Abbreviations

**CFD** Computational Fluid Dynamic

**DOE** Design of Experiment

**FWMAV** Flapping Wing Micro Air Vehicle

**LHS** Latin Hypercube Sampling

**MAV** Micro Air Vehicle

**MSE** Mean Squared Error

**NACA** National Advisory Committee for Aeronautics

**RGB** Red Green Blue

**RMSE** Root Mean Squared Error

**SVM** Support Vector Machine

**SVR** Support Vector Regression

# Surrogate Modeling for Optimizing the Wing Design of a Hawk Moth Inspired Flapping-Wing Micro Air Vehicle

## Abstract

by

WEI HUANG

Proving the feasibility and overall efficiency of Flapping-Wing Micro Air Vehicles (FWMAVs) over other types of MAVs is vital for their advancement. Due to their complex aerodynamics and the difficulty of building accurate models of the flying animal, assessing the flight performance and efficiency of animals and FWMAVs mimicking those animals can be a challenging task. The research presented here investigates the hawk moth (*Manduca Sexta L.*) forewing as inspiration for designing an optimal wing for a moth-scale FWMAV using a surrogate modeling approach. The design of experiment (DOE) assesses the variation in aerodynamic lift-to-drag ratio due to variations in the wing geometry parameters. Using results from the experiment as training data, the trained surrogate model is a quadratic Support Vector Regression model that can rapidly evaluate the aerodynamic lift-to-drag ratio based on the wing geometry input parameters, thus identifying local extrema within the design space.

# **Chapter 1 Introduction**

## 1.1 Overview and Significance

The growing interest in developing technology based on observations from nature has influenced researchers to implement biological mechanisms of flight into modern day Micro Air Vehicles (MAVs). Specifically, flapping wing flight mechanisms from animals are used as inspiration for developing a version of MAVs known as Flapping-Wing Micro Air Vehicles (FWMAVs). The development of FWMAVs is motivated by their practical applications in areas ranging from agriculture to surveillance to natural disaster relief. In addition, their engineered wing design and flapping mechanism advance our understanding of animal flight. As a stealthy and small flight vehicle, they introduce new methods for discreet surveillance and reconnaissance as well as robust navigation in areas affected by natural disasters.

An ongoing area of research for FWMAVs is proving its feasibility and overall efficiency as a small, stand-alone flight system that can be controlled autonomously or remotely. The main challenge in assessing this efficiency relates to the complexity of the aerodynamics of flapping wing flight. Because biological systems are complex and often hard to mimic, finding optimal designs inspired by biology can be challenging. The research done in this thesis proposes a surrogate modeling design technique to design an optimal wing for a hawk moth (*Manduca Sexta L.*) inspired FWMAV. The performance of various wing designs are investigated in Computational Fluid Dynamic (CFD) simulations that reveal the unsteady aerodynamics around the moth wing, and surrogate models trained from CFD results are used to estimate the aerodynamic performance based on the wing geometry. The trained surrogate model serves as a rapid optimization tool to determine a lift optimal wing design.



## 1.2 Thesis Outline

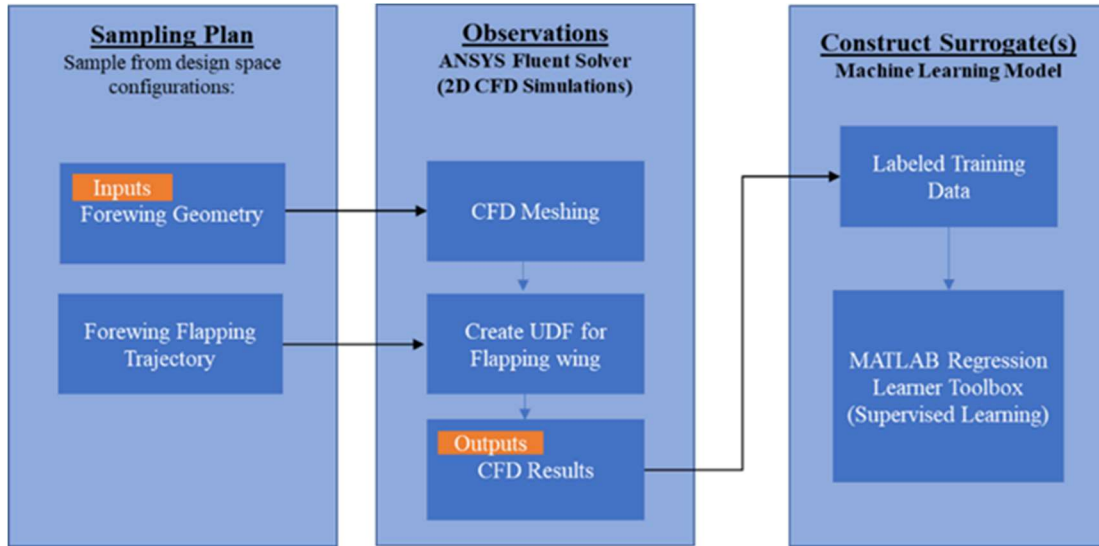


**Figure 1.1:** Diagram showing the design experiment for obtaining training data for constructing a surrogate model. The experiment starts by sampling a configuration of parameters that define the geometry of the moth wing and ends with an observation of aerodynamic simulation results.

The structure of this thesis is organized according to the design of experiments (DOE) presented in Fig. 1.1. Chapter 2 provides an introductory background into modern the field of surrogate modeling and how it is used in aerospace engineering. A literature review is done in Chapter 2 that outline research done on the morphology of the hawk moth forewing and kinematic modeling of the wing flapping motion.

In Chapter 3, a sampling plan is created to obtain input data into the CFD simulations. The results from morphological studies done by [1] and flapping kinematic studies done by [6] are used to model the wing geometry and flapping kinematics of the forewing. The process of generating a 3D forewing model is discussed in detail, and the design space of the wing is defined. Through a Latin Hypercube Sampling method, 20 different wing design configurations are considered, and their geometries are imported

into the CFD simulation. The end of Chapter 3 consists of comparisons done on the flapping motion of the hawk moth wing in hovering flight and forward flight, and the flapping motion of the wing using a Scotch yoke mechanism.

In Chapter 4, the CFD simulations performed in this thesis are discussed in detail. A setup of the CFD simulation in Ansys and relevant information about the Fluent solver are presented. The results from the three flapping cases discussed in Chapter 3 are compared with relevant CFD research conducted by other researchers in this field. At the end of Chapter 4, CFD results from the wing geometry samples taken in Chapter 3 are presented and their results are discussed.

In Chapter 5, the lift-to-drag ratios are calculated and used as the performance metric for each of the sampled wing design, and the results are used as the response variable data for supervised regression model training. Finally, in Chapters 6 and 7 conclusions are made about the observed results in each of the sections, and the objectives for future work are discussed.

## **Chapter 2 Background**

## 2.1 Surrogate Modeling

Limitations on the amount of known experimental data available for flapping wing aerodynamics and the cost of conducting wind tunnel experiments prove to be significant design challenges for developing fully flight capable FWMAVs. Because of this, assessing off-design points for FWMAV systems can become a tedious iterative design process that can sometimes lead to unsatisfactory results. To address this, the surrogate modeling approach allow engineers to inquire information about off-design points in a quick manner without the need for expensive simulated or real-world experiments.

Aerodynamic optimization commonly utilizes the surrogate modeling approach as a rapid design optimization technique. When CFD simulations or wind tunnel simulations become costly, surrogate models are used as a computationally inexpensive method for predicting the results of an expensive simulation based on previous data observed in the real experiment. Although aerodynamic optimization can be achieved through CFD-based optimization and is inexpensive compared to wind tunnel testing, modeling a full simulation involving flapping-wing aerodynamics is extremely difficult and can still take days or weeks to run on supercomputers.

In [12], Du et al. trained a neural network-based surrogate model on optimizing the shape parameters of an airfoil design. The model trained is a rapid prediction model capable of estimating both scalar and vector response variables from the CFD simulations such as the lift and pressure distribution on an airfoil in varying flow regimes. The surrogate model from that study was able to rapidly determine an optimal design point for

aerodynamic quantities that agreed well with results obtained from CFD-based optimization.

For studies done on flapping wing aerodynamic optimization, one notable work done by Trizila et al. in [13] developed surrogate models used to predict the aerodynamic efficiency of a 2D and 3D flapping wing in hovering flight. The design space consists of kinematic parameters such as plunge altitude and angular amplitude, and the models are trained using ensembles of machine learning models to predict aerodynamic coefficients. The results from their surrogate models showed that in 3D flapping wing flight, lift forces are more influenced by the phase lag of the wing, while in 2D the angular amplitude impacted the lift force more.

## **2.2 *Manduca Sexta L.* Forewing Morphology**

The hawk moth forewing is a thin wing structure consisting of venation structures spanning from the root of the wing to the tip. The leading edge of the wing is made up of the most venation lines that are thicker than the ones spanning to the trailing edge. Additionally, observations made in [4] on the cross-sectional geometry of the forewing showed it is not symmetric about a chord line from the leading ledge to the trailing edge, but rather it has a decently large camber located about 50% down the chord length at approximately 2 mm from the root of the wing. The morphology of the hawk moth forewing was heavily studied by O'Hara et al. in both [1] and [2]. The physical properties of a sample of 30 hawk moth forewings were analyzed and recorded. O'Hara's work reported on the sample statistics and identified important properties of the wing such as the mean camber. Revealed in their work were the average mass, wingspan, max chord, and surface area of the wings along with their variance. These results are instrumental in

developing finite element structural models and hawk moth inspired wings for future FWMAVs. For this thesis, the inclusion of O'Hara's results is an important step for modeling an engineered forewing for investigation in a CFD simulation.

## **2.3 Flapping Wing Kinematics**

Defined in [6], the flapping kinematics of wing can be described by a four degree-of-freedom biomechanism that describe both the trajectory of the wingtip and the orientation of the wing. The 4 variables that describe the flapping kinematics are the stroke plane angle, sweep angle, elevation angle, and rotational angle which changes most aggressively during pronation and supination. These variables are better defined later in Chapter 3. Using a wind tunnel and high-speed camera set up, the work done by Willmott et al. in [6] investigated the 4 kinematic variables for hovering and forward flight. Their results showed consistent trends in the variables, but the magnitude of the variables varied as flight velocity changed. In this thesis, the results of the kinematic variables presented in [6] are used to model the hovering flight and forward flight wing kinematics for the CFD simulations.

# Chapter 3 Sampling Plan

### **3.1 Chapter Overview**

The variation in aerodynamic performance of the hawk moth is being investigated as its wing geometry is changed. A process using both biological data and engineered modeling is implemented to create 3D geometries of the hawk moth forewing. This process allows for rapid generations of the wing geometry for testing in an aerodynamic simulation. Afterwards, flapping kinematics of the wing are investigated, and equations are derived for use in the aerodynamic simulation software. Both the wing geometry modeling and flapping kinematic modeling process discussed in this chapter serve as the vital first steps for defining conditions in the aerodynamic simulation.

### **3.2 Forewing Geometry Modeling and Design Space**

Contemporary research characterizing the aerodynamics of flapping-wing flight within a CFD simulation use simple models for the cross section of the wing such as a flat plate or other types of symmetrical cross section geometry. However, the cross section of the moth forewing more closely resembles that of an asymmetric airfoil. The 3D geometry modeling of the forewing is accomplished using a combination of image processing and NACA airfoil equations. By parameterizing the cross-sectional geometry with NACA 4-digit airfoils, a 3D wing geometry can be modeled to resemble that of the hawk moth forewing which has thick venation structures near the leading edge and a camber. The wing geometry parameters discussed in this thesis define the design space of the wing. The bounds of the design space are defined, and sample geometries are acquired through a Latin Hypercube Sampling technique.



### 3.2.1 Two-Dimensional Wing Geometry

A 2D wing geometry is created by implementing an image digitalization technique on the image taken by [1]. First an RGB image of the forewing is converted into a grayscale version. Then, using an image binarization method, each pixel in the grayscale image of the wing is converted into a one or zero based on a defined threshold value on the grayscale magnitude. The pixel values on a grayscale image range between 0 to 255 with 0 representing black and 255 representing white. For any pixel value less than the threshold value, zero is assigned to that pixel, and one is assigned to pixel values greater than the threshold. Using this method, a 2D point cloud outlining the venation structure and the geometry of the forewing is created. Finally, based on the desired wingspan ( $R$ ) and chord length ( $C$ ) of the modeled forewing, the point cloud is rescaled to fit within the bounds of the wingspan and chord length.

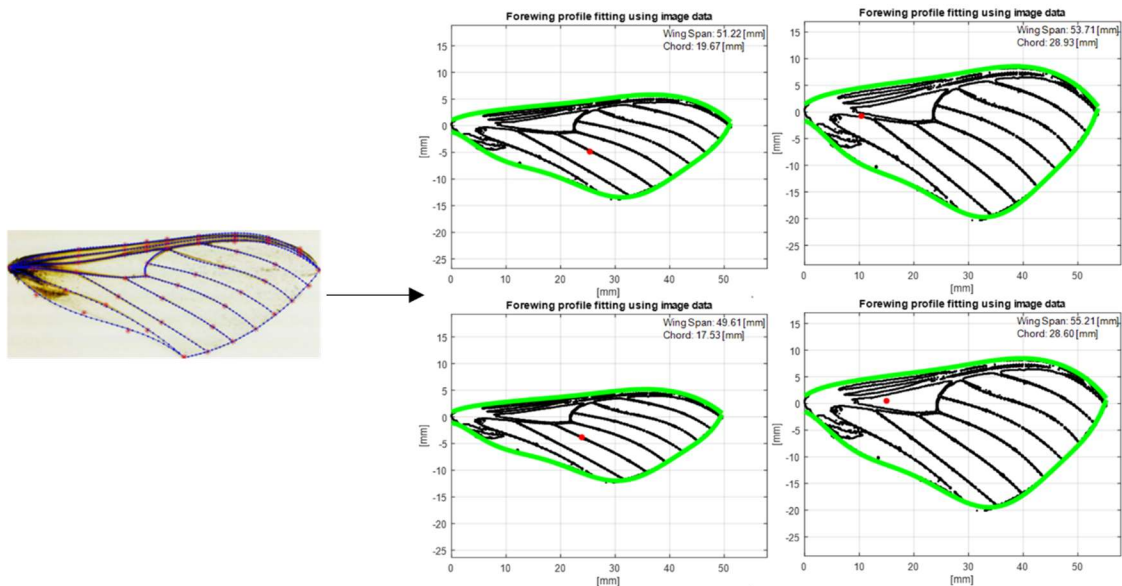


**Figure 3.1:** Image of hawk moth forewing used for image binarization [1]. 2D models of the wing are created based on desired wingspan and max chord length. Permission was obtained from O’Hara to use the picture from [1].

The process depicted in Fig 3.1 shows the image binarization method used to create a 2D point cloud of the wing. By filtering out the point cloud coordinates associated with the leading and trailing edges of the wing, a profile of the 2D wing can be defined using 6<sup>th</sup> order polynomial functions fitted to the leading and trailing edge points. Depicted in Fig 3.1, four samples of a 2D wing were created with varying wingspan and chord lengths using the process described. The bounds of the two parameters are the maximum and minimum wingspan and chord lengths among the 30 samples of the biological forewing collected in [1].

The shape of the forewing is a complicated structure that cannot be modeled simply with two dimensional geometric parameters such as wingspan, chord length, and the leading and trailing edge profiles. While the wing is still attached to the abdomen of the moth, a camber plane exists that extends the shape of the wing into three dimensions. Measurements of the three-dimensional camber plane are taken in [1] using a 3D coordinate measurement arm and a laser scanning system. Using samples of the scan, a mean camber plane is defined by a surface function fitted to a 3D point cloud of the forewing. This mean camber provides a baseline for modeling the thickness of the wing using NACA 4-digit airfoils.

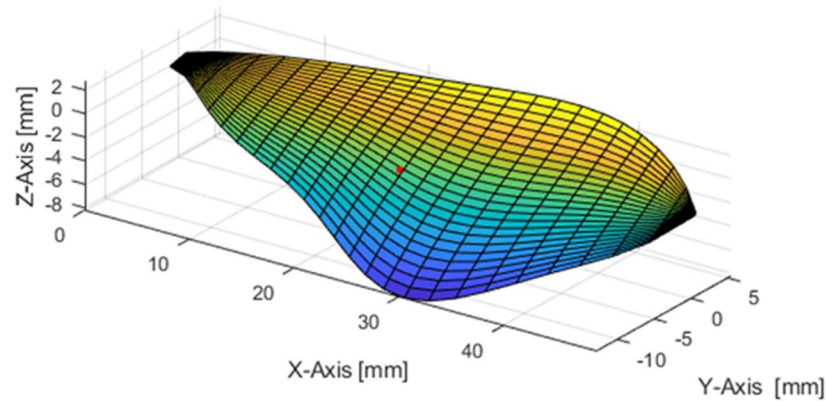


**Figure 3.2:** Forewing mean camber plane defined by a surface function [1]. The wing depicted has a wingspan ( $R$ ) of 48.26 [mm] and a max chord length ( $C$ ) of 17.65 [mm].

### 3.2.2 Three-Dimensional Wing Geometry

On the hawk moth, the cross section of the forewing consists of thick venation structures at the leading edge and a camber line. The venation structures decrease in thickness along the span and chord of the wing. The thickest structure of the wing is located at the root and the thinnest at the tip of the wing. To mimic this thickness variation, the engineered cross section of the wing is modeled after NACA 4-digit airfoils. NACA airfoils are a series of aircraft wing cross section shapes developed by NACA in the late 1920s. A series of 4-digit airfoils as first developed and tested in wind tunnel experiments by [5]. Each number within the 4-digit series describes the geometric properties of the wing cross section such as its camber profile and thickness. Similar to the biological structure of the forewing cross section, the NACA airfoils can be parameterized such that the leading edge has a greater cross-sectional thickness than the

trailing edge. The NACA 4-digit airfoils are defined by the maximum camber (M) as a percentage of the chord length, the position of maximum camber (P) as P/10 of the chord length, and the max airfoil thickness (XX) as a percentage of the chord length.

For a NACA MPXX airfoil, the geometry can be defined by first formulating a function for the camber of the wing. The camber function on a normalized chord length domain  $x \in [0,1]$  can be represented as a piecewise function.

$$f_c(x) = \begin{cases} \frac{m}{p^2}(2px - x^2), & \text{if } 0 \leq x < p \\ \frac{m}{(1-p)^2}(1 - 2p + 2px - x^2), & \text{if } p \leq x \leq 1 \end{cases} \quad (3.1)$$

Additionally, the rate of change of the camber function with respect to the chord length is

$$\frac{df_c(x)}{dx} = \begin{cases} \frac{2m}{p^2}(p - x), & \text{if } 0 \leq x < p \\ \frac{2m}{(1-p)^2}(p - x), & \text{if } p \leq x \leq 1 \end{cases} \quad (3.2)$$

The thickness distribution function defines the cross-section thickness variation along the chord length. Along the same chord length domain  $x$  the thickness distribution function can be expressed as

$$f_T(x) = \frac{T}{0.2}(a_0x^{0.5} + a_1x + a_2x^2 + a_3x^3 + a_4x^4) \quad (3.3)$$

$$a_0 = 0.2969, \quad a_1 = -0.126, \quad a_2 = -0.3516, \quad a_3 = 0.2843, \quad a_4 = 0.1036$$

The geometric parameters  $m$ ,  $p$ , and  $T$  in equations 3.1-3.3 are each associated with the 4-digit designations assigned to NACA airfoils. In the equations,

$$m = \frac{M}{100}, \quad p = \frac{P}{10}, \quad T = \frac{XX}{100}$$

From Equations 3.1-3.3, expressions for the lower and upper surface profile of the airfoil can be defined. The surface profiles are generated along the camber line and their distances from the camber line are determined by the thickness distribution function

along the chord. First, an angle  $\theta$  is expressed as the angle of the camber slope along the chord length.

$$\theta = \tan^{-1} \left( \frac{df_c(x)}{dx} \right) \quad (3.4)$$

Then, combining the slope angle in equation 3.4 and both equations 3.1 and 3.3, the profile for upper and lower surfaces of the airfoil can be determined as

$$x_u = x - f_T(x) \sin(\theta), \quad y_u = f_c(x) + f_T(x) \cos(\theta) \quad (3.5)$$

$$x_l = x + f_T(x) \sin(\theta), \quad y_l = f_c(x) - f_T(x) \cos(\theta) \quad (3.6)$$

with equation 3.5 representing the functions for the upper surface profile and 3.6 for the lower surface. This method of parameterizing the cross section allows for a smooth process of generating a wing cross section profile at each local chord length of the 2D wing. In Fig. 3.3, three NACA airfoils are generated using the method described in this section.

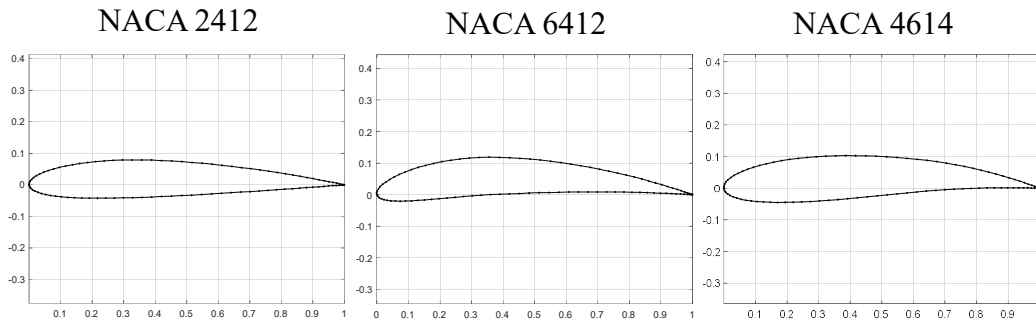


**Figure 3.3:** Example of airfoils modeled using NACA 4-digit convention [5].

The chord length parameter ( $C$ ) described in Section 3.1.1 refers to the maximum chord length of the forewing. That parameter itself, however, does not properly define the variation in chord length on the wing from the root to the wingtip. From where the model

of the wing was left off in Fig. 3.2, the variation in the chord length along the wingspan is defined as the distance between the leading edge and trailing edge profile of the wing that was modeled using 6<sup>th</sup> order polynomial functions. Given this length, the airfoil geometry equations developed in Equations 3.1 to 3.6 can be scaled to fit the variation in chord length at each local chord length. Additionally, the decrease in the thickness of the wing cross section from the root to the tip is implemented by a thickness rate of change along the wingspan constant  $\frac{dT}{dR}$ . This process is depicted in Fig. 3.4

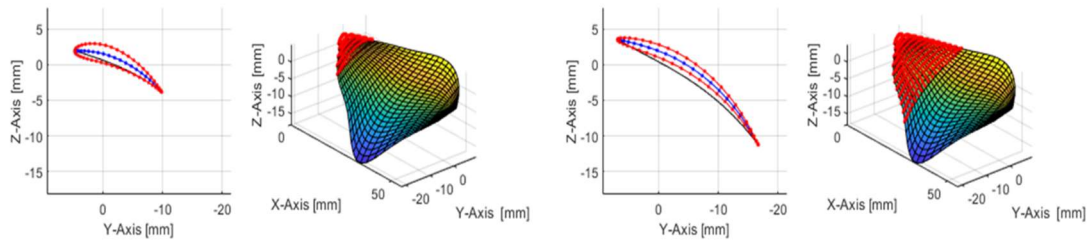


**Figure 3.4:** Three-dimensional wing cross-sectional geometry along the wingspan using 4-digit NACA airfoil parameterization.

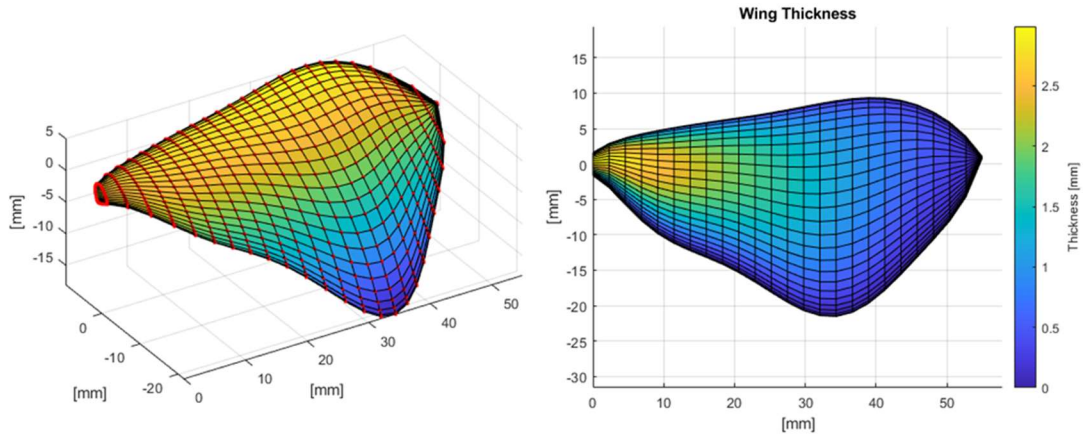


**Figure 3.5:** Final wing geometry designed using the geometry parameterization methods discussed in this section. The image on the right show the thickness distribution of the wing after modeling the cross-sectional geometry using NACA airfoils.

The 3D wing model depicted in Fig. 3.4 and 3.5 has a wingspan  $R = 54.95 [mm]$ , maximum chord length  $C = 31.66 [mm]$ , max camber of  $M = 6\%$  of the local chord length, max camber position of  $P = 40\%$  of the local chord length, and a maximum thickness of  $T = 3 [mm]$ . Using these 5 geometric parameters, different variations of the engineered forewing geometry can be generated and tested in a computational fluid dynamic simulation environment to assess its performance.

### 3.2.3 Design Space Sampling

The design space parameters discussed in this thesis are the geometric parameters defined in sections 3.1.1 and 3.1.2 that model the engineered forewing. To ensure that the engineered wing resembles the biological wing, the range of the wingspan  $R$  and max chord length  $C$  are chosen as the maximum and minimum lengths of the sample of biological wings collected by [1]. The range of the cross-sectional geometry variables are

chosen to model realistic 3D wing designs with the thickest portion of the wing at the root and leading edge.

**Table 3.1:** Minimum and maximum values of design space parameters

<b>Design Space Parameters</b>		
<b>Parameter</b>	<b>Minimum</b>	<b>Maximum</b>
Wingspan ( $R$ )	42.59 [mm]	57.85 [mm]
Max Chord Length ( $C$ )	16.64 [mm]	32.83 [mm]
Max Camber ( $M$ )	0%	9%
Max Camber Location ( $P$ )	30%	70%
Max Thickness ( $T$ )	3 [mm]	6 [mm]

Running computational fluid dynamic simulations can be an expensive process both in terms of time and the computer hardware requirement. On top of that, the aerodynamic mechanisms involved in flapping wing flight consists of unsteady airflows that add on to the complexity of the simulation. As such, a Latin Hypercube Sampling (LHS) technique is used to reduce the number of simulations that need to be run while including sample points from a wide range in the design space [14]. This is a controlled random sampling method that attempts to reflect the entire data set within the design space with a small sample size.



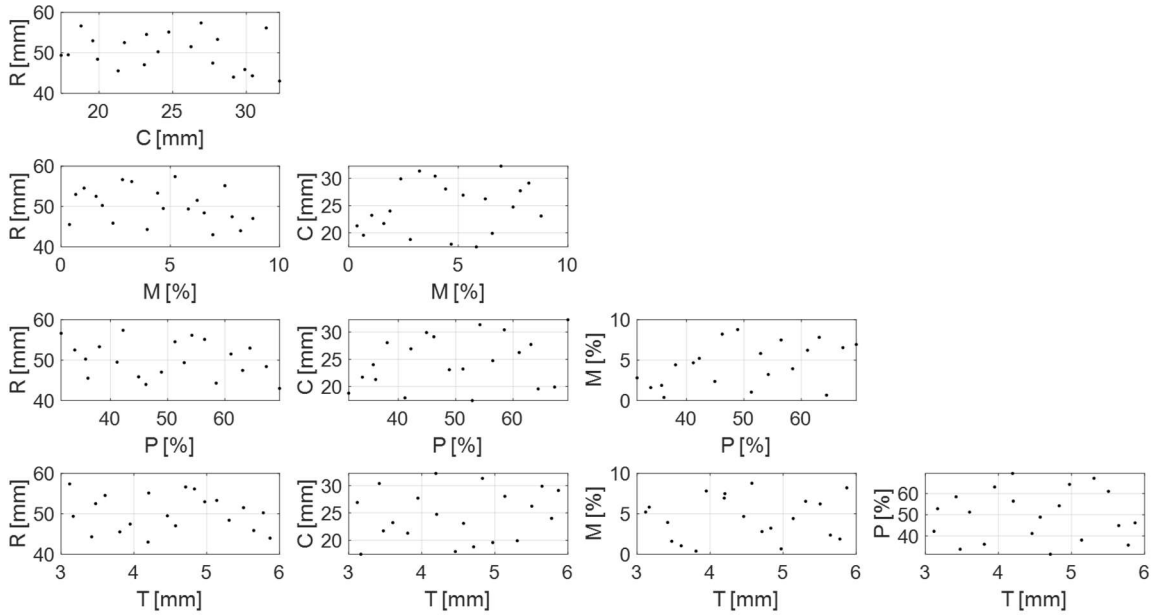


**Figure 3.6:** Latin Hypercube Sampling of design space with 20 sampled points.

Fig. 3.6 depicts the sampled design space points that define the three-dimensional geometry of 20 configurations of engineered forewings. The shape of the forewings can be seen in Appendix A. For continuous design variables and 20 sampled points, Latin Hypercube Sampling evenly partitions the design space into 20 regions across each dimension. Then, a random sample is picked within the 20 divided regions along each dimension separately. Finally, the samples taken from each dimension are combined randomly into coordinates in the hypercube. This method of sampling results in a rapid and more accurate estimation of true simulation results because of the spread and number of sample points. Appendix A includes all the generated geometry at each sample point and the 2D wing section geometry of the wing that is to be tested in the CFD simulation.

### 3.3 Flapping Mechanisms

Before the CFD simulations can proceed, kinematic equations that describe the motion of the wing relative to its body must be derived. The kinematic equations derived in this section are then used to describe the mesh motion within the CFD simulation. These equations are defined by 4 coordinate variables that describe the trajectory of the wingtip and the orientation of the wing relative to a fixed reference frame. Depicted in Fig. 3.7, the coordinate variables are the stroke plane angle ( $\beta$ ), wing elevation angle with respect to the stroke plane ( $\theta$ ), the sweep angle within the stroke plane ( $\phi$ ), and finally, a rotational angle ( $\alpha$ ) that describes the orientation of the wing about the wingtip axis. The wingtip axis in the kinematic models derived is defined as a rotational axis from the root of the wing to the tip.

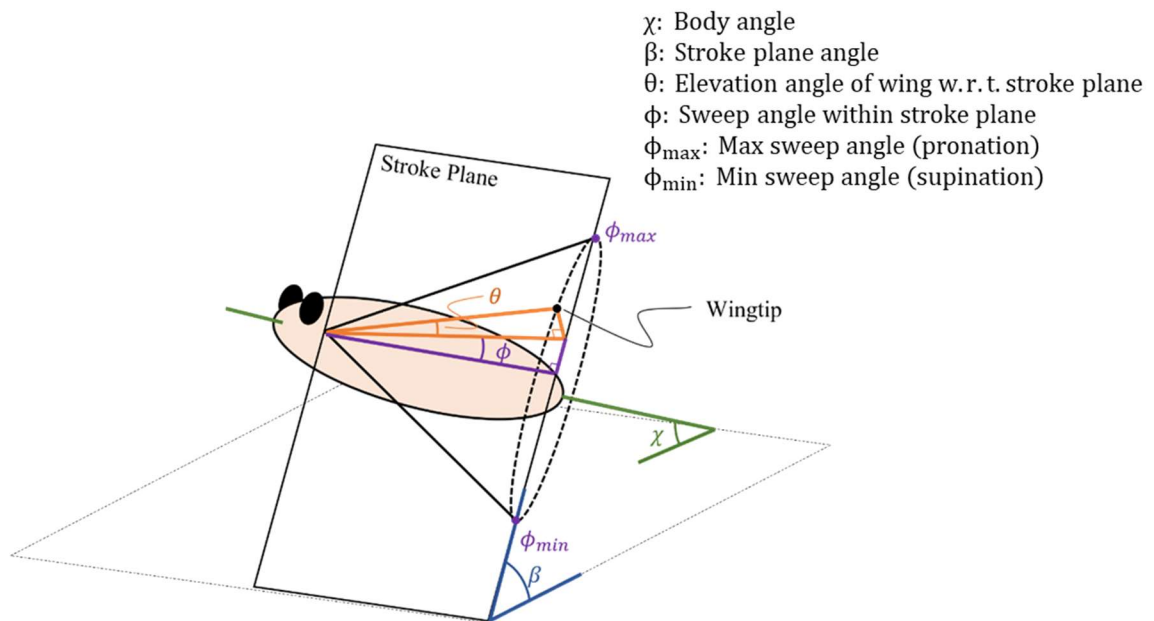


**Figure 3.7:** The flapping kinematic variables as depicted on the moth. [6]

Section 3.3 of this thesis include derivations of the kinematic equations for the wing motion using both biological data obtained from [6] and the engineered Scotch yoke flapping mechanism developed by [10]. The Scotch yoke flapping mechanism is configured to mimic the biological wing motion data for hovering flight obtained from [6]. A comparison of the two types of flapping motions in 2D is performed and used to gain a better understanding of the CFD results in Chapter 4.

For the purpose of investigating the aerodynamics at a specified cross-sectional geometry along the wingspan, the 3D kinematic motions are simplified to 2D. Although the aerodynamics around a 3D geometry can be investigated with the kinematic equations presented in this section and the geometry in Section 3.1, three-dimensional CFD simulations are beyond the scope of this thesis. However, the 3D geometry created in Section 3.1 remains a critical step in parameterizing the 2D geometry as parameters such as wingspan and wing thickness affect the 2D geometry being tested in the CFD simulation.

To conclude this section, the effective airflow velocity and angle of attack for each of the three cases are compared and used as an initial insight into the aerodynamic mechanisms around the wing that is to be observed in Chapter 4.

### **3.3.1 Biological Flapping**

A study done on the mechanics of flight in the hawk moth [6] investigated the kinematics of hovering and forward flight using a wind tunnel and an airflow visualization setup. A feeder placed inside the wind tunnel acted as a stimulus for the moth and kinematic variables are observed using two high speed cameras placed inside the test area. Using the same kinematic modeling as depicted in Fig. 3.7, researchers in

[6] measured both the body angle ( $\chi$ ) and stroke plane angle ( $\beta$ ) from a fixed reference frame. The sweep angle ( $\phi$ ) is measured tangent to the stroke plane and the elevation angle ( $\theta$ ) measured normal to the stroke plane. Finally, the rotation angle of the wing is measured relative to the stroke plane. Using the kinematic variables measured from [6] for hovering flight and forward flight at a velocity of 2.1 m/s, the wingtip trajectory and orientation of the wing geometry described in Section 3.1 can be defined.

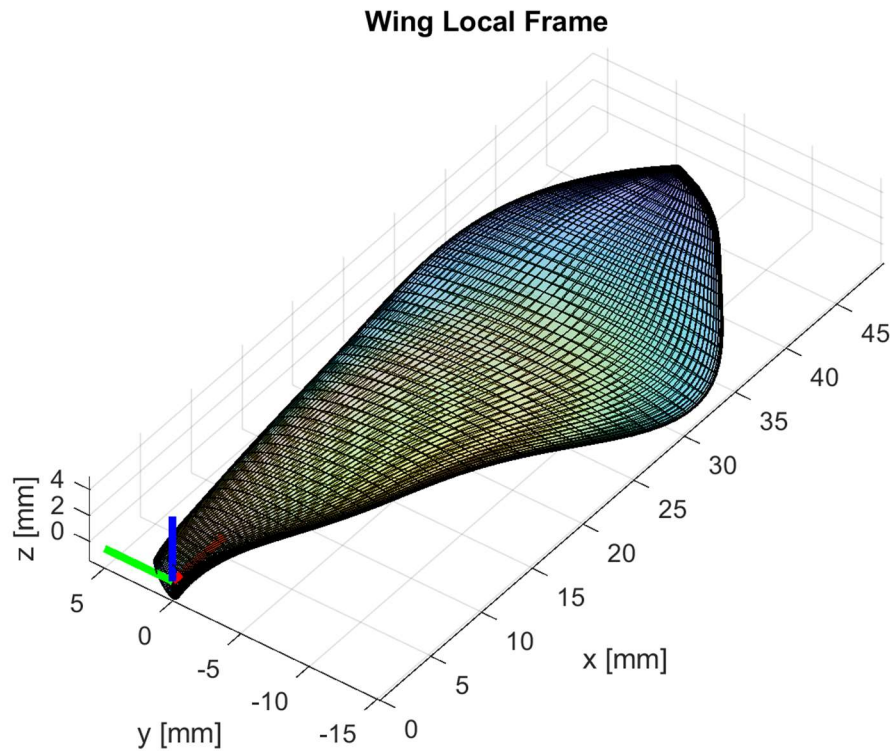


**Figure 3.8:** Local coordinate system on the wing with the origin located at the root.

The motion of the 3D wing geometry can be described by first defining a wing local frame as depicted in Fig. 3.8 and then using a series of rotational matrices associated with the kinematic variables as a coordinate transform from the wing local

frame to the fixed frame. The origin of the wing local frame is located at the root of the wing. The local z-axis points toward the wing surface, local x-axis points toward the wingtip, and local y-axis is the cross product of the z-axis with the x-axis. The wingtip vector points in the direction of the local x-axis and has a magnitude of the wingspan. A transformation between this local frame and the fixed frame can be defined by the coordinate transform below.

$$\vec{r}_{l,i} = [R_1(\beta(t))][R_2(\phi(t))][R_3(\theta(t))][R_1(\alpha(t))]\vec{r}_{w,i} \quad (3.7)$$

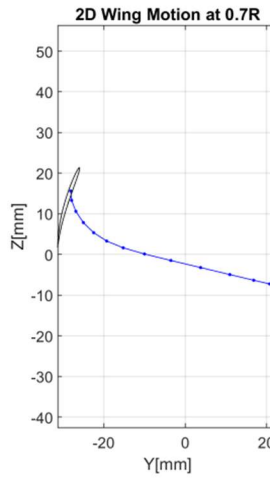
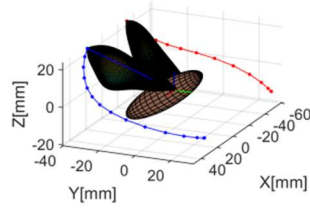
In Equation 3.7,  $[R_k(x(t))]$  is the rotation matrix about the  $k^{th}$  axis defined by the time dependent variable  $x(t)$ . The vector,  $\vec{r}_{l,i}$  is the coordinate of the  $i^{th}$  element on the wing in the fixed frame. Finally, the vector  $\vec{r}_{w,i}$  is the coordinate of the same  $i^{th}$  element of the wing in the wing local frame. Suppose the 2D wing element being investigated in the CFD simulation is located at a length of  $n$  percent of the whole wingspan. Assuming the wing is a rigid body, the trajectory of any element along the wingspan can be described with the following set of equations for wing position in the fixed frame.

$$\vec{r}_{l,n} = \frac{n}{100} R \begin{bmatrix} \cos(\theta) \cos(\phi) \\ \sin(\theta) \cos(\beta) + \cos(\theta) \sin(\phi) \sin(\beta) \\ \sin(\theta) \sin(\beta) - \cos(\theta) \sin(\phi) \cos(\beta) \end{bmatrix} \quad (3.8)$$

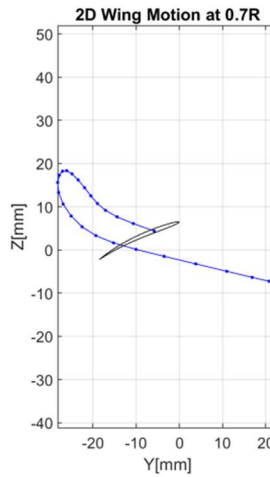
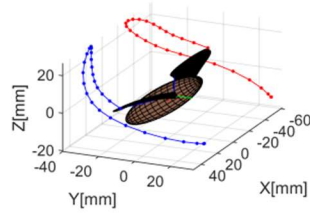
Simplified into two-dimensions in the y-z frame, Equation 3.8 becomes

$$\vec{r}_{l,n} = \frac{n}{100} R \begin{bmatrix} \sin(\theta) \cos(\beta) + \cos(\theta) \sin(\phi) \sin(\beta) \\ \sin(\theta) \sin(\beta) - \cos(\theta) \sin(\phi) \cos(\beta) \end{bmatrix} \quad (3.9)$$

Simulation Time: 0.0140 [sec]  
 Body Angle: 33.9 [deg]  
 Stroke Plane Angle: 23.4 [deg]  
 Elevation Angle: 5.2 [deg]  
 Sweep Angle: 70.2 [deg]  
 Rotation Angle: 91.0 [deg]  
 Forward Flight Velocity: 0.0 m/s



Simulation Time: 0.0260 [sec]  
 Body Angle: 33.9 [deg]  
 Stroke Plane Angle: 23.4 [deg]  
 Elevation Angle: 2.8 [deg]  
 Sweep Angle: 14.2 [deg]  
 Rotation Angle: 67.2 [deg]  
 Forward Flight Velocity: 0.0 m/s



Simulation Time: 0.0360 [sec]  
 Body Angle: 33.9 [deg]  
 Stroke Plane Angle: 23.4 [deg]  
 Elevation Angle: 3.5 [deg]  
 Sweep Angle: -37.9 [deg]  
 Rotation Angle: 72.2 [deg]  
 Forward Flight Velocity: 0.0 m/s

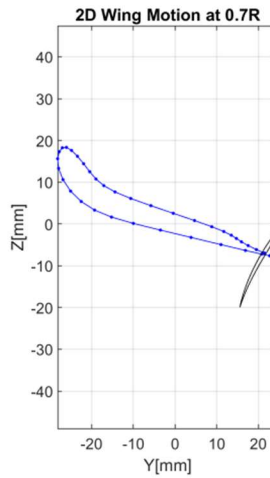
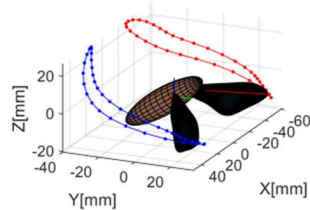
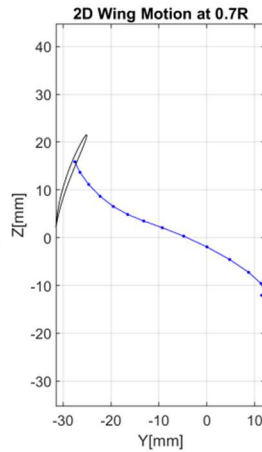
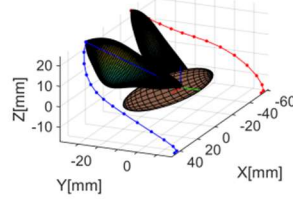
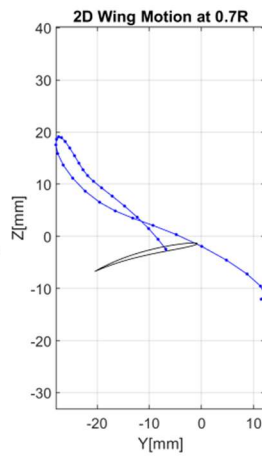
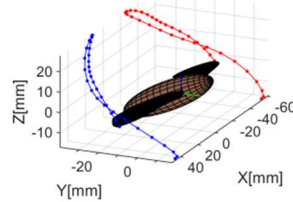


**Figure 3.9:** Hawk moth wingtip trajectory in hovering flight. Kinematic variables measured in [6].

Simulation Time: 0.0140 [sec]  
 Body Angle: 25.8 [deg]  
 Stroke Plane Angle: 37.6 [deg]  
 Elevation Angle: -7.0 [deg]  
 Sweep Angle: 68.6 [deg]  
 Rotation Angle: 105.0 [deg]  
 Forward Flight Velocity: 2.1 m/s



Simulation Time: 0.0320 [sec]  
 Body Angle: 25.8 [deg]  
 Stroke Plane Angle: 37.6 [deg]  
 Elevation Angle: -10.1 [deg]  
 Sweep Angle: 9.0 [deg]  
 Rotation Angle: 71.2 [deg]  
 Forward Flight Velocity: 2.1 m/s



Simulation Time: 0.0400 [sec]  
 Body Angle: 25.8 [deg]  
 Stroke Plane Angle: 37.6 [deg]  
 Elevation Angle: -3.3 [deg]  
 Sweep Angle: -26.3 [deg]  
 Rotation Angle: 95.9 [deg]  
 Forward Flight Velocity: 2.1 m/s

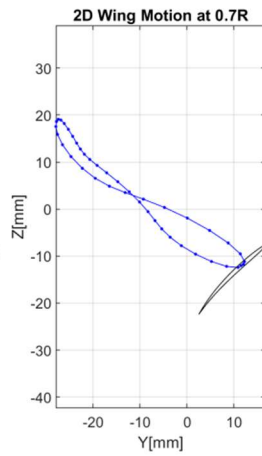
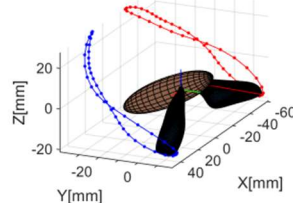


**Figure 3.10:** Hawk moth wingtip trajectory in forward flight. Kinematic variables measured in [6].

With the wingtip trajectory and orientation of the wing properly defined in Equations 3.8 and 3.9, the wing motion of the moth in both hovering flight (Fig. 3.9) and forward flight (Fig. 3.10) can be visualized in both 3D and 2D. For hovering flight, the stroke plane angle is set at a constant  $23.4^\circ$ , sweep angle ranges from  $-42.2^\circ$  to  $70.2^\circ$ , elevation angle ranges from  $-16.3^\circ$  to  $9.7^\circ$ , and rotational angle at 70% of the wingspan ranges from  $47^\circ$  to  $151^\circ$ . For forward flight velocity of 2.1 m/s, the stroke plane angle is set at a constant  $37.6^\circ$ , sweep angle ranges from  $-26.3^\circ$  to  $69.2^\circ$ , elevation angle ranges from  $-11.6^\circ$  to  $3.1^\circ$ , and rotational angle at 70% of the wingspan ranges from  $58^\circ$  to  $153^\circ$ .

Results from the work done in [6] indicate that the hawk moth showed a tendency to increase its stroke plane,  $\beta$  as its forward flight velocity increased. For hovering flight, the stroke plane angle ranged between  $10^\circ$  and  $30^\circ$ , whereas this angle ranged between  $50^\circ$  and  $60^\circ$  for the highest measured forward flight speed of 5 m/s. The wing velocity in the fixed frame is derived under the assumption that the wingtip trajectory is at a constant stroke plane angle for constant forward flight velocities. The stroke plane angles in the kinematic model are the average of the measured stroke plane angles among each moth specimen in [6] for different forward flight velocities. Under the assumption of constant stroke plane angle, the velocity of the wing motion can be expressed as

$$\vec{v}_n = \frac{n}{100} R \begin{bmatrix} \dot{\theta}(\cos(\theta) \cos(\beta) - \sin(\theta) \sin(\phi) \sin(\beta)) + \dot{\phi} \cos(\theta) \cos(\phi) \sin(\beta) \\ \dot{\theta}(\cos(\theta) \sin(\beta) - \sin(\theta) \sin(\phi) \cos(\beta)) + \dot{\phi} \cos(\theta) \cos(\phi) \cos(\beta) \end{bmatrix} + \begin{bmatrix} v \\ 0 \end{bmatrix} \quad (3.10)$$



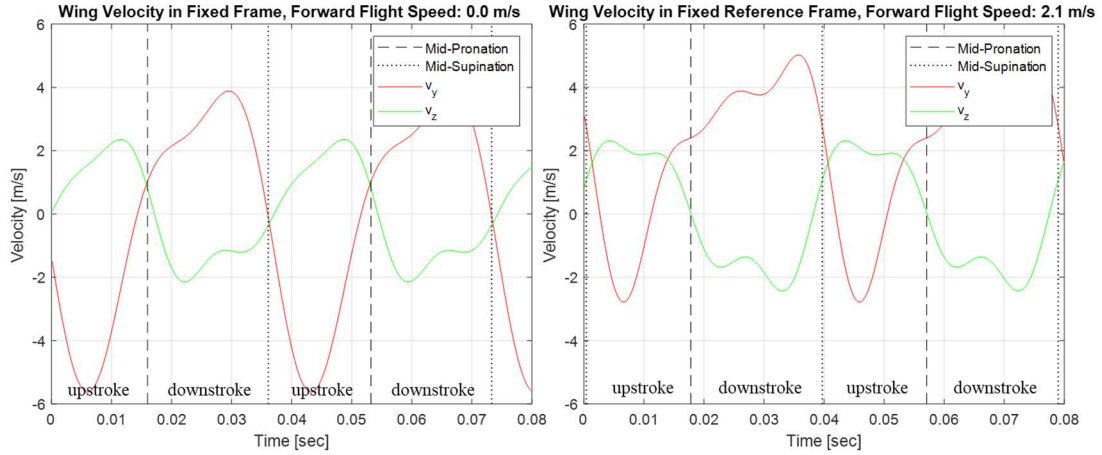


**Figure 3.11:** Wing velocity results for hovering flight and forward flight velocity of 2.1 m/s. Lines indicating mid-pronation and mid-supination separate the upstroke and downstroke trajectories. The plots show velocity components near 0 m/s for hovering flight and 2.1 m/s for forward flight during mid-pronation and mid-supination.

Equation 3.10 models the velocity ( $\vec{v}_n$ ) of the wing at an airfoil element located  $n\%$  down the wingspan ( $R$ ) by taking the first-order time derivative of Equation 3.9 and adding the forward flight velocity,  $v$  in the positive  $y$  direction.  $\theta$ ,  $\dot{\theta}$ ,  $\phi$ , and  $\dot{\phi}$  are the elevation and sweep angles measured in [6], and their respective time rates of change. From the results in Fig. 3.11, initial intuitions about the velocity of the wing are validated. As the wing trajectory transitions from upstroke to downstroke and vice versa, the speed of the wing is expected to approach 0 m/s or the forward flight speed. This is evident in the hovering flight plot as mid-supination and mid-pronation occurs at points where the  $y$  and  $z$  velocity components intersect, and the point of intersection is near 0 m/s as there is no forward flight velocity. For a forward flight velocity of 2.1 m/s, this trend is not as evident because the intersection points do not occur during mid-pronation and mid-supination. However, the transition between upstroke and downstroke does occur when the wing velocity is near 2.1 m/s. This is a consequence of the asymmetric

shape of the flapping trajectory and where the mid-supination and mid-pronation points are defined in the trajectory.

### **3.3.2 Scotch Yoke Mechanism Flapping Wing**

To compare the performance of an engineered flapping mechanism with the moth's flapping, the Scotch yoke flapping mechanism developed by [10] is configured to mimic the biological flapping trajectory of the wingtip in [6] for hovering flight. Depicted in Fig. 3.12, the flapping mechanism consists of two shoulder joints (blue), one rotation crank (red) actuated by a motor, and a yoke (black) that converts the rotational motion of the crank to a flapping motion on the wing. At each shoulder joint, linear springs are attached to shoulder arm and the yoke to aid in the stroke reversal of the wing. This mechanism was successfully implemented by [10] and showed improved results in mimicking the flapping motion on the hawk moth compared to a crank-slider mechanism.

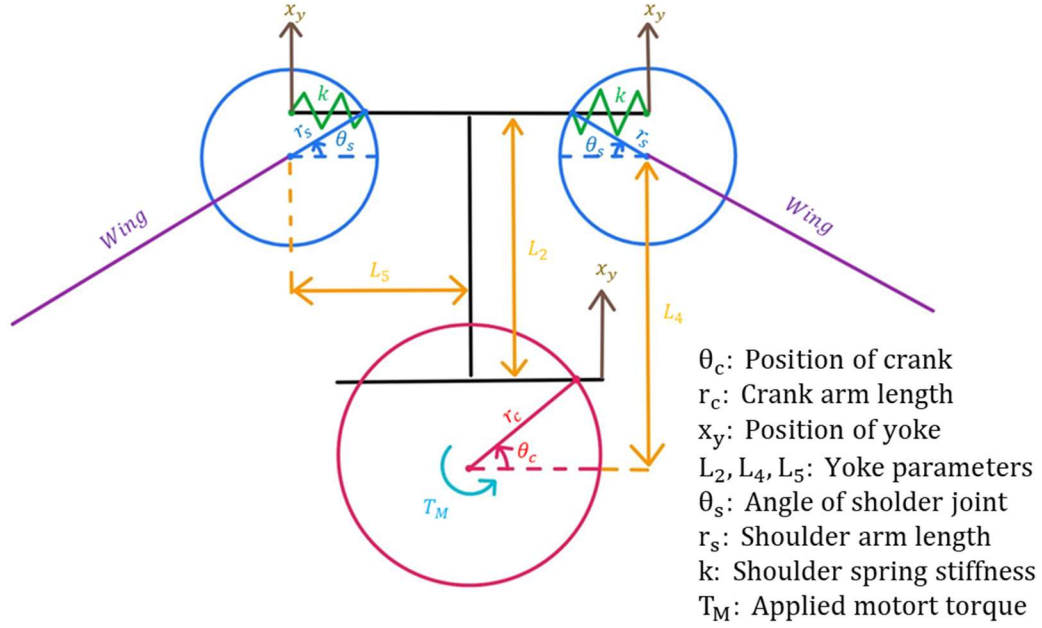


**Figure 3.12:** Diagram depicting the generalized coordinates and the parameters for the Scotch yoke flapping mechanism developed by [10].

The equations of motion for the three generalized coordinates  $\theta_c$ ,  $x_y$ , and  $\theta_s$  are derived using Lagrangian mechanics. Two holonomic constraint equations are defined to model the contact between the shoulder pin and the yoke, and the crank pin and the yoke. First, the kinetic and potential energies of the system are expressed as

$$T = \frac{1}{2}I_c\dot{\theta}_c^2 + \frac{1}{2}m_y\dot{x}_y^2 + I_{w+s}\dot{\theta}_s \quad (3.11)$$

$$V = kr_s^2(1 - \cos(\theta_s))^2 \quad (3.12)$$

Then, the Lagrangian of the system can be expressed as the difference in kinetic and potential energy.

$$L = T - V$$

$$L = \frac{1}{2}I_c\dot{\theta}_c^2 + \frac{1}{2}m_y\dot{x}_y^2 + I_{w+s}\dot{\theta}_s - kr_s^2(1 - \cos(\theta_s))^2 \quad (3.13)$$

Lastly, the holonomic constraints that model the contact between the yoke, crank and shoulder are expressed as

$$x_y - r_c \sin(\theta_c) = 0 \quad (3.14)$$

$$x_y - r_s \sin(\theta_s) = 0 \quad (3.15)$$

In the kinetic energy equation in 3.11,  $I_c$  is the mass moment of inertia of the crank,  $m_y$  is the mass of the yoke, and  $I_{w+s}$  is the mass moment of inertia of the shoulder and the wing. Using equations 3.11 to 3.15 the equations of motion can be derived using Lagrange's equation with the addition of two Lagrangian multipliers ( $\lambda_1$  and  $\lambda_2$ ) for each corresponding constraint force.

$$\frac{d}{dt} \left( \frac{\partial L}{\partial \dot{\theta}_c} \right) - \frac{\partial L}{\partial \theta_c} = T_M - \lambda_1 r_c \cos(\theta_c) \quad (3.15)$$

$$\frac{d}{dt} \left( \frac{\partial L}{\partial \dot{x}_y} \right) - \frac{\partial L}{\partial x_y} = \lambda_1 + \lambda_2 \quad (3.16)$$

$$\frac{d}{dt} \left( \frac{\partial L}{\partial \dot{\theta}_s} \right) - \frac{\partial L}{\partial \theta_s} = \lambda_2 r_s \cos(\theta_s) \quad (3.17)$$

By taking the partial derivate of the Lagrangian with respect to each generalized coordinate, the equations of motion of the Scotch yoke mechanism becomes

$$I_c \ddot{\theta}_c + \lambda_1 r_c \cos(\theta_c) = T_M \quad (3.18)$$

$$m_y \ddot{x}_y - \lambda_1 - \lambda_2 = 0 \quad (3.19)$$

$$2I_{w+s} \ddot{\theta}_s + 2kr_s^2 \sin(\theta_s) (1 - \cos(\theta_s)) + \lambda_2 r_s \cos(\theta_s) = 0 \quad (3.20)$$

Additionally, by taking the second-order time derivative of the constraint Equations 3.14 and 3.15,

$$\ddot{x}_y - \ddot{\theta}_c r_c \cos(\theta_c) + \dot{\theta}_c^2 r_c \sin(\theta_c) = 0 \quad (3.21)$$

$$\ddot{x}_y - \ddot{\theta}_s r_s \cos(\theta_s) + \dot{\theta}_s^2 r_s \sin(\theta_s) = 0 \quad (3.22)$$

two more equations are derived for the generalized coordinates to make 5 equations with 5 unknowns variables ( $\ddot{\theta}_c, \ddot{\theta}_s, \ddot{x}_y, \lambda_1, \lambda_2$ ). With this, the second order generalized

coordinates  $(\ddot{\theta}_c, \ddot{\theta}_s, \ddot{x}_y)$  can be solved in terms of the system state variables, and the nonlinear equations of motion of the Scotch yoke mechanism can be represented in state space form.

$$\dot{\vec{x}} = \vec{f}(\vec{x}, \vec{u})$$

where, the state variable vector is

$$\vec{x} = \begin{bmatrix} \theta_c \\ \dot{\theta}_c \\ x_y \\ \dot{x}_y \\ \theta \\ \dot{\theta}_s \end{bmatrix}$$

The Scotch yoke system takes a motor torque  $T_M$  as the input into the crank and outputs a one degree of freedom flapping motion at the shoulder that mimics the sweep angle motion of the moth. Using MATLAB's ode45, which is a 5<sup>th</sup> order ordinary differential equation solver using the Runge-Kutta method with 4<sup>th</sup> order error estimates, the state vector  $\vec{x}$  of the flapping mechanism can be solved. The parameters of the Scotch yoke mechanism are configured to output a wingtip flapping motion that is similar to the oscillatory sweep angle motion of the moth in hovering flight.

**Table 3.2:** Scotch yoke flapping mechanism parameters

<b>Flapping Mechanism parameters</b>	
$m_y$	0.35 g
$I_c$	1.22 g/mm <sup>2</sup>
$I_{w+s}$	96.09 g/mm <sup>2</sup>
$r_c$	2.39 mm
$r_s$	2.85 mm
$L_2$	7.11 mm
$L_4$	7.11 mm
$L_5$	5.08 mm
$\Delta$	152°

The engineered wings attached to the Scotch yoke mechanism are placed at an offset angle of  $\Delta$  from each shoulder pin. Varying this offset angle changes the range of the engineered sweep angle response on the wing. Decreasing  $\Delta$  increases the sweep angle magnitude at pronation and decreases it at supination, whereas increasing it has the opposite affect on the sweep angle. At  $\Delta = 152^\circ$ , the engineered sweep angle range accurately mimics the biological sweep angle range. From [10], the equation used to relate the wingtip angle and the crank angle of the mechanism is

$$\theta_w = \sin^{-1} \left( \frac{r_c \sin(\theta_c) + L_2 + L_4}{r_s} \right) + \Delta - \frac{\pi}{2} \quad (3.23)$$

The 2D wingtip motion from the Scotch yoke flapping mechanism is then expanded into three-dimensional space using the same kinematic model represented in Equation

3.8. However, the mechanism lacks the extra degree of freedom that mimics the elevation angle on the hawk moth. Thus, Equation 3.8 simplifies to

$$\vec{r}_{l,n} = \frac{n}{100} R \begin{bmatrix} \cos(\phi) \\ \sin(\phi) \sin(\beta) \\ -\sin(\phi) \cos(\beta) \end{bmatrix} \quad (3.24)$$

For any 2D wing cross-sectional element at  $n\%$  down the wingspan, the trajectory can be expressed as

$$\vec{r}_{l,n} = \frac{n}{100} R \begin{bmatrix} \sin(\phi) \sin(\beta) \\ -\sin(\phi) \cos(\beta) \end{bmatrix} \quad (3.25)$$

In Equations 3.24 and 3.25, the sweep angle  $\phi$  is the wingtip angle  $\theta_w$  in Equation 3.23 from the Scotch yoke mechanism redefined in the 3D kinematic model of the moth wing motion. The stroke plane angle ( $\beta$ ) and rotational angle ( $\alpha$ ) for the Scotch yoke flapping is equal to that of the hawk moth in hovering flight.

$$\phi(t) = \theta_w(t) - \theta_{w,m} + \frac{\theta_{w,max} - \theta_{w,min}}{2} \quad (3.26)$$

$$\beta = 23.4^\circ$$

In hovering flight, the hawk moth flaps its wings at a frequency of about 25.4 Hz which equates to 159.59 rad/s. Thus, to mimic this frequency, the Scotch yoke mechanism is initialized at a constant crank frequency of 159.59 rad/s with no motor torque input. The results of the Scotch yoke sweep angle solution and the biological sweep angle can be seen in Fig. 3.13.

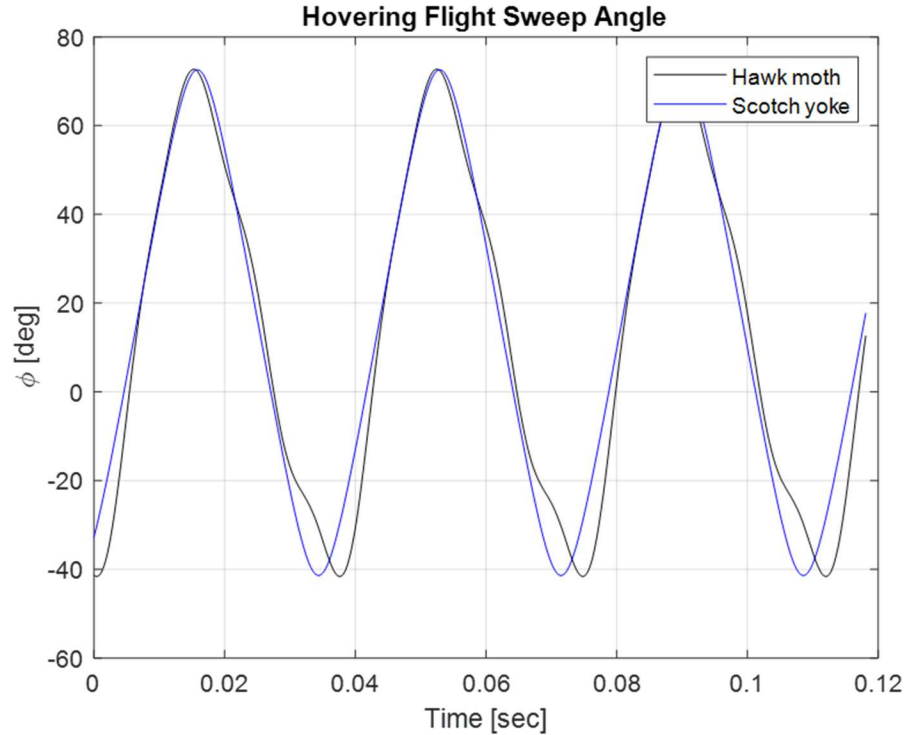


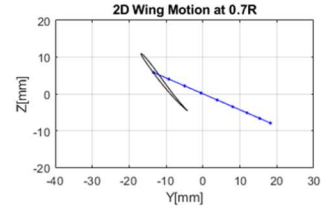
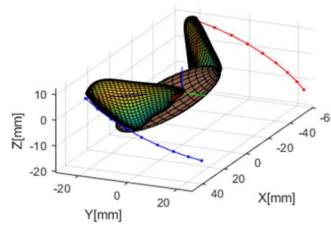
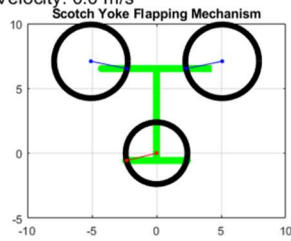
**Figure 3.13:** Sweep angle comparison for engineered flapping versus biological flapping. Scotch yoke mechanism is initialized to mimic hovering flight and the simulation ran for 3 flapping cycles.

Sweep angle results from the Scotch yoke flapping mechanism reaches similar sweep angle amplitudes as the hawk moth. The engineered flapping at pronation shows the wing transitioning from an upstroke motion to a downstroke at a similar time as the hawk moth. However, during supination, the difference in the time of transition is more noticeable. The engineered flapping mechanism transitions from downstroke to upstroke earlier compared to the hawk moth. This is mainly due to the difference in elevation angle between the two flapping motions. The Scotch yoke mechanism has no additional degree of freedom to mimic the elevation angle on the moth, hence its wingtip trajectory path is slightly shorter than that of the biological flapping trajectory. Because of this, it

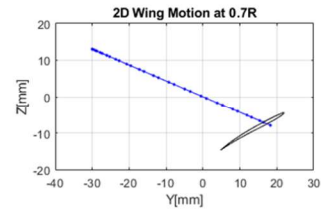
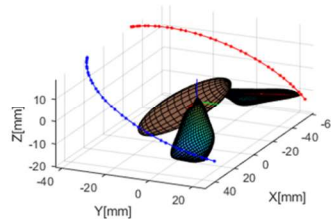
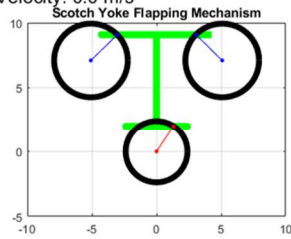


takes the biological wing slightly longer to reach the minimum sweep angle than the engineered wing.

Simulation Time: 0.0080 [sec]  
 Body Angle: 33.9 [deg]  
 Stroke Plane Angle: 23.4 [deg]  
 Elevation Angle: -0.0 [deg]  
 Sweep Angle: 27.1 [deg]  
 Rotation Angle: 130.1 [deg]  
 Forward Flight Velocity: 0.0 m/s



Simulation Time: 0.0310 [sec]  
 Body Angle: 33.9 [deg]  
 Stroke Plane Angle: 23.4 [deg]  
 Elevation Angle: 0.0 [deg]  
 Sweep Angle: -28.8 [deg]  
 Rotation Angle: 64.8 [deg]  
 Forward Flight Velocity: 0.0 m/s



Simulation Time: 0.0220 [sec]  
 Body Angle: 33.9 [deg]  
 Stroke Plane Angle: 23.4 [deg]  
 Elevation Angle: 0.0 [deg]  
 Sweep Angle: 40.1 [deg]  
 Rotation Angle: 59.3 [deg]  
 Forward Flight Velocity: 0.0 m/s

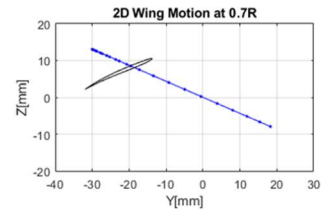
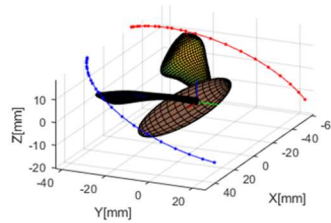
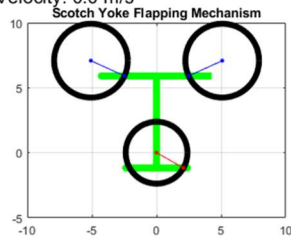


**Figure 3.14:** Scotch yoke flapping mechanism wing tip trajectory as depicted in 3D space.

After the Scotch yoke flapping motion is redefined in the 3D kinematic model, its flapping trajectory can be visualized in Fig 3.14 along with the components of the Scotch yoke mechanism that drives the flapping motion. With these results, the velocity of the 2D cross-sectional component of the wing is calculated similar to the derivation of Equation 3.10. Since the Scotch yoke mechanism does not mimic the elevation angle, Equation 3.10 is simply

$$\vec{v}_n = \frac{n}{100} R \begin{bmatrix} \dot{\phi} \cos(\phi) \sin(\beta) \\ -\dot{\phi} \cos(\phi) \cos(\beta) \end{bmatrix} \quad (3.27)$$

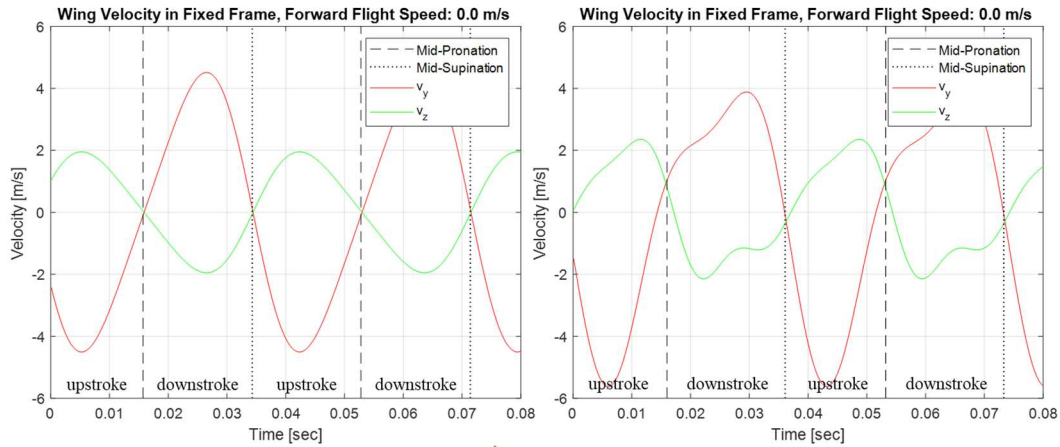


**Figure 3.15:** Wing velocity trend for Scotch yoke mechanism hovering flight (left) and the biological hovering flight.

Compared to the wing velocity in the biological hovering flight case, the Scotch yoke mechanism wing velocity differs in amplitude in the y-direction, but the trend of each velocity component remains fairly consistent with the biological case. A greater velocity amplitude in the y-direction is observed during upstroke and downstroke for each case and the z-component velocity remain within the range of -2 m/s to 2 m/s. Mid-pronation and mid-supination occurs at exactly 0 m/s for the Scotch yoke flapping

mechanism, but mid-pronation occurs at a slightly greater velocity on the hawk moth. Additionally, the main difference in the two trends is the maximum y-component velocity during upstroke. Whereas the Scotch yoke mechanism is driven at a constant crank angle throughout the flapping cycle, the hawk moth can vary its wing velocity at different phases of its flapping cycle. Hence, the velocity amplitude at upstroke and downstroke are the same on the Scotch yoke mechanism. However, on the hawk moth, the velocity amplitude during upstroke is greater than during downstroke. In Chapter 4, the aerodynamic mechanisms for both flapping cases will be investigated, and results will reveal whether the greater upstroke velocity and other differences in the biological flapping case is advantageous to the flight performance.

### **3.3.3 Effective Airflow Velocity and Angle of Attack Calculations**

Calculations for the effective airflow velocity and angle of attack on the wing are done to gain an initial insight on the flow conditions in the CFD simulation. For a wing cross section that is fixed in one position and free to rotate relative to the direction of the airflow, effective velocity describes the airflow velocity that the wing encounters as a result of its translational velocity. Effective angle of attack is a function of the fixed frame rotational angle and the direction of the wing velocity. Fig. 3.16 depicts the effective velocity and angle of attack as it relates to the 2D wing velocity at  $n\%$  of the wingspan ( $\vec{v}_n$ ) and rotational angle ( $\alpha$ ).

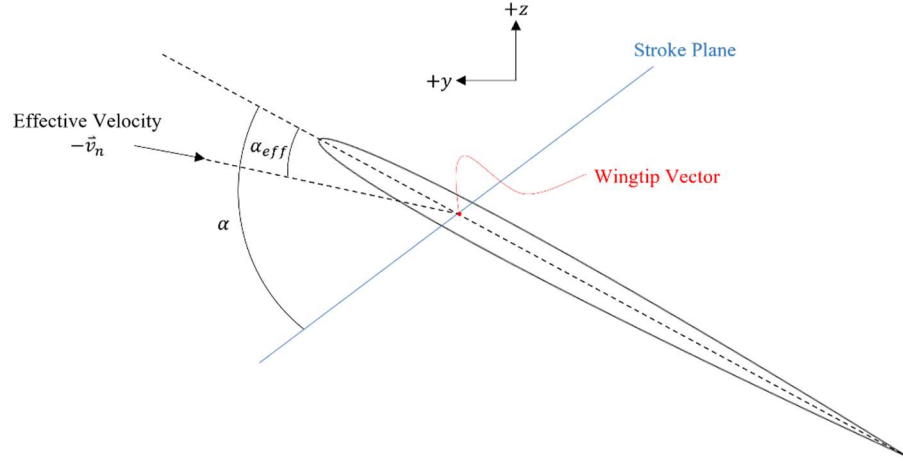


**Figure 3.16:** Diagram of wing cross-sectional geometry and the relation between the wing kinematics and the relative airflow. The wing section is allowed to rotate about the wingtip vector.

The effective airflow velocity is simply the velocity vector of the wing in the opposite direction. For hovering flight in both the biological and mechanical flapping cases, the effective velocity is the negative of just the wing velocity. For forward flight, this velocity is the negative of the sum of the forward flight velocity and wing velocity vector. The effective angle of attack is determined using the components of the wing velocity vector ( $\vec{v}_n$ ) and the rotational angle ( $\alpha$ ) of the wing about the stroke plane,

$$\alpha_{eff} = \alpha - \tan^{-1} \left( \frac{v_{n,z}}{v_{n,y}} \right) \quad (3.28)$$

In equation 3.28,  $\alpha_{eff}$  is the effective angle of attack,  $\alpha$  is the rotational angle of the wing relative to the stroke plane in the fixed reference frame, and  $v_{n,y}$  and  $v_{n,z}$  are the y and z components of the wing velocity. With the relative airflow condition and cross-sectional geometry angle of attack properly defined, these two quantities can be computed for each of the wing flapping cases discussed in Sections 3.2.1 and 3.2.2.

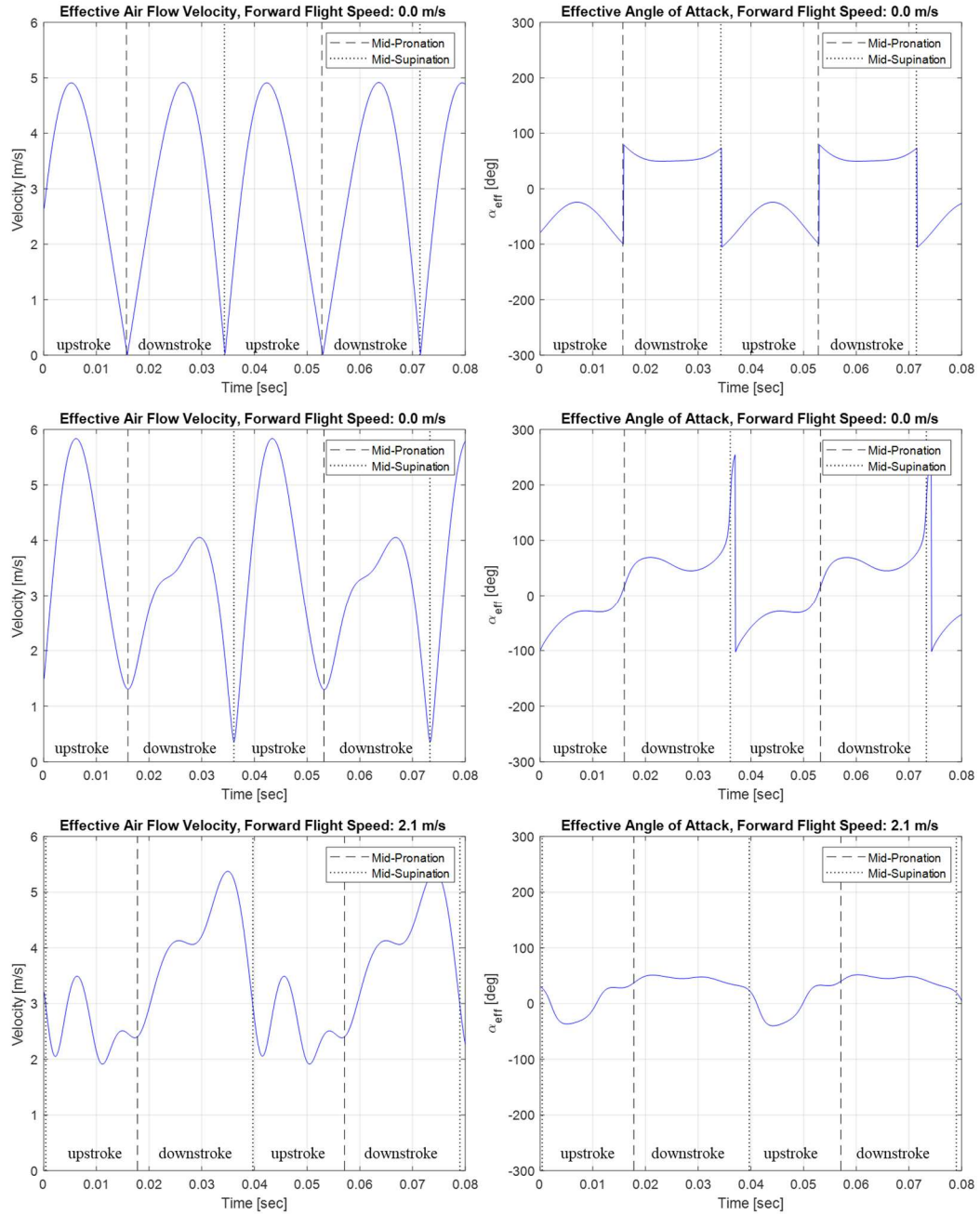


**Figure 3.17:** Effective airflow velocities and angles of attack for the Scotch yoke mechanism hovering flight (first row), hawk moth hovering flight (second row), and hawkmoth forward flight at a speed of 2.1 m/s (third row).

The kinematics describing the motion of the wing can be used to determine the relative flow regime within a CFD simulation. For hovering flight at a frequency of 25.4 Hz on the hawk moth, one flapping cycle is completed by the moth in approximately

0.035 seconds. A maximum effective velocity of 5.84 m/s is reached in mid-upstroke and the minimum occurs during mid-supination at 0.58 m/s. For a forward flight speed of 2.1 m/s on the hawk moth, the maximum effective velocity of 5.37 m/s occurs at mid-downstroke and the minimum occurs during mid-upstroke at 1.91 m/s. Finally, on the Scotch yoke flapping mechanism operating at the same constant frequency of 25.4 Hz for hovering flight, one cycle is completed at the same time. The maximum effective velocity occurs at both mid-upstroke and mid-downstroke at 4.91 m/s. The minimum effective velocity occurs at mid-pronation and mid-supination at 0 m/s.

Although these results do not provide new information on the aerodynamic efficiency of the wing geometry at the sampled design configuration, it is important for determining the flow regime in the CFD software. Additionally, a comparison of the hawk moth hovering and forward flight data sets show a greater downstroke velocity and smaller upstroke velocity for a forward flight, and a greater upstroke velocity and smaller downstroke velocity for hovering flight. The range of effective angle of attack at hovering flight is also much larger than that of the forward flight wing trajectory. These results, along with research done in [6] and [10] provide insights into the aerodynamic mechanisms that enhance lift and thrust for the wing and their relation to the kinematics of the wing motion.

# **Chapter 4 Computational Aerodynamic Simulations**

## 4.1 Chapter Overview

Results in [7] on the aerodynamic lifting mechanisms of the *Manduca Sexta* forewing identified three lift enhancing mechanisms for flapping flight. During downstroke, delayed stall generates leading edge vortices on the upper surface of the wing to create a pressure differential between the lower and upper surface. Following mid-downstroke, the wing aggressively transitions its rotation angle to generate rotational lift before entering upstroke. Finally, during upstroke, wake capture occurs where the wing switches directions to collide with the previously shed wake. At certain angles of rotation, the moth can take advantage of wake capture to enhance lift and even propel itself forward. The study done in [7] concluded that the moth utilized unsteady flow for all flight speeds with flow visualization results even showing larger leading-edge vortices during higher flight speeds compared to hovering flight. The CFD study done in this chapter will investigate the aerodynamic mechanisms involved in a flapping wing and validate the results with the work done in [7].

The computational fluid dynamic simulations performed in this thesis utilizes the Ansys Fluent solver version 20.1 for computing the aerodynamic forces (lift and drag) of 2D wing cross sections. Each design case follows the same workflow that utilizes MATLAB to automate the geometry generation and flapping kinematic modeling for defining the fluid domain and mesh motion in Ansys. First, the geometry parameter of the forewing is defined according to the wing modeling method developed in section 3.1. Then, an Ansys compatible geometry file is written for a 2D wing cross-sectional geometry at 0.7R along the wingspan. Lastly, a user-defined function (UDF), consisting of the kinematic equations derived in section 3.2, is written as a c-file for one of the three



desired flapping cases. Fig. 4.1 depicts the workflow used to run the CFD simulations and gather results.

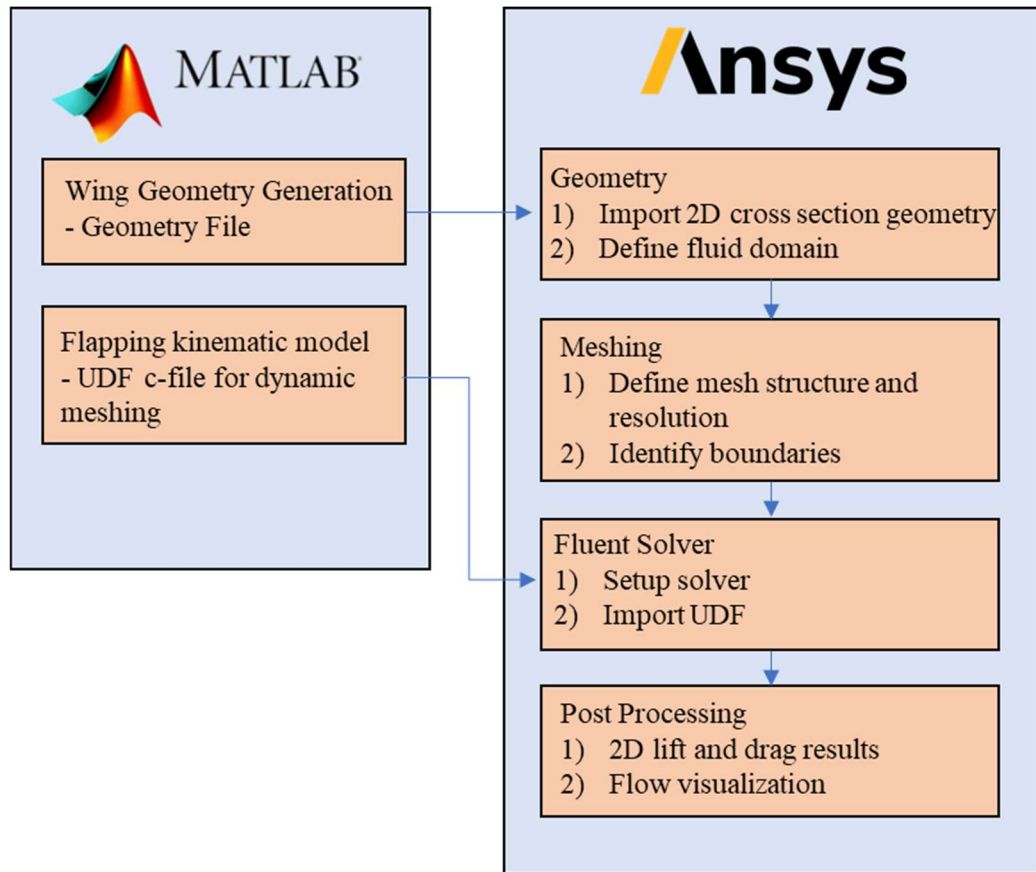


**Figure 4.1:** Depiction of Ansys simulation workflow, and the input geometry and UDF files from MATLAB.

This chapter is organized as follows. First the aerodynamics of all three flapping motion cases from Section 3.2 are investigated in a 2D CFD simulation using a symmetrical airfoil geometry at the cross-section of the wing. Then, the time-averaged vertical and horizontal force results in hovering flight are compared against results from [11] on the 3D aerodynamics of the hawk moth in hovering flight. Lastly, the chapter ends with simulation results for all the wing geometry configurations sampled from the LHC design space in Chapter 3.

## 4.2 CFD Simulation Setup

The governing equations solved in the CFD simulation are the 2D incompressible, unsteady, Navier-Stokes equations. They are written in the y-z components as the continuity equation (4.1) and fluid momentum equations (4.2) and (4.3).

$$\frac{\partial v}{\partial y} + \frac{\partial w}{\partial z} = 0 \quad (4.1)$$

$$\rho \left( \frac{\partial v}{\partial t} + v \frac{\partial v}{\partial y} + w \frac{\partial v}{\partial z} \right) = -\frac{\partial p}{\partial y} + \mu \left( \frac{\partial^2 v}{\partial y^2} + \frac{\partial^2 v}{\partial z^2} \right) \quad (4.2)$$

$$\rho \left( \frac{\partial w}{\partial t} + v \frac{\partial w}{\partial y} + w \frac{\partial w}{\partial z} \right) = -\frac{\partial p}{\partial z} + \rho g_z + \mu \left( \frac{\partial^2 w}{\partial y^2} + \frac{\partial^2 w}{\partial z^2} \right) \quad (4.3)$$

In the above equations,  $v$  and  $w$  are the flow velocities in the  $y$  and  $z$  direction, respectively.  $\rho$  is the constant airflow density at  $1.225 \text{ kg/m}^3$ ,  $\mu$  is the dynamic viscosity of the fluid ( $1.789 \times 10^{-5} \text{ Pa} \cdot \text{s}$ ),  $p$  is the flow pressure,  $g_z$  is the gravitational acceleration, and finally  $t$  is time. Using the Ansys Fluent pressure-based solver and a dynamic meshing method on triangular mesh structures, transient time CFD simulations are utilized to determine the aerodynamic mechanisms responsible for the lift and drag forces on a 2D flapping wing.

The Fluent solver used in this research is a pressure-based coupled algorithm that simultaneously solves for the system of momentum and pressure-based continuity equations at each cell. After Equations 4.1 to 4.3 are solved, the mass flux of the airflow is updated at each cell, and the convergence criteria are checked at each iteration. If the simulation is not converged, the fluid properties are updated and Equations 4.1, 4.2, and 4.3 are solved again with the updated fluid properties. If the simulation converges, the

dynamic mesh structure steps further in time according to the UDF, and simulation results for the next time step are calculated with the updated mesh structure.

The convergence criteria are defined using the flow momentum and continuity residual values. The residual values during each iteration determine the imbalance of conserved quantities in the simulation. The continuity equation (4.1) represents mass conservation, and the momentum equations (4.2) and (4.3) represents momentum conservation. Small residual values show that these quantities are well conserved in the fluid domain and is an indication of convergence. For the simulations performed in this work, a residual value of  $1E - 5$  is set as the convergence criteria for each conserved quantity at every timestep in the transient simulation.

### **4.3 CFD Simulations on Three Flapping Cases**

Initial CFD simulations are performed to investigate the aerodynamics around the wing for the three flapping cases discussed in Section 3.2. For each case, the same forewing geometry is used and a 2D fluid domain with a triangular mesh structure is generated around the wing cross section at 70% of the wingspan. The position of the wing and rotational angle is initialized at the mid-supination position as defined in the kinematic model in Section 3.2.1.

### 4.3.1 Wing Geometry and Fluid Domain Meshing

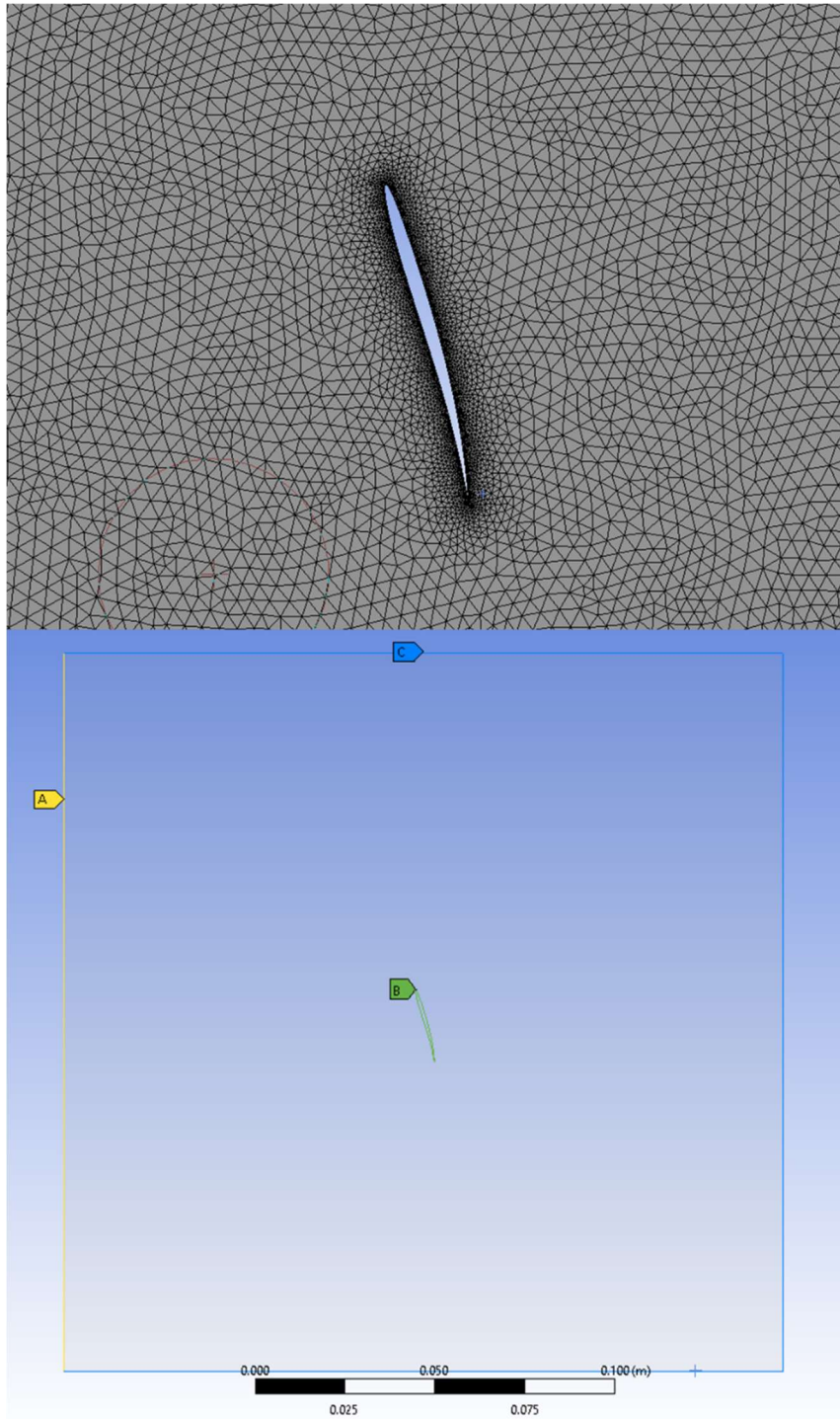


**Figure 4.2:** Initial mesh structure around wing cross section (top) and boundary condition of the fluid domain (bottom). Boundary A (yellow) is set as an incompressible inlet. B (green) is the airfoil wall with no slip boundary condition. C (blue) is set as the flow outlet.

The wing geometry depicted in Fig. 4.2 is an airfoil shape symmetric about the biological mean camber line. Its geometric parameters according to the wing modeling method discussed in section 3.1 are

$$R = 49.57 [mm], C = 18.71 [mm], M = 0\%, P = 30\%, Th = 3 [mm]$$

This geometry is imported into Ansys for all three flapping cases and a triangular mesh structure is generated around the geometry to represent the fluid domain. This wing design will be referred to as the control sample in later discussions on surrogate modeling. For the control sample, the resolution of the mesh structure is determined through a grid sensitivity analysis that will be discussed later in this section. After successfully generating the mesh, boundaries in the fluid domain are identified and the flow conditions at the boundaries are determined in Fluent.

### **4.3.2 Fluent Setup**

The mesh structure generated in the previous section is imported into the Fluent solver and the solver is setup for transient, dynamic meshing simulations. To simplify the calculations, only unsteady, laminar flow is modeled in the simulation. For hovering flight, the effective airfoil velocity on the wing varies between 1.29 m/s and 5.84 m/s and the chord length varies between 16 [mm] and 32 [mm]. As a result, the Reynolds number of the flow is between 1400 and 12000. Hence, more accurate models of the flow around the wing would include laminar-turbulent transition models for Reynolds numbers greater than 2000. The airfoil wall is set as a no slip boundary condition. Inlet velocity magnitude is the forward flight velocity of the moth. For the two hovering flight cases, the inlet velocity is zero, and for forward flight, inlet velocity is 2.1 m/s. The pressure at the outlet is set as the standard atmospheric pressure at sea level (101325 Pa), or a gauge

pressure of 0 Pa. The simulation runs for 4 flapping cycles for each case (about 0.15 seconds) at a time step size of  $\Delta t = 0.0001$ .

### 4.3.3 Post CFD Calculations

The aerodynamic forces of interest are the vertical, z-direction force and horizontal, y-direction force on the wing section in the fixed reference frame. The fixed reference frame is the same as the one defined in Fig. 3.16, where the positive z axis points toward the upper surface of the wing section and the positive y axis points toward the leading edge. Hence, the direction of the lift force on the wing is in the positive z and drag is in the negative y direction. Both the vertical and horizontal forces can be expressed in terms as components of the pressure force and viscous force vectors.

$$f_V(t) = (\vec{f}_p(t) + \vec{f}_v(t))\hat{z} \quad (4.4)$$

$$f_H(t) = (\vec{f}_p(t) + \vec{f}_v(t))\hat{y} \quad (4.5)$$

In Equations 4.4 and 4.5,  $\vec{f}_p(t)$  and  $\vec{f}_v(t)$  are the time-varying pressure force and viscous force vectors acting on the wing cross section. The units of the 2D vertical and horizontal forces are in Newton force per unit meter of span ( $N/m$ ). The aerodynamic forces can be approximated for a 3D wing under the assumption of constant chord length. Results for  $f_V(t)$  and  $f_H(t)$  are multiplied by 2 times the length of the wingspan  $R$  to account for both wings on the moth. Thus, the approximated total aerodynamic forces are  $F_V(t) = 2f_V(t)R$  and  $F_H(t) = 2f_H(t)R$ . Furthermore, the forces are non-dimensionalized into time average vertical and horizontal force coefficients by

$$\bar{C}_V = \frac{\bar{F}_V}{0.5\rho\bar{v}_{eff}^2S} \quad (4.6)$$

$$\bar{C}_H = \frac{\bar{F}_H}{0.5\rho\bar{v}_{eff}^2S} \quad (4.7)$$

In the above equations, the average vertical ( $\bar{C}_V$ ) and horizontal ( $\bar{C}_H$ ) force coefficients are calculated by dividing the time averaged total forces by the time averaged dynamic pressure and wing surface area ( $S$ ). The dynamic pressure is a function of the effective flow velocity ( $v_{eff}$ ) that was calculated in Section 3.2.3. The average aerodynamic forces and coefficients are calculated for each flapping case and the results are compared with the 3D fluid structure interaction simulations on the hawk moth in hovering flight done in [11].

#### 4.3.4 Grid Sensitivity Analysis

Before CFD simulations are performed for each flapping case, a grid sensitivity analysis on the biological hovering flight case is performed to reduce computational cost and to determine the level of sensitivity to the mesh. Three types of mesh with different number of cells were compared and the results are presented in Fig. 4.3. The three meshes consists of around  $5.3 \times 10^3$  cells (coarse mesh),  $8.8 \times 10^4$  cells (medium mesh), and  $2.1 \times 10^5$  cells (fine mesh).

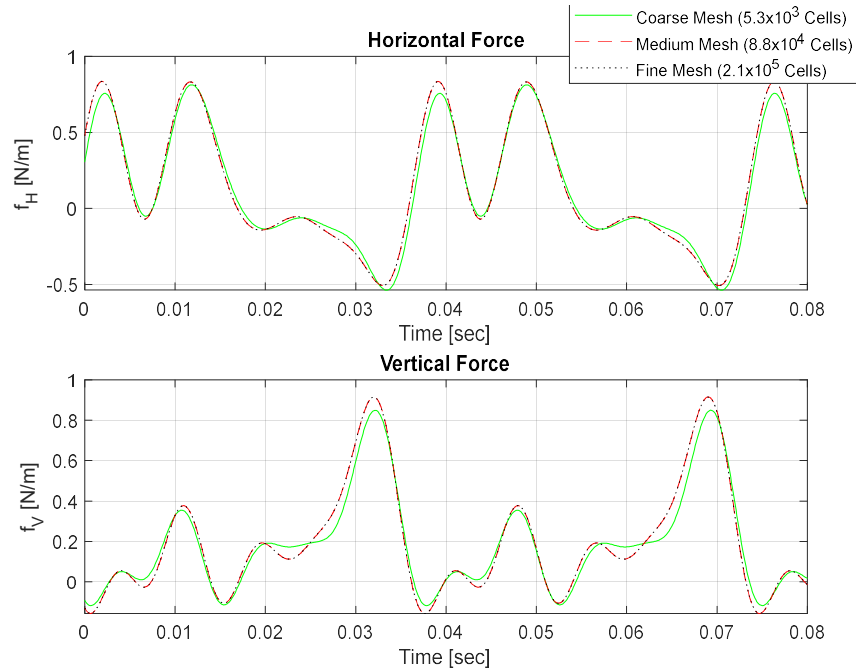


**Figure 4.3:** Grid sensitivity results done on biological hovering flight case. The results are the lift and drag forces per unit meter wingspan of one wing section.

The results from the grid sensitivity study shows the vertical and horizontal forces for the medium mesh and fine mesh agree with each other, but the coarse mesh results are slightly different from the other two. With less cells, the medium mesh simulations computed similar results to the fine mesh in a shorter amount of time. As such the medium mesh is used for all future simulations.

### 4.3.5 CFD Results for Three Flapping Cases

The aerodynamic forces for each of the flapping case discussed in Section 3.2 are investigated in CFD simulations using the same mesh resolution as the medium mesh in Section 4.2.4. For all three flapping cases, the simulations ran for 4 flapping cycles, and the wing section and fluid around it start at rest. The steady trend in the aerodynamic forces was not observed until the beginning of the 3<sup>rd</sup> flapping cycle. This is because the



first two flapping cycles served as initial wake formation cycles in the simulation for wake interaction during the 3<sup>rd</sup> and 4<sup>th</sup> cycles.

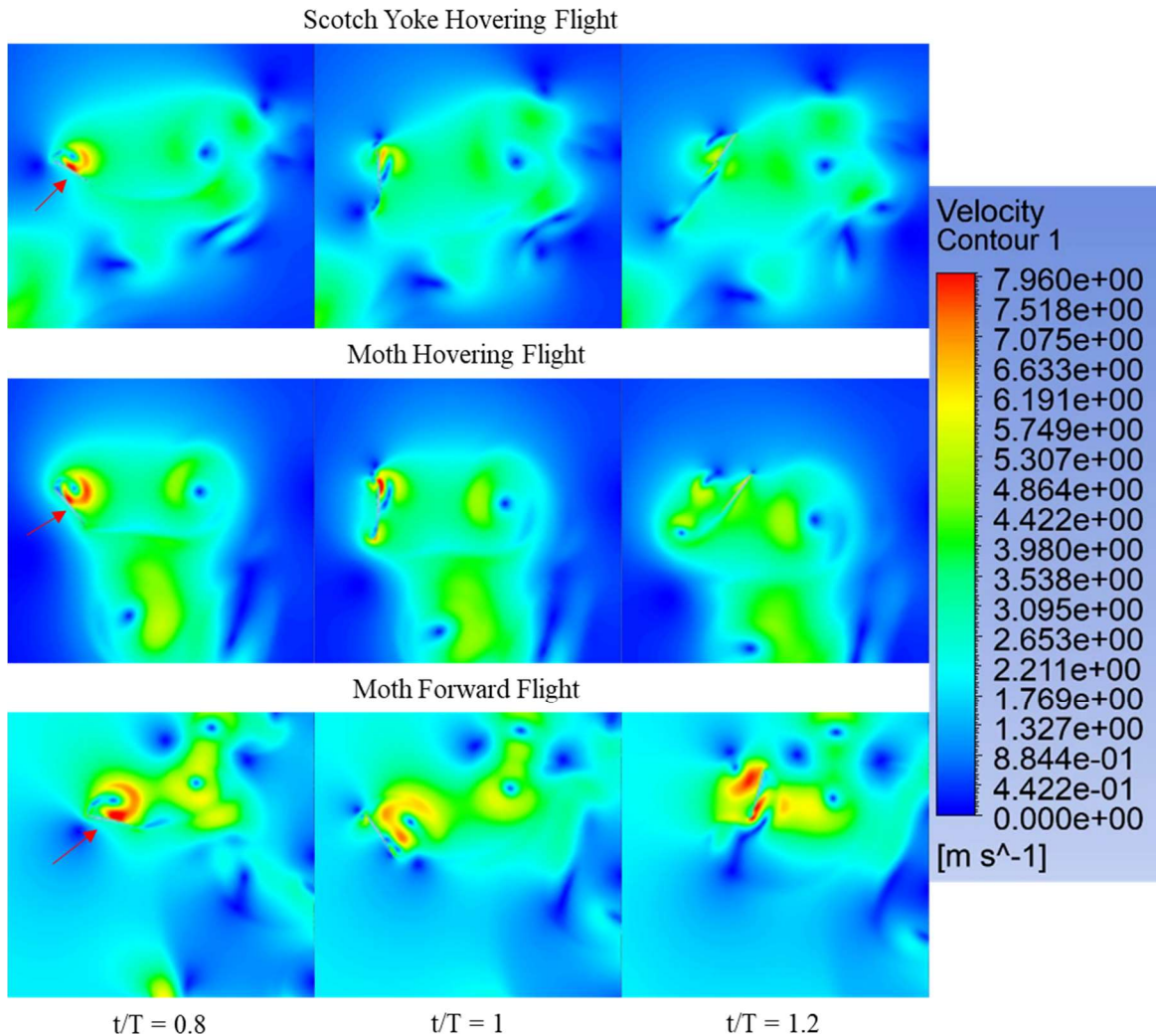


**Figure 4.4:** Sequence of frames from CFD simulations showing fluid velocity contours for all three flapping cases. The wing cross section can be seen as a small grey slit within the velocity contour. Red arrow in the first frame of each case points to the wing cross section.

The sequence of frames depicted in Fig. 4.4 show the wing in downstroke, supination, and then upstroke for all three flapping cases. The resulting aerodynamics show a leading-edge vortex forming on the upper surface of the wing during downstroke

( $t/T = 0.8$ ). The wing then rotates during supination to generate rotational lift ( $t/T = 1$ ). Finally, during upstroke, the wing collides with the wake created during downstroke ( $t/T = 1.2$ ) and additional lift is generated during the upstroke phase. The leading-edge vortex creates a region of high velocity and low pressure on the upper surface of the wing while lower surface pressure remains relatively high, hence this pressure gradient creates the main lifting force on the moth for all three types of flapping.

The velocity contour for the three flapping cases shows differences in the flow characteristic around the wing. The lift enhancing mechanisms observed in both [7] and [11] are also observed here. In the forward flight case, larger regions of unsteady flow can be observed around the wing as compared to the two hovering flight cases. The largest leading-edge vortex is formed in the forward flight case during downstroke, and the smallest is observed for the Scotch yoke hovering case. This difference in the leading-edge vortex determine the magnitude of the main lifting mechanism produced by each flapping motion. Comparing the two hovering flight cases, a larger leading-edge vortex creates a greater pressure difference between the lower and upper surface, hence greater lift is generated during downstroke in the hawk moth hovering case.

Fig. 4.4 also show instances when the wing utilizes rotational lift in each flapping case. Rotation lift is made possible on the wing by the rapid change in the rotational angle at supination and pronation. This lift force on the wing is created from the Magnus effect. During supination and pronation, the wing rotates aggressively to create a region of high velocity at the leading edge and low velocity at the trailing edge. During supination, the direction of air flow around the wing is in the -y direction as the wing is finishing its downstroke in the +y direction, hence the wing rotates in a clockwise

direction such that the leading edge moves in the direction of the airflow, increasing the flow velocity at that point, and the trailing edge moves in the opposite direction of flow, decreasing the flow velocity at that point. During pronation, the wing rotates in a counterclockwise direction to generate the same Magnus lift. The lift generated from the Magnus effect can be seen at  $(t/T = 1)$  for both hovering flight cases.

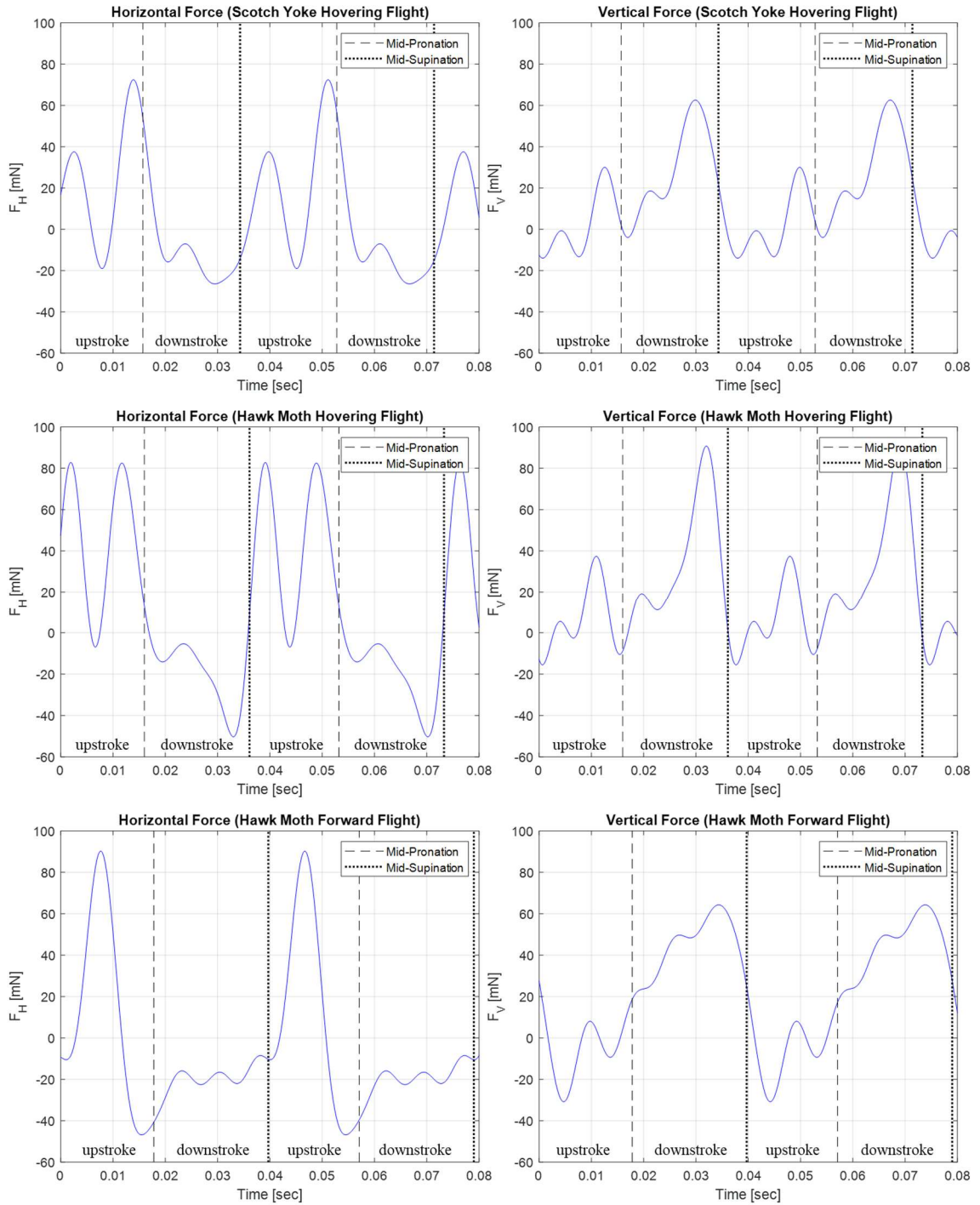


**Figure 4.5:** Vertical and horizontal force plots for all three flapping cases. Lines on the plot indicate when the wing is in mid-pronation or mid-supination. The course of the wing stroke between the lines are divided into downstroke and upstroke.

Fig. 4.5 show plots of the vertical and horizontal forces for all three flapping cases with trends in the data revealing instances when lifting mechanisms take effect. For the Scotch yoke and hawk moth hovering cases, the vertical and horizontal forces have the same trend, however the magnitude in the forces differed. The repeating trend for both cases were observed after the 2<sup>nd</sup> flapping cycle, and the unsteady aerodynamic mechanisms for generating lift are observed. After mid-supination, the effective angle of attack increases, and the max vertical force produced from rotational lift can be observed at the first peak after the mid-supination line for both cases. As effective velocity continues to increase during upstroke, the angle of attack begins to level off on the hawk moth whereas on the Scotch yoke mechanism it reaches a peak and decreases. As mentioned before, this difference is caused by the lack of elevation angle in the Scotch yoke mechanism. The result of this is a smaller lift force on the Scotch yoke flapping mechanism during wake capture. The maximum lift force during wake capture for the hawk moth hovering flight is 8 mN greater than the Scotch yoke hovering flight.

During the end of the upstroke phase, a leading-edge vortex is formed underneath the wing as it enters stroke reversal. At this point, the vertical lift force decreases as the effective velocity decrease and the pressure above the wing start to become greater than the pressure below. The first peak in the vertical force plot after mid-pronation is created from rotational lift as the effective angle of attack increases again. Results in Fig. 4.5 show that the rotational lift created during mid-pronation for both hovering cases are approximately equal. Finally, the greatest vertical force is created during downstroke. CFD results show a larger leading-edge vortex being formed during downstroke in the hawk moth hovering case than in the Scotch yoke hovering case. This results in a larger

pressure differential between the upper and lower surface of the wing on the hawk moth compared to the Scotch yoke, hence creating a greater downstroke lift force on the hawk moth. At downstroke, the maximum lift created by the hawk moth is 28 mN greater than the Scotch yoke.

The time-averaged vertical and horizontal forces are calculated for the hovering flight cases and the results are compared to the work done in [11]. The research done in [11] also investigated the hovering flight on a hawk moth in a 3D transient, fluid structure interaction simulation. In that study, the kinematic variables  $\phi$  and  $\alpha$  are sinusoidal functions of time and elevation angle  $\theta$  is 0. The range of  $\phi$  and  $\alpha$  are approximately equal to those in this paper, and the main difference between the hovering flight kinematic model in [11] and the hawk moth hovering case in this thesis is the elevation angle  $\theta$ . When compared to the rigid wing case in [11], the average vertical force in the hawk moth flapping case agreed more with the results in [11] than the average horizontal forces.

**Table 4.1:** Time-averaged aerodynamic force comparison for hovering flight

Cases	Vertical Force (mN)			Horizontal Force (mN)		
	$\bar{F}_{V,down}$	$\bar{F}_{V,up}$	$\bar{F}_V$	$\bar{F}_{H,down}$	$\bar{F}_{H,up}$	$\bar{F}_H$
Hawk Moth (Presented)	33.9	5.67	21.0	-18.5	45.1	10.6
Scotch Yoke (Presented)	27.9	2.39	15.2	-9.77	21.5	5.65
Hawk Moth [11]	26.3	12.9	19.2	-14.8	26.0	5.70

The results in Table 4.1 are the time-averaged vertical and horizontal forces calculated from CFD results in the hawk moth and scotch yoke hovering cases. They are compared to the aerodynamic forces calculated in [11] for a rigid-wing hawk moth in hovering flight. The average horizontal force created by the hovering hawk moth in this

paper differs from both the Scotch yoke hovering and hovering case in [11]. The reported force in [11] was  $5.7 [mN]$ , whereas  $\bar{F}_H$  was calculated to be  $10.6 mN$  and  $5.65 mN$  in the hawk moth and Scotch yoke hovering case, respectively. A comparison of the horizontal force suggests the difference in magnitude of  $\bar{F}_H$  may be a result of the amplitude in elevation angle as both [11] and the Scotch yoke cases do not have an elevation angle in their kinematic models. However, a comparison of the horizontal force trends shows a difference between the Scotch yoke case and the horizontal force plot in [11]. As for the vertical force, the average vertical force created by the hawk moth in hovering flight more closely agree with [11] than the Scotch yoke results. Additionally, the vertical force trend in all three data sets agree with one another. From this comparison, the result in this thesis suggests that the 2D CFD model used is effective in estimating the lift forces on the moth in hovering flight but drag and thrust forces require further consideration of 3D aerodynamic mechanisms.

## 4.4 Training Data Experiments

The experiments conducted for collecting training data combines the Latin Hypercube wing geometries sampled in Section 3.2.3 and the hawk moth hovering kinematic equations developed in Section 3.3.1 into the CFD simulation discussed in previous sections of this chapter. The performance of each sampled wing geometry is compared with the control sample modeled in Section 4.3.1. Each sample follows the same workflow discussed in previous sections. First, a 3D wing geometry is modeled based on the Latin Hypercube samples drawn from the design space, and the 2D cross section geometry at 70% of the wingspan is imported into Ansys as a geometry file. Then, a triangular mesh structure is built around the imported geometry. Afterwards, a user-defined function that contain the flapping kinematic equations for the hawk moth in hovering flight is imported into Fluent and used as mesh motion equations for dynamic meshing. Lastly, Fluent is set up to run transient CFD simulations with dynamic meshing for 4 flapping cycles.

CFD simulations were conducted for the 20 wing designs sampled in Fig. 3.6. Each 2D wing geometry is investigated in hovering flight and the results are presented in Fig. 4.6. Out of the 20 simulations conducted, three wing geometry cases failed to meet the convergence criteria. The failed cases (samples 1,2, and 5) all have similar geometry properties such as a thin cross section and a large maximum camber near the trailing edge of the wing. Running samples 1, 2, and 5 simulations with the mesh structure in Fig. 4.2 was ineffective in converging the simulation residual to a value of less than  $1E - 5$ , hence future attempts to investigate them require a different mesh structure.



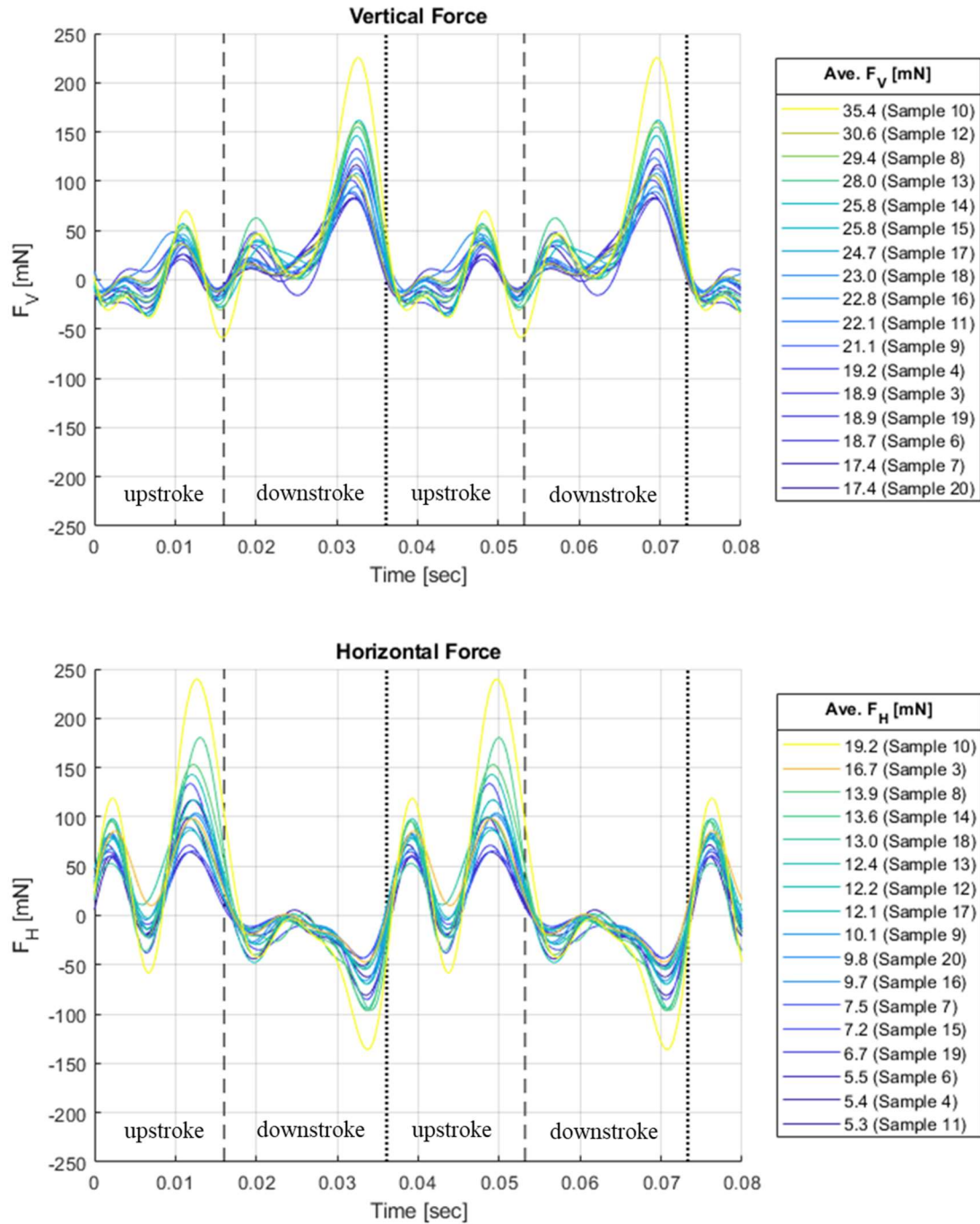


**Figure 4.6:** Vertical and horizontal force results for each of the sampled wing geometries. The average forces for each wing geometry sample are presented in the legend.

Results in Fig. 4.6 show a similar trend in the aerodynamic forces among all the wing geometry cases. The trend follows that of the hawk moth in hovering flight with

peaks on the vertical force plot showing the effects of the unsteady aerodynamic lift mechanisms. Variations in the magnitude of the forces are observed for each wing design, with the greatest variation occurring at the maximum lifting force during downstroke. Because this lifting force is caused by the formation of a leading-edge vortex on the upper surface of the wing, the variation in the lift produced from it suggests that change in wing geometry influences the size of the leading-edge vortex. A large variation in the aerodynamic force is observed once again in horizontal force plot. During the end of the upstroke phase, a maximum horizontal force in +y direction is caused by a leading-edge vortex forming underneath the wing as it is transitioning into pronation. The large variation in the force magnitude here once again suggests that leading-edge vortices of different sizes are being formed because of the difference in wing geometry.

During hovering flight, the ideal horizontal force created by the wing should be close enough to zero for the moth to stay in the same horizontal position. Hence the performance of each wing is assessed by comparing the lift-to-drag in hovering flight. Among all wing designs, sample 11 outperforms every other wing design and the control sample. The calculated lift-to-drag ratio on the control sample was 1.97, whereas sample 11 was calculated to be 4.17. The results of the CFD simulations and the calculations made afterwards for each sample are presented in Appendix B. For the supervised machine learning portion of the surrogate modeling approach, the lift-to-drag ratio results are used as the response variable data and the geometry parameters make up the predictor variable data.

# **Chapter 5 Surrogate Modeling Approach**

## 5.1 Chapter Overview

The surrogate modeling design approach is a data driven method of constructing estimation models that aims to predict results from real world experiments or computationally expensive simulation experiments. In aircraft wing design problems, surrogate models are utilized for rapid performance estimation and shape optimization after data from CFD simulations or wind tunnel testing have been gathered. For the problem presented at the beginning of this thesis, surrogate models offer quick estimations of the aerodynamic performance on the hawk moth in hovering flight for various wing design configurations. In this chapter, surrogate models are trained using supervised regression learning algorithms in MATLAB's regression learner toolbox, and the resulting models are assessed based on their prediction performances. Methods for assessing the surrogate models and interpreting their prediction performances are done according to [14]. The best performing model is evaluated within the design space of the wing, and the resulting predictions reveal lift-to-drag sensitivity from variations in wing geometry parameters. Finally, an optimization algorithm is implemented on the surrogate model to identify the maximum lift-to-drag ratio within the design space.

## 5.2 Supervised Regression Learning

The training data gathered in Section 4.4 is a set of labeled data with a known response variable and known input variables. Lift-to-drag ratios calculated from before are used as the performance metric for each of the sampled wing designs, thus it is assigned as the response variable in the training data set. The predictor variables are the wing geometry parameters that define the shape of the wing. Both the response and

predictor variables are a set of continuous data that were gathered in the geometry modeling section and CFD simulation section of this thesis. Because this type of data is gathered, the best approach is to train models using supervised regression learning algorithms and present the lift-to-drag ratio as a continuous function of the geometric parameters within the bounds of the design space.

The regression model training done in this thesis utilizes MATLAB's Regression Learner toolbox. Available in the toolbox are classes of regression models such as Support Vector Regression, Gaussian Process Regression, Linear Regression, etc. Fig. 5.1 depicts the training data used for surrogate modeling. The available classes of regression models on MATLAB are trained to estimate the lift-to-drag ratio given wing geometry parameters. The training method utilizes a  $k$ -fold cross validation resampling technique for validating model predictions with the actual data. The training data is partitioned into  $k$  subsets, and one subset is assigned as the validation data while the others are used as training data. The algorithm reassigns the validation set  $k$  times for different subsets in the whole data set. For the data set presented, it was determined that a 4-fold cross validation resampling method trained the best performing prediction models.

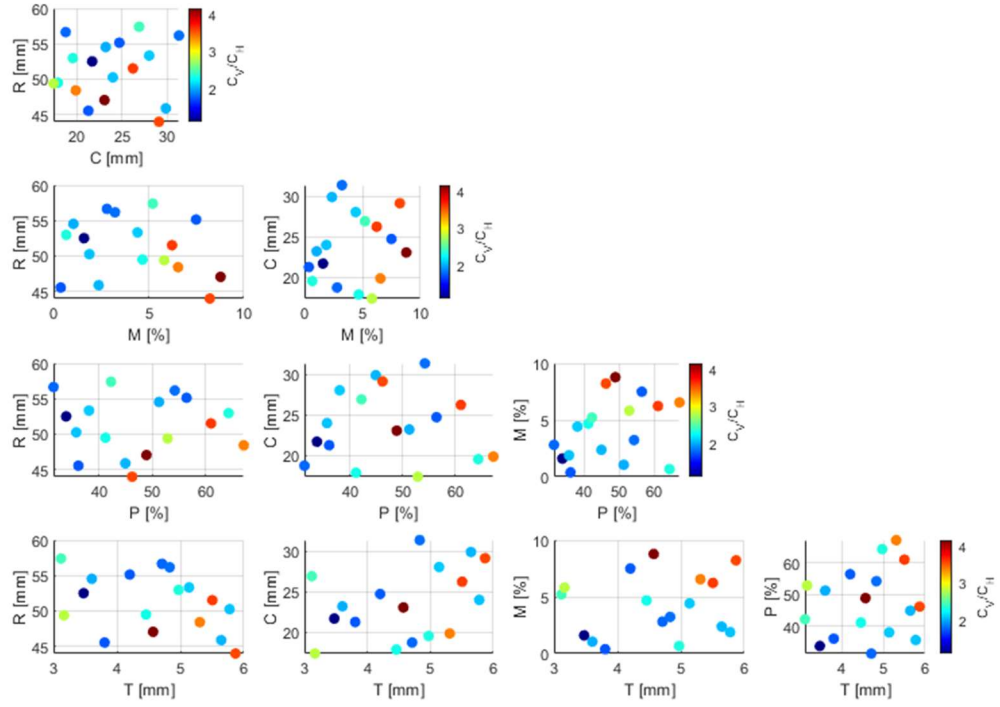


**Figure 5.1:** Training data set used for surrogate modeling. The response variable ( $C_V/C_H$ ) are color coded based on their magnitudes shown on the color bar. Predictor variables are the vertical and horizontal axes on each plot.

By ranking each surrogate model based on minimum root mean squared error (RMSE) of the predicted versus actual lift-to-drag ratio, three Support Vector Regression (SVR) models were identified as the best performing models for predicting lift-to-drag ratio. The training data set used on the SVR models is defined as follows

$$D = \{(\vec{x}_i, y_i) \in \mathbb{R}^6\}_{i=1}^{17} \quad (5.1)$$

Here,  $\vec{x}_i$  is a 5-dimensional vector consisting of the  $i^{th}$  predictor value that define the geometry of the wing.  $y_i$  is the  $i^{th}$  response variable value representing the lift-to-drag ratio calculated from before. The set of training data is a 17 by 6 matrix with rows consisting of 17 data points, and columns consisting of the 5 predictor variables and 1

response variable. The support vector machine is trained to determine an optimal 5<sup>th</sup> dimensional hyperplane fitted to predict the one-dimensional response variable. For a simple linear SVR model, the equation for a hyperplane can be defined as.

$$\hat{y} = xw^T + b \quad (5.2)$$

Here the weight  $w$  is a 1-by-5 row vector and  $b$  is a 17-by-1 column vector. The inner dot product of  $x$  and  $w$  results in a 17-by-1 column vector. During training, the original hyperplane is fitted the data using a linear regression model, then decision boundaries are defined to include points that are closest to the original hyperplane or the support vectors within the boundaries. Then the hyperplane is redefined based on the support vectors within the boundaries. With the boundary defined, the hyperplane that satisfies a linear SVR model is then

$$-c < \hat{y} = xw^T + b < c \quad (5.3)$$

Where the decision boundary is at a distance  $c$  from the hyperplane. The optimal hyperplane is one that minimizes the mean squared error (MSE) and predicts the maximum number of points with minimal error.

**Table 5.1:** Top 3 performing surrogate models trained using the training data

	SVR (Linear)	SVR (Quadratic)	SVR (Cubic)
RMSE	0.4913	0.3815	0.4172

As a performance metric, the RMSE is used to determine the quality of each type of SVR model. Results showed that the Quadratic Support Vector Regression model performed better than the other two SVR models in predicting the lift-to-drag ratio in the

training data set. The difference in the SVR models listed in Table 5.1 is the kernel function used on the data. Linear SVR models assume the data is linearly separable and utilize a linear mapping of the predictor variables. This is ineffective for nonlinear data sets. Hence, nonlinear kernel functions such as the polynomial kernels presented in Table 5.1 are used to map a linear hyperplane in the feature space into a nonlinear hyperplane in the design space.

### 5.3 Quadratic Kernel Support Vector Regression Model

With a RMSE of 0.3815, the Quadratic SVR model is used as the lift-to-drag prediction model in this research. The response variables are redefined using a quadratic kernel.

$$K(\vec{x}_i, \vec{x}_j) = \Phi(\vec{x}_i)^T \Phi(\vec{x}_j) = (\vec{x}_i^T \vec{x}_j + c)^2 \quad (5.4)$$

Here  $\vec{x}_i$  and  $\vec{x}_j$  are column vectors consisting of the 17 data points for the  $i^{th}$  and  $j^{th}$  response variable. The mapping of the predictor variables from design space into the feature space is defined by a feature map function  $\Phi(\cdot)$ . By expanding the right side of Equation 5.4 and separating the terms into functions of  $\vec{x}_i$  and  $\vec{x}_j$ , the separated functions define the feature map  $\Phi(\cdot)$  for each respective response variable.



### Support Vector Regression (Quadratic) Surrogate Model

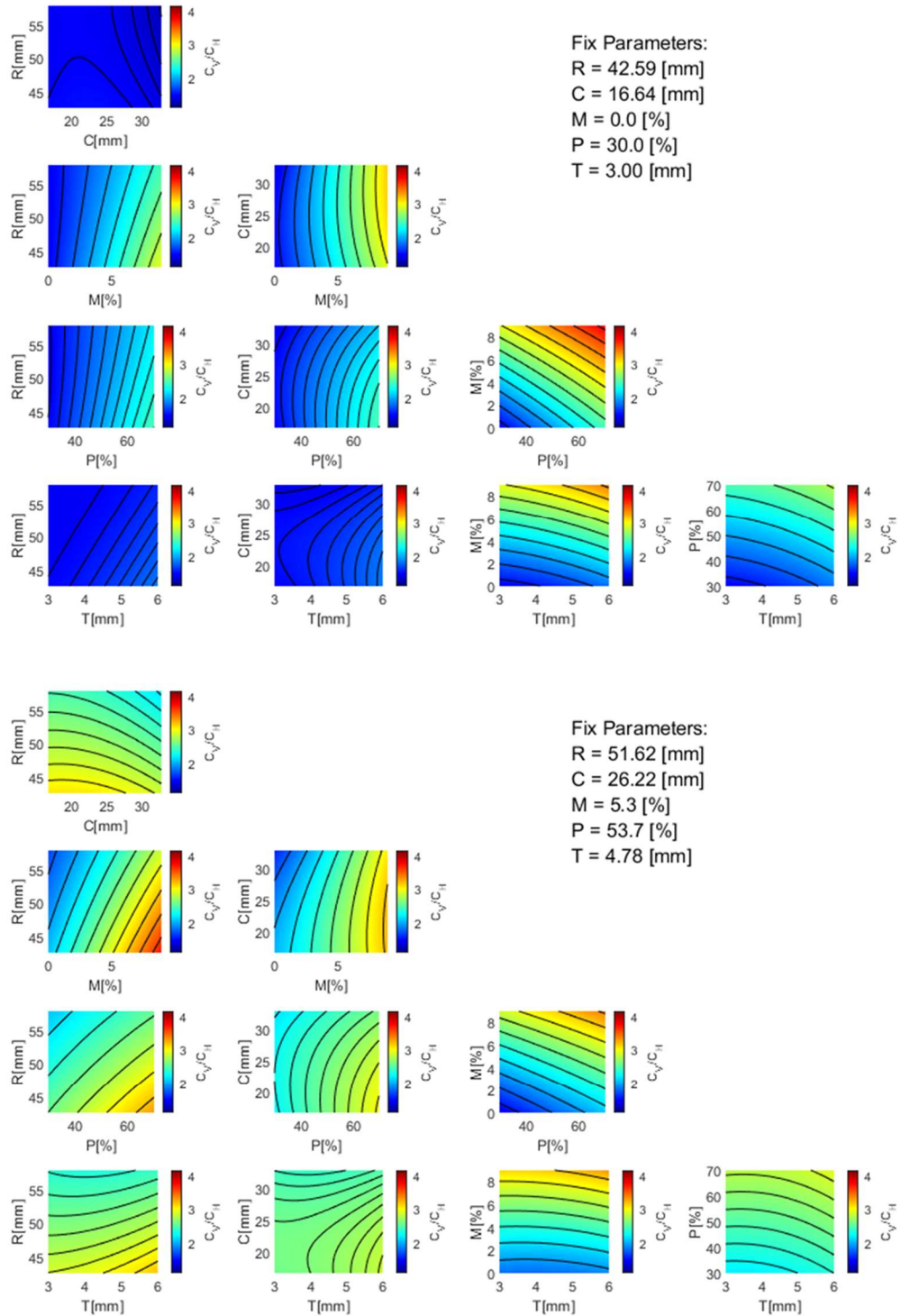


**Figure 5.2:** Contours of quadratic SVR predictions on lift-to-drag ratio. Since the surrogate is a high dimensional estimation model, it is impossible to show all the possible configurations of the response contour in a single 2D map.

After redefining the response variables in the feature space with the quadratic kernel function, linear hyperplanes fitted in the feature space using a linear SVR can be mapped back into the design space as quadratic functions of the response variables. The results of the quadratic SVR model are presented in Fig. 5.2. Each tile in the figure shows a contour of the lift-to-drag predictions made by the model versus two of the response variables that define the geometry of the wing. The remaining 3 response variables that are not presented in a single tile are set at a fixed value defined in the figure. Because the model resides in a high dimensional space, it is impossible to show all the possible configurations of the response variable in the format presented. Appendix C presents additional contours of the lift-to-drag ratio prediction with increasing fixed parameters after each frame.

The contours reveal geometric parameters that have the greatest influence in the lift-to-drag ratio response of the wing. Out of all the wing geometry parameters, the max camber  $M$  and location of the max camber along the chord  $P$  had the greatest impact on the magnitude of the lift-to-drag ratio. This can be seen in the contour gradient of the tiles. As a result of this observations, the wing design with the greatest max camber and max camber position within the design space is capable of generating a greater lift-to-drag ratio than a wing with a smaller camber. The other three parameters have less influence on the magnitude of the lift-to-drag ratio as the contour gradient only varies slightly.

Appendix C presents additional contour maps as the fixed parameters are increased. As additional indication of the influence  $M$  and  $P$  have on the lift-to-drag ratio, increasing the fixed  $M$  and  $P$  values lead to a greater contour gradient in the tiles that are

plotted against the two parameters. Each contour plot with a geometric parameter paired with  $M$  or  $P$  showed a greater change in lift-to-drag magnitude as the fixed parameters are increased, whereas parameters with less influence showed a smaller level of contour gradient.

## 5.4 Optimal Wing Design using Interior Point Algorithm

The trained surrogate model presented in Section 5.3 provide rapid estimates of the lift-to-drag ratio for all possible wing design configurations within the design space. The color contour in each tile in Fig. 5.2 show regions of high lift-to-drag ratio as the wing geometry parameters are varied. With this model of the CFD experiments, the task of evaluating the design space for optimal lift-to-drag ratio values become easier. The goal of the optimization problem presented here is to find the maximum lift-to-drag ratio using the surrogate model as the objective function. The problem can also be expressed as finding the minimum of the negative surrogate model values given that the design variable is bounded within the minimum and maximum design space values specified in Table 3.1.

$$\min_x(-\hat{f}(x)) \text{ subject to } \begin{cases} x - x_{min} \geq 0 \\ x_{max} - x \geq 0 \end{cases}, \text{ where } \hat{f}: \mathbb{R}^5 \rightarrow \mathbb{R} \quad (5.5)$$

Here, the surrogate model function is  $\hat{f}(x)$  and  $x$  is the design variable in a 5-dimensional design space. The elements in  $x$  are the 5 wing geometry parameters defined before. The optimization algorithm used for the problem is the interior-point method [23] with two constraint equations that define the bounds of the design space. With the objective and constraint equations defined, the interior-point method solves the inequality-constrained optimization problem by converting it into an unconstrained

objective function using a logarithmic barrier function. For the optimization problem presented here, this barrier function is

$$B(x, \mu) = \hat{f}(x) - \mu(\log(x - x_{min}) + \log(x_{max} - x)) \quad (5.6)$$

In the barrier function (5.6), the barrier parameter  $\mu$  converges to zero as the minimum of  $B(x, \mu)$  approaches the solution of the optimization problem presented in (5.5).

Additionally, two Lagrangian multiplier variables  $\lambda_1$  and  $\lambda_2$  are introduced for each of the constraint equations and two new conditions are defined as

$$\lambda_1(x - x_{min}) = \mu \quad (5.7)$$

$$\lambda_2(x_{max} - x) = \mu \quad (5.8)$$

Once Equations 5.7 and 5.8 are applied to 5.6, the goal is to find those  $x$  and  $\lambda$  such that the gradient of the barrier function is equal to zero,  $\nabla B = 0$ . The results of the interior-point optimization approach are depicted in Fig. 5.3. The initial guess of the optimal solution was set at the halfway point between the maximum and minimum boundary values.

Interior Point Optimal Design Search,  $C_V/C_H^* = 4.29$

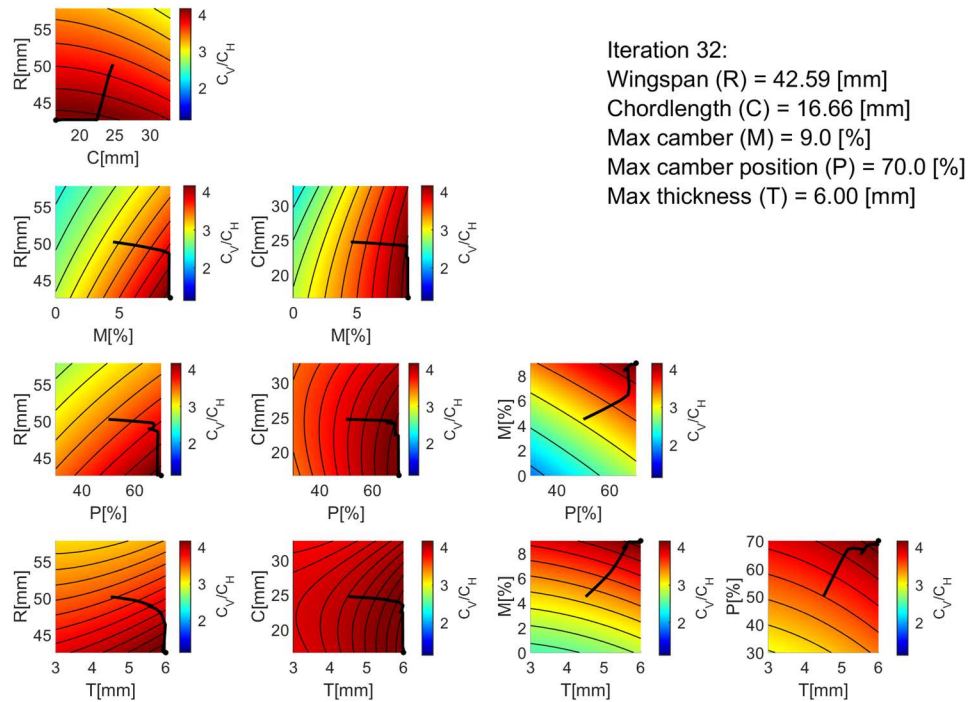


**Figure 5.3:** Design space optimal point search using interior point method. Optimal point found after 32 iterations. The black line shows the path taken by the search algorithm to find the optimal point.

$$\left(\frac{C_V}{C_H}\right)^* = 4.29$$

The optimization algorithm identified a maximum lift-to-drag ratio of 4.29 for a wing with a wingspan of 42.59 [mm], chord length of 16.66 [mm], max camber of 9%, camber position of 70%, and max thickness of 6 [mm]. The contour map show regions of greater lift-to-drag ratio near the boundary lines of the design space, thus as expected, the optimal search algorithm is observed to step closer toward the boundary line after each iteration.

To determine the accuracy of the surrogate model in predicting the lift-to-drag ratio of an off-design point, the wing geometry identified to produce the maximum ratio was tested in a final CFD simulation and the results were compared to the surrogate model prediction. Fig. 5.4 depicts the optimal forewing design which the surrogate model estimated to produce a lift-to-drag ratio of 4.29.

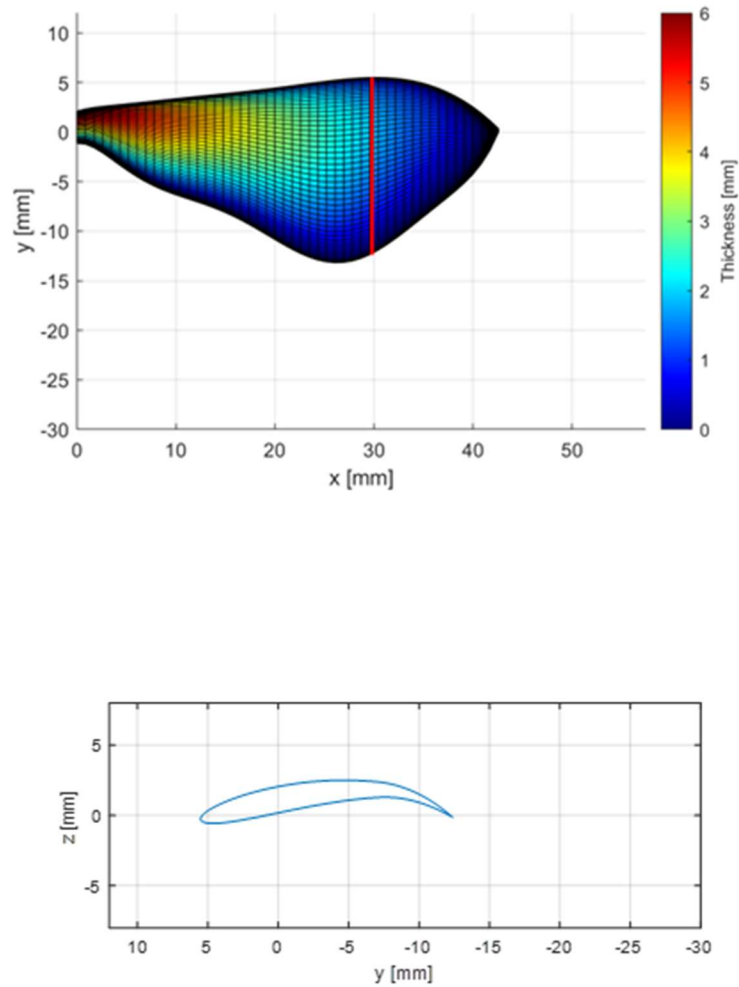


**Figure 5.4:** Optimal wing design estimated by surrogate model.

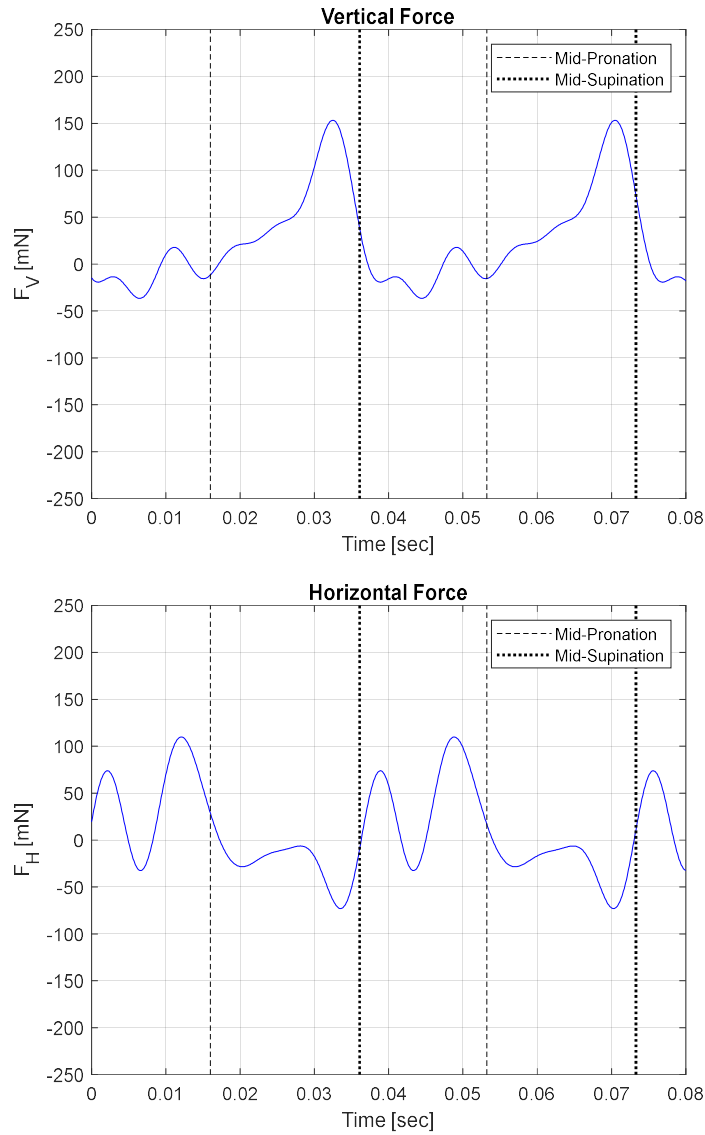


**Figure 5.5:** Vertical and horizontal force CFD results for the optimal wing design.

$$\left(\frac{C_V}{C_H}\right)_{CFD} = 3.8541$$

Compared to the predicted lift-to-drag ratio for the optimal wing design, the CFD experiment on the same wing produced a lift-to-drag ratio that was 10% smaller than the predicted.

## **Chapter 6 Conclusion**



The work presented in this thesis investigates a surrogate modeling approach for optimizing the forewing design of a *Manduca Sext L.* inspired FWMAV. An experiment involving wing geometry modeling, flapping kinematic modeling, and the use of computational aerodynamic simulations is designed to gather data on the aerodynamic performance of a sample of 20 wing designs. The analysis of 17 out of the 20 wing designs in an aerodynamic simulation concluded that sample 11, the wing depicted in Fig 6.1, performed the best out of all the wing designs.

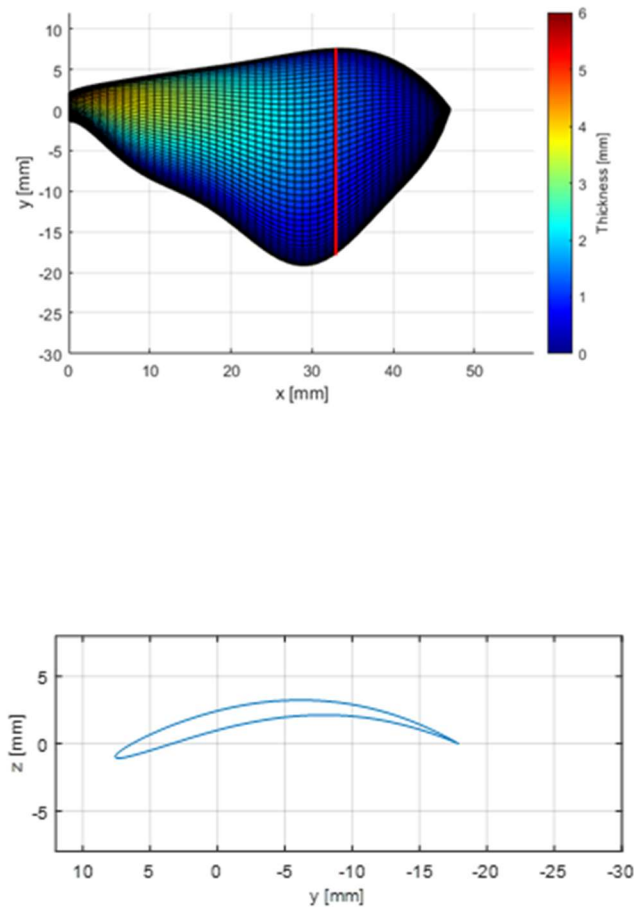


**Figure 6.1:** Sample 11 wing design. The wing depicted has the following geometric parameters:  $R = 47$  [mm],  $C = 23$  [mm],  $M = 8.8\%$ ,  $P = 49\%$ ,  $T = 4.8$  [mm].

Additionally, sample 11 showed better performance in the CFD simulation even compared to the optimal wing design that was predicted by the surrogate model. Interestingly, the cross-section geometry of sample 11 more closely resembles that of the actual hawk moth than the other samples. The calculated aerodynamic forces for sample 11 were  $\bar{F}_V = 22.1 [mN]$ ,  $\bar{F}_H = 5.29 [mN]$ , and  $\frac{\bar{C}_V}{\bar{C}_H} = 4.17$ . Compared to the results on rigid wing simulations in [11] these results showed better performance in generating lift and minimizing the average horizontal force in hovering flight.

In Chapter 3, the kinematic equations of the flapping motion for a Scotch yoke flapping mechanism in hovering flight, the hawk moth flapping in hovering flight, and the hawk moth flapping in forward flight are derived for a 3D wing motion. Combined with the wing geometry modeling performed in Chapter 2, CFD simulations for the three types of flapping cases were investigated in Chapter 4. For the three flapping cases a control sample of the wing geometry was used in the experiment. The control sample is a wing cross section symmetric about the biological mean camber line of the wing with a max thickness at the root of 3 [mm]. Comparing the 2D CFD results with existing literature on the 3D CFD simulations of the hawk moth in hovering flight, it was found that the trend in the vertical force from the 2D simulations agreed with that of the 3D simulations, but horizontal force trends differed significantly. Time averaged force results were compared for the Scotch yoke hovering flight case, the hawk moth hovering case, and the 3D hovering case in [11]. Results showed a similar magnitude for the vertical forces, but horizontal forces differed significantly. In conclusion, these results suggest that 3D aerodynamic mechanisms such as wingtip vortices and the variation of leading-edge vortices along the span of the wing contribute more to the variation in horizontal

forces than it does vertical forces. To fully assess the true aerodynamic efficiency of the wing designs in hovering flight, a higher fidelity CFD model that accounts for 3D aerodynamic mechanisms is recommended for future experiments.

In Chapter 5, a surrogate model trained using a quadratic Support Vector Regression model revealed the lift-to-drag sensitivity to variations in wing geometric parameters. By inspecting the contour gradient of the surrogate model predictions, it was revealed that the maximum camber ( $M$ ) and location of the max camber along the chord ( $P$ ) had the greatest influence in the magnitude of the lift-to-drag ratio on the wing. To further validate this conclusion, it is recommended that future aerodynamic experiments be conducted on wings with a larger camber near the trailing edge of the wing, and the results compared to that of symmetrical wings in hovering flight.

During the surrogate model training process, three candidate SVR models with different kernel functions were compared based on their RMSE values. Out of the three, the quadratic SVR performed the best at predicting the train data set with a RSME value of 0.3815 and an R-squared value of 0.62. The R-squared value is a measure of the level of variance that is explained by the model. A value of 1 indicates all the variance in the data are explained by the model whereas lower levels indicate there are additional variations in the data that the model did not account for. An R-squared value of 0.62 suggests there are other unaccounted for factors in the experiments that contributed to the variation in lift-to-drag ratio within the wing design space. Because of this, further investigations into the unsteady aerodynamic mechanisms should be performed to visually assess the effects of that wing geometry parameters have on the aerodynamic efficiency of wing. Additionally, improvements to the prediction performance can be

achieved with a larger sample size as a greater sample may reveal additional information about the variance in the training data set.

The scope of this research reveals preliminary capabilities of the surrogate modeling approach in rapidly assessing the aerodynamic performance of specific wing designs on a hawk moth inspired FWMAV in hovering flight. Using the methods described in this research, the trained SVR surrogate model was able to reveal the sensitivity of the lift-to-drag ratio from variations in wing geometric parameters, with the greatest impact on aerodynamic performance coming from variations in the max camber and location of max camber on the wing. However, the optimal wing prediction made by the surrogate model showed a 10% error in predicting the lift-to-drag ratio when compared to CFD results on the same wing. Thus, future improvements can be made to build more accurate prediction models trained on higher fidelity simulation models. To fully assess the effects that the wing geometry has on the aerodynamic performance, an experiment with a larger sample size must be conducted and higher fidelity computational simulations that incorporate both 3D aerodynamics and fluid structure interactions between the wing and the air must be utilized.

## **Chapter 7 Future Work**

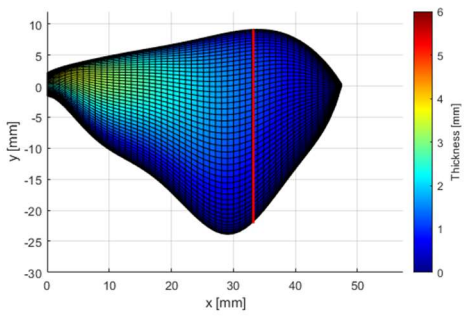
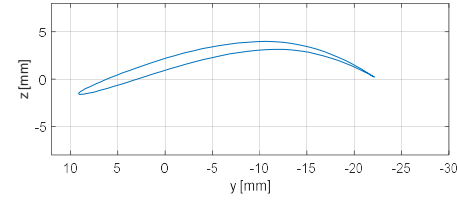
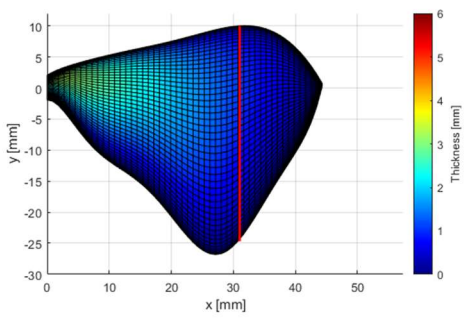
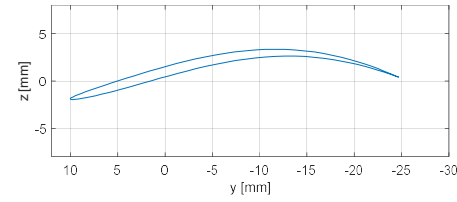
The current experiment presented in this thesis lacks the inclusion of significant physical properties. For the moth forewing and flapping kinematic modeling process discussed, inertial properties on the wing need to be considered for higher fidelity models. As the wing geometry changes, the total mass of the wing changes based on the mass density distribution on the wing. Additionally, based on the density distribution on the wing, the kinematic model of the flapping motion also changes. A greater mass density toward the leading edge of the wing causes the rotational axis of the wing to shift toward the leading edge. As revealed in [8], this model of the rotational axis turned out to perform better at mimicking the biological wing motion compared to the rotational axis in this thesis in that it aided in passive pronation and supination of the wing.

Future computational aerodynamic simulations should consider the inclusion of fluid structure interaction models. Incorporating structural properties of the wing such as flexural and torsional stiffness build higher fidelity into the simulation model as the moth wing itself is not a rigid structure. The addition of extra parameters such as inertial and structural properties of the wing add on to the complexity of the simulation model and create a more complex wing design space to be investigated. Hence in future work, more wing design configurations will have to be sampled from the design space to effectively train future surrogate models.

An alternative option to lessen the complexity of the experiments would be to conduct real world experiments as opposed to complex simulated fluid structure interaction experiments. Real world wing models with varying inertial, geometric, and structural properties can be fabricated in the Bioinspired Robotics Lab at Case Western Reserve University, and their performance can be evaluated in wind tunnel experiments.

A wind tunnel compatible flapping mechanism that mimics the flapping motion on the hawk moth can be fabricated to account for all degrees of motion in the flapping wing. For small wing testing in a wind tunnel, a particle image velocimetry (PIV) setup for flow visualization can be used for measuring fluid velocity on the wing. An experimental setup of this type has been developed by [3]. With that said, the most challenging part of transitioning the experiment from a simulated environment to a real-world environment would be designing a flapping mechanism for the wind tunnel that accounts for the 4 degrees of motion on the hawk moth wing.

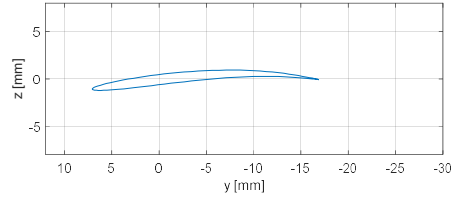
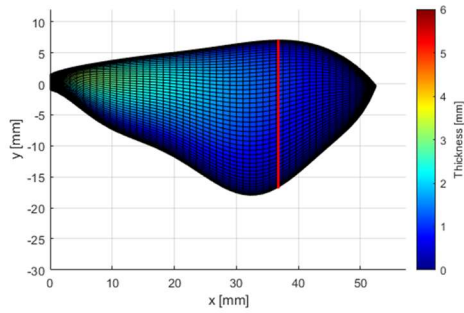
# Appendix A: Latin Hypercube Sampled Wing Geometries

<b>Sample 1 (Failed to Converge)</b>				
$R = 47.2 [mm]$	$C = 27.7 [mm]$	$M = 7.8\%$	$P = 63\%$	$T = 3.9 [m]$
				
<b>Sample 2 (Failed to Converge)</b>				
$R = 44.3 [mm]$	$C = 30.4 [mm]$	$M = 3.9\%$	$P = 58\%$	$T = 3.4 [mm]$
				



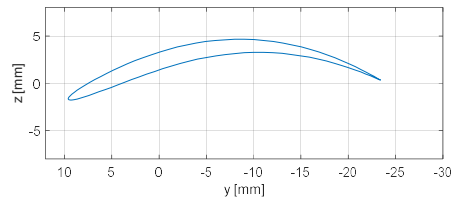
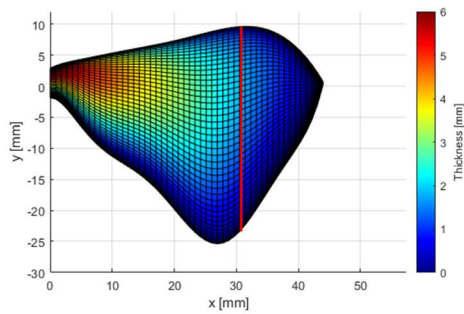
### Sample 3

$R = 52.5$  [mm] |  $C = 21.7$  [mm] |  $M = 1.6\%$  |  $P = 33\%$  |  $T = 3.5$  [mm]



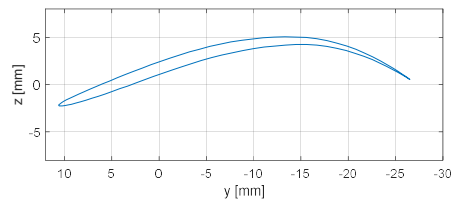
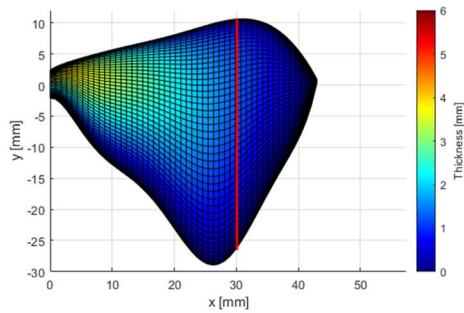
### Sample 4

$R = 43.9$  [mm] |  $C = 29.1$  [mm] |  $M = 8.2\%$  |  $P = 46\%$  |  $T = 5.9$  [mm]



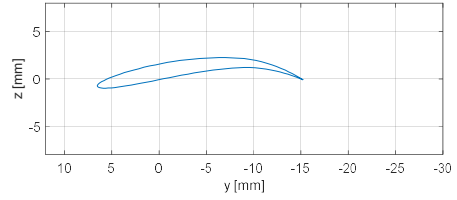
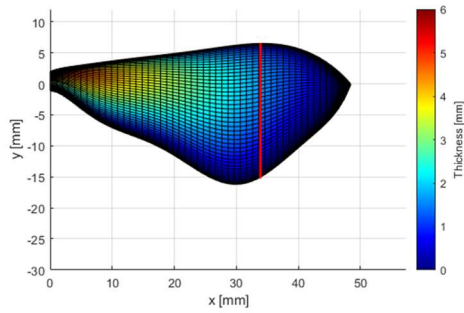
### Sample 5 (Failed to Converge)

$R = 43.0$  [mm] |  $C = 32.2$  [mm] |  $M = 6.9\%$  |  $P = 70\%$  |  $T = 4.2$  [mm]



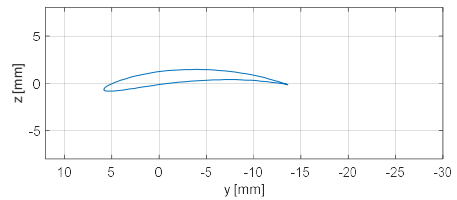
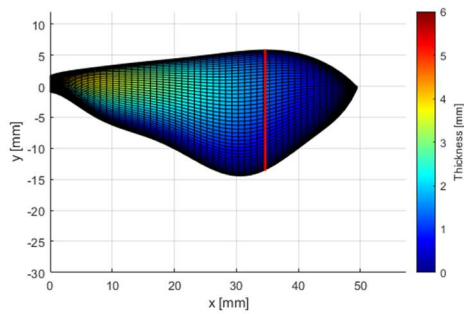
### Sample 6

$R = 48.4$  [mm] |  $C = 19.9$  [mm] |  $M = 6.6\%$  |  $P = 67\%$  |  $T = 5.3$  [mm]



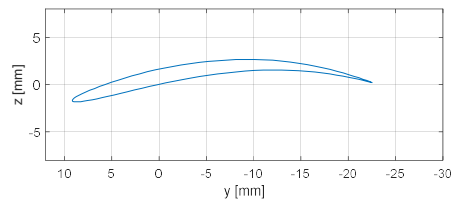
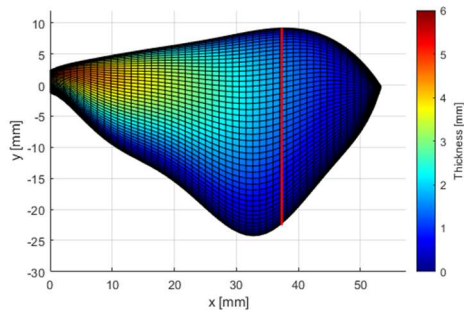
### Sample 7

$R = 49.5$  [mm] |  $C = 17.9$  [mm] |  $M = 4.7\%$  |  $P = 41\%$  |  $T = 4.5$  [mm]



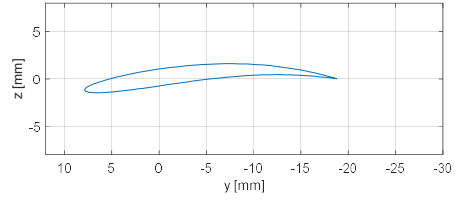
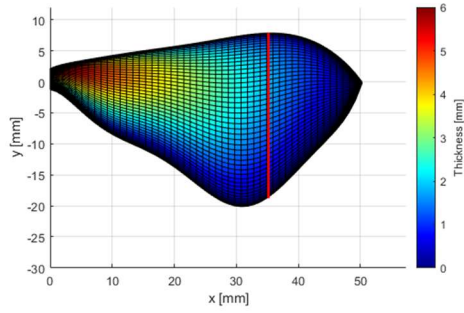
### Sample 8

$R = 53.3$  [mm] |  $C = 28.0$  [mm] |  $M = 4.4\%$  |  $P = 38\%$  |  $T = 5.1$  [mm]



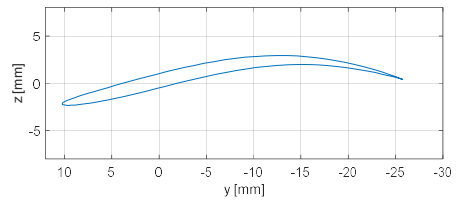
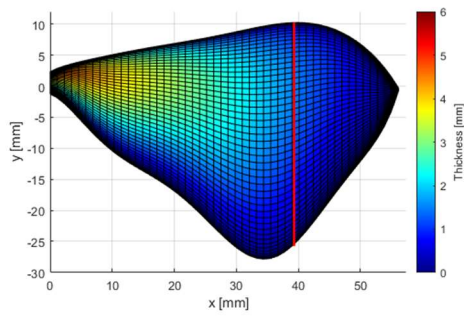
### Sample 9

$R = 50.3 [mm]$  |  $C = 24.0 [mm]$  |  $M = 1.8\%$  |  $P = 35\%$  |  $T = 5.8 [mm]$



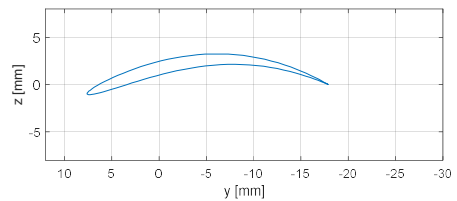
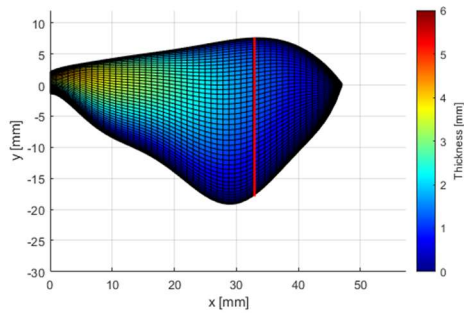
### Sample 10

$R = 56.1 [mm]$  |  $C = 31.3 [mm]$  |  $M = 3.2\%$  |  $P = 54\%$  |  $T = 4.8 [mm]$



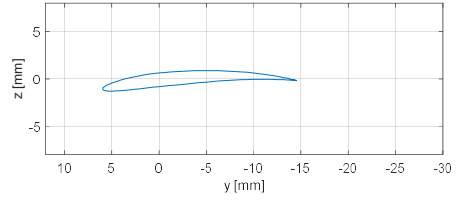
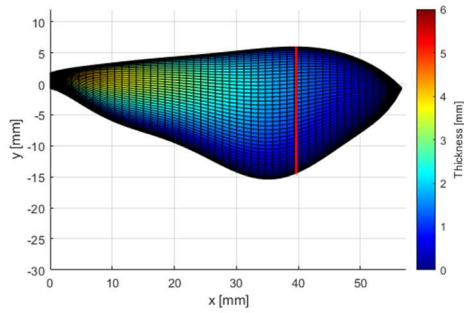
### Sample 11

$R = 47.0 [mm]$  |  $C = 23.0 [mm]$  |  $M = 8.8\%$  |  $P = 49\%$  |  $T = 4.8 [mm]$



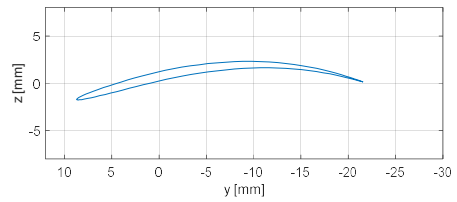
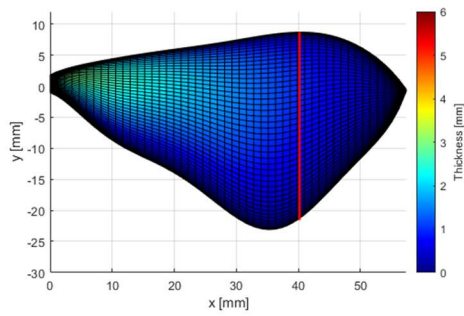
### Sample 12

$R = 56.7 [mm]$  |  $C = 18.8 [mm]$  |  $M = 2.8\%$  |  $P = 31\%$  |  $T = 4.7 [mm]$



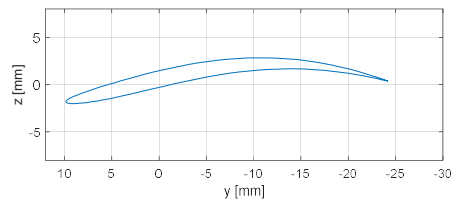
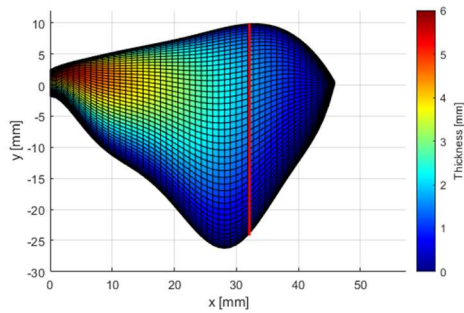
### Sample 13

$R = 57.4 [mm]$  |  $C = 26.9 [mm]$  |  $M = 5.2\%$  |  $P = 42\%$  |  $T = 3.1 [mm]$



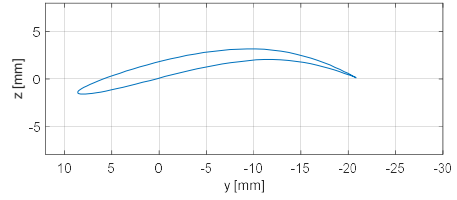
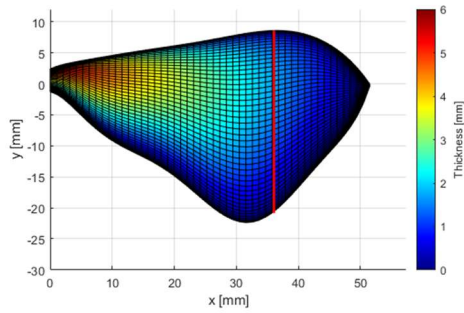
### Sample 14

$R = 45.9 [mm]$  |  $C = 29.9 [mm]$  |  $M = 2.3\%$  |  $P = 45\%$  |  $T = 5.6 [mm]$



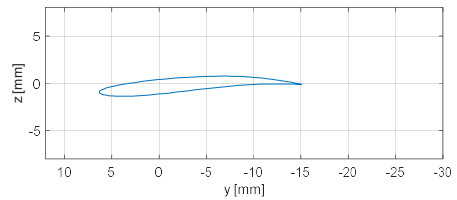
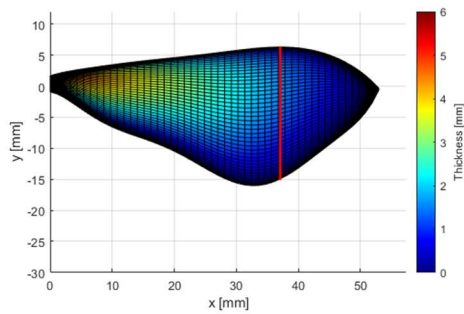
### Sample 15

$R = 51.5 [mm]$  |  $C = 26.2 [mm]$  |  $M = 6.2\%$  |  $P = 61\%$  |  $T = 5.5 [mm]$



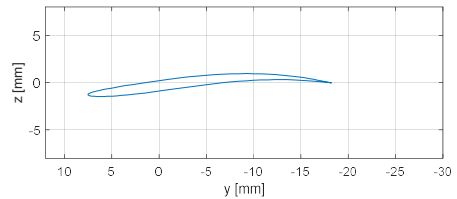
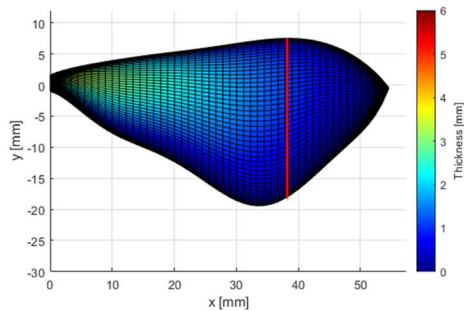
### Sample 16

$R = 52.9 [mm]$  |  $C = 19.6 [mm]$  |  $M = 0.7\%$  |  $P = 64\%$  |  $T = 4.9 [mm]$



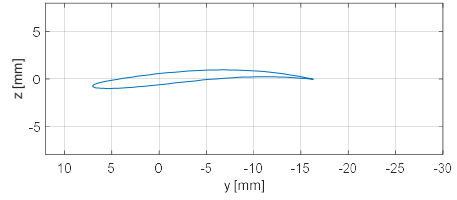
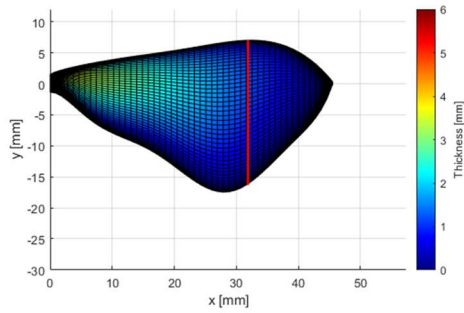
### Sample 17

$R = 54.5 [mm]$  |  $C = 23.2 [mm]$  |  $M = 1.0\%$  |  $P = 51\%$  |  $T = 3.6 [mm]$



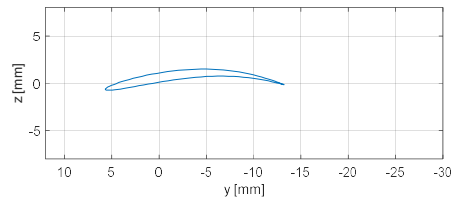
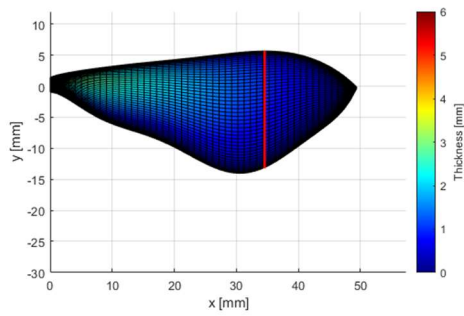
### Sample 18

$R = 45.5 [mm]$  |  $C = 21.3 [mm]$  |  $M = 0.4\%$  |  $P = 36\%$  |  $T = 3.8 [mm]$



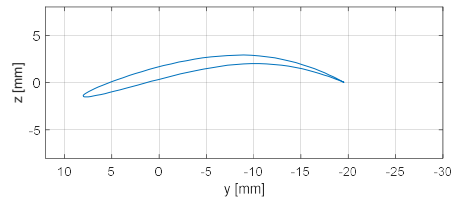
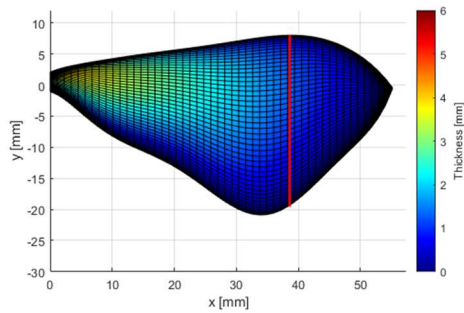
### Sample 19

$R = 49.4 [mm]$  |  $C = 17.4 [mm]$  |  $M = 5.8\%$  |  $P = 53\%$  |  $T = 3.2 [mm]$



### Sample 20

$R = 55.1 [mm]$  |  $C = 24.7 [mm]$  |  $M = 7.5\%$  |  $P = 56\%$  |  $T = 4.2 [mm]$

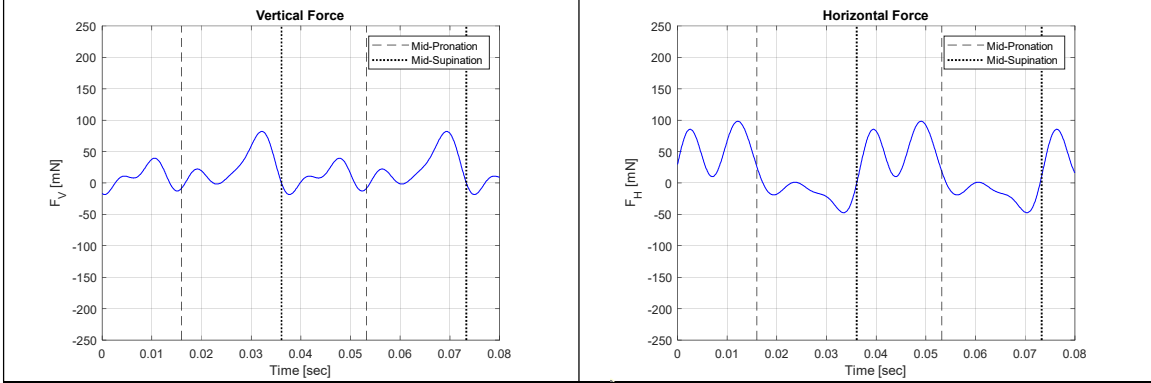


## Appendix B: CFD Results on Sampled Wing

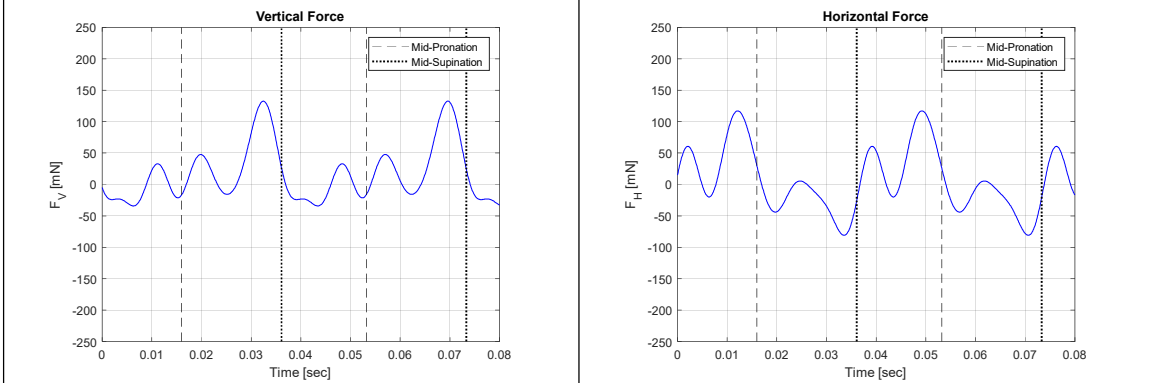
### Geometries

Sample No.	$\bar{F}_V$ (mN)	$\bar{F}_H$ (mN)	$\bar{C}_V$	$\bar{C}_H$	$\frac{\bar{C}_V}{\bar{C}_H}$
Control	21.0	10.6	1.7302	0.8763	1.9744
3	18.9	16.7	1.2654	1.1182	1.1316
4	19.2	5.38	1.1439	0.3205	3.5691
6	18.7	5.49	1.4808	0.4352	3.4026
7	17.4	7.52	1.5026	0.6477	2.3199
8	29.4	13.9	1.4989	0.7116	2.1064
9	21.1	10.1	1.3324	0.6398	2.0825
10	35.4	19.2	1.5347	0.8325	1.8435
11	22.1	5.29	1.5523	0.3720	4.1728
12	22.1	12.16	1.5869	0.8728	1.8182
13	30.6	12.4	1.5122	0.6119	2.4713
14	28.0	13.6	1.5605	0.7582	2.0582
15	25.8	7.16	1.4589	0.4043	3.6085
16	22.8	9.67	1.6826	0.7121	2.3629
17	24.7	12.1	1.4867	0.7323	2.0302
18	23.0	13.0	1.8110	1.0246	1.7675
19	18.9	6.70	1.6773	0.5944	2.8218
20	17.4	9.79	0.9722	0.5482	1.7734

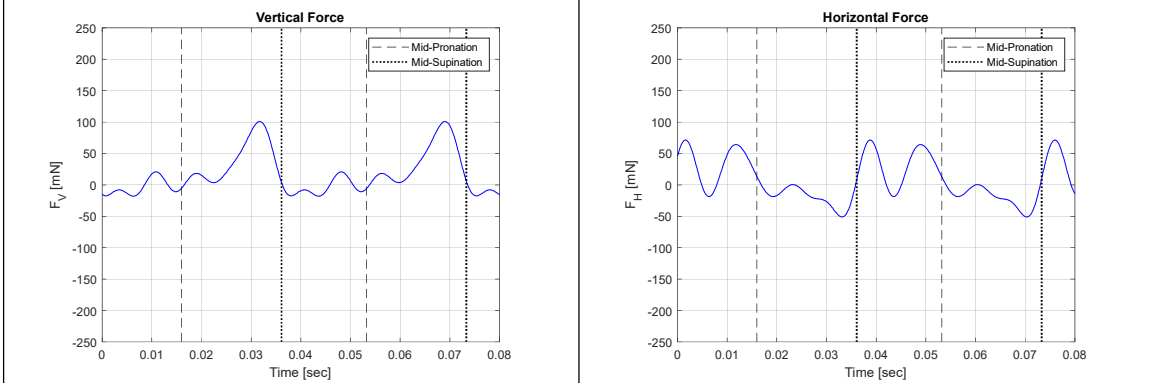
### Sample 3



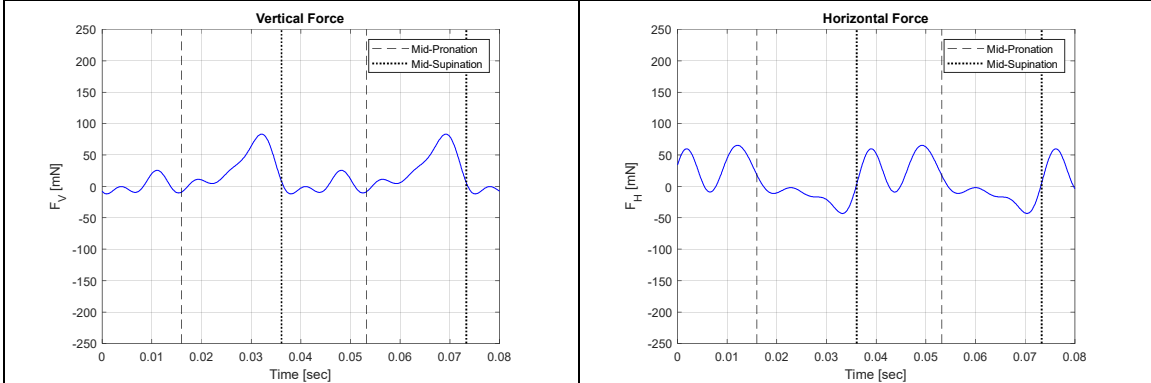
### Sample 4



### Sample 6

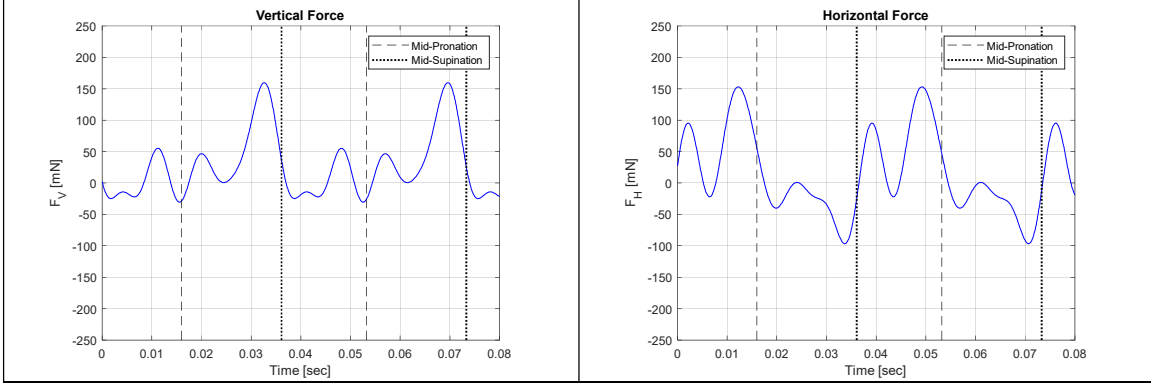


### Sample 7

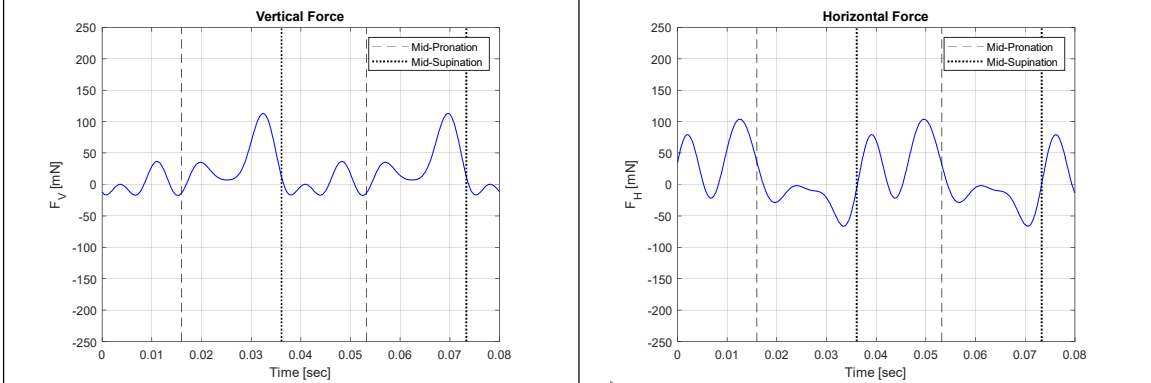




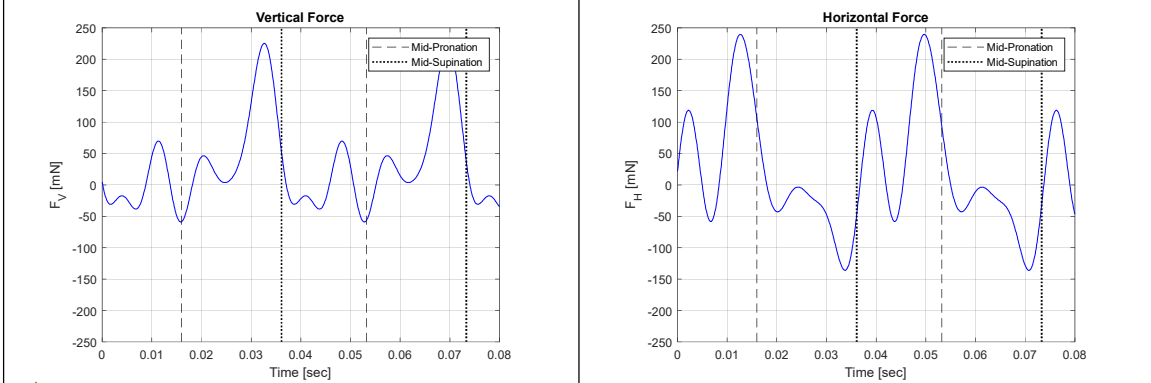
### Sample 8



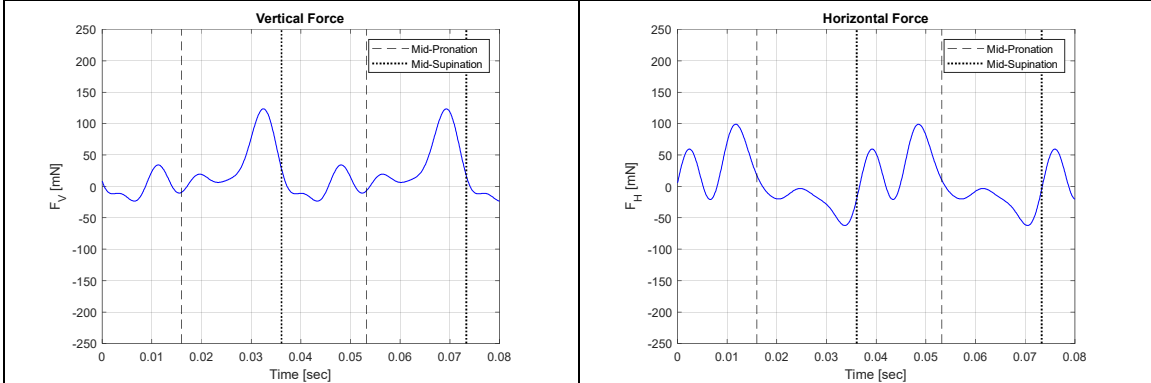
### Sample 9



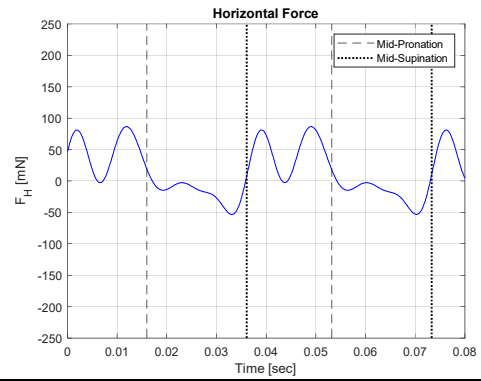
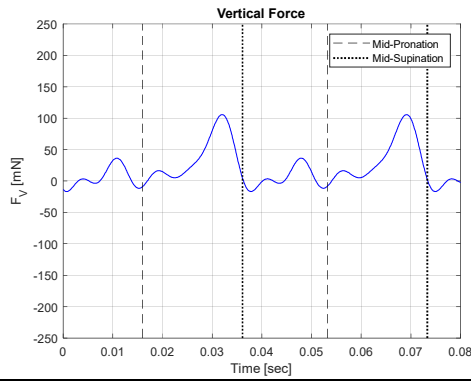
### Sample 10



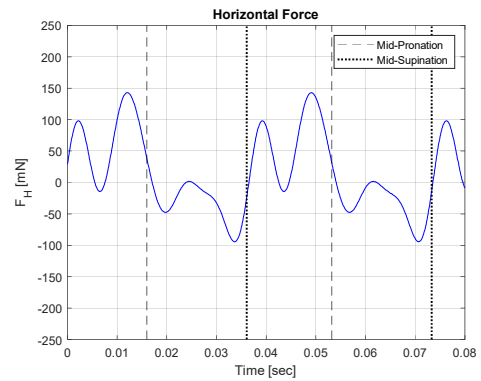
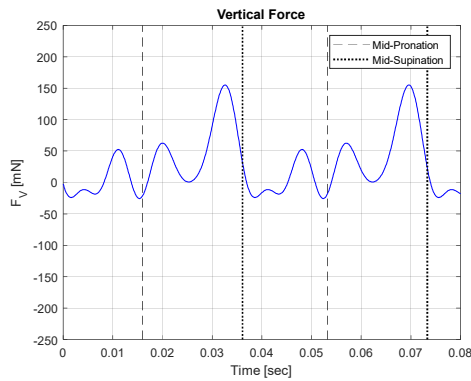
### Sample 11



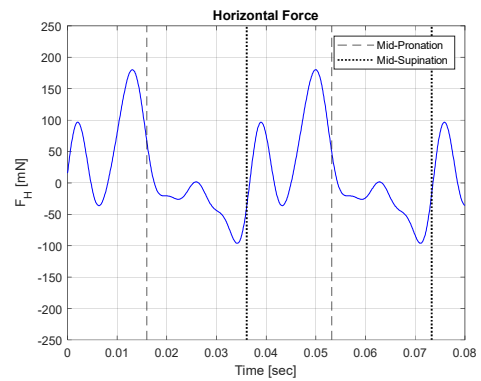
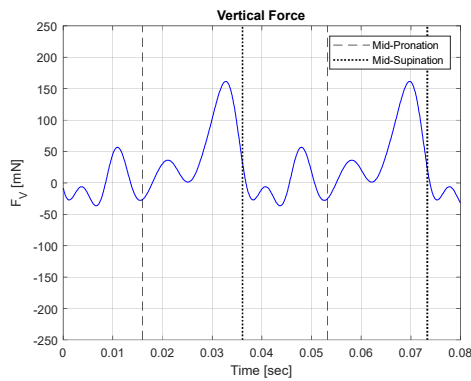
### Sample 12



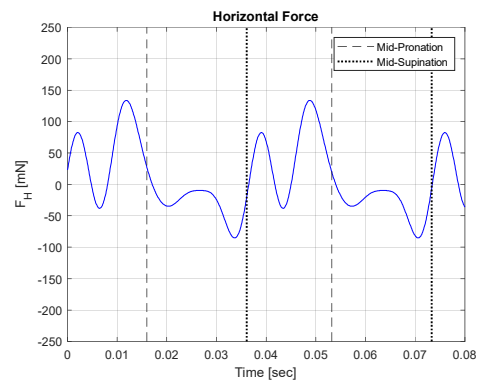
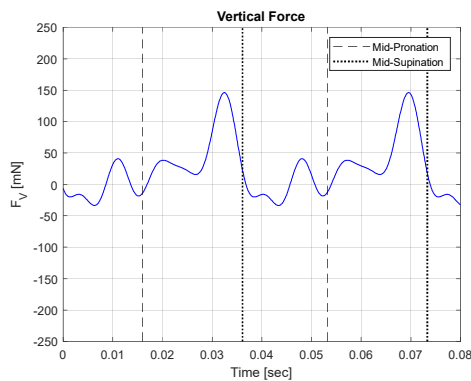
### Sample 13



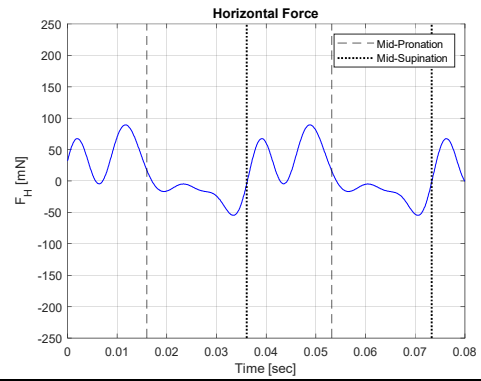
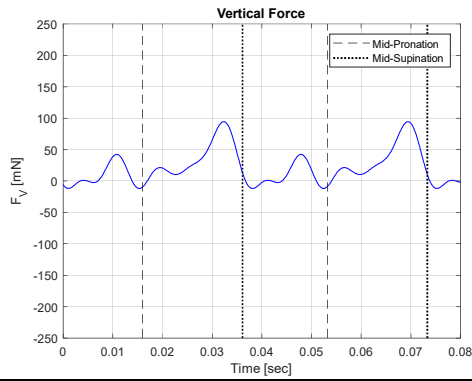
### Sample 14



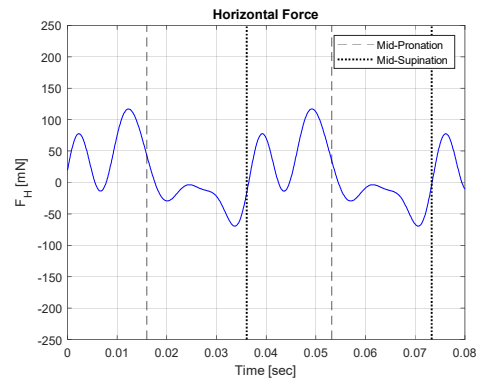
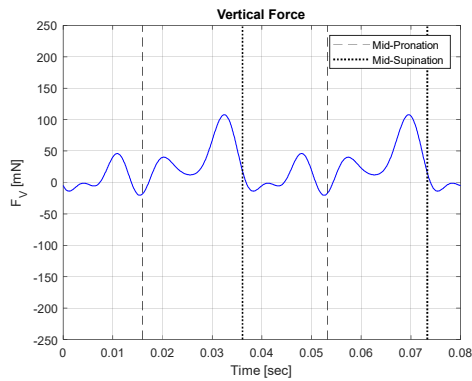
### Sample 15



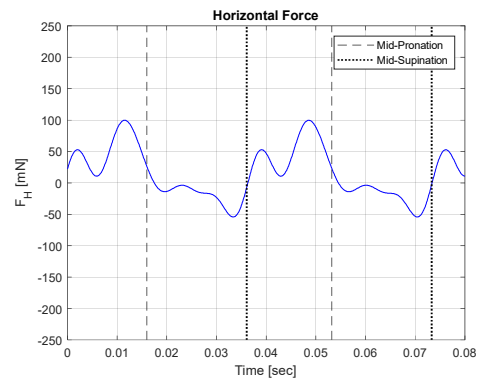
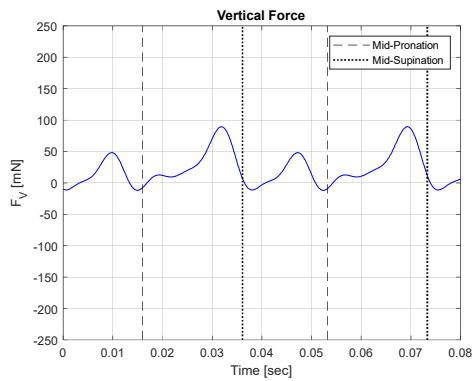
### Sample 16



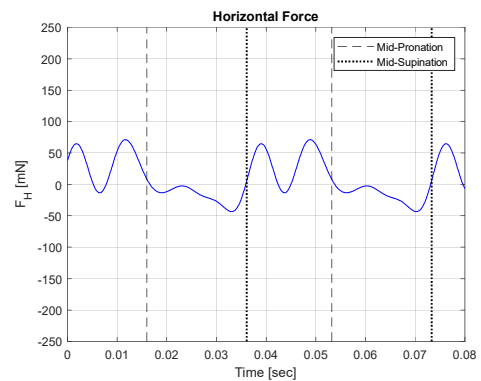
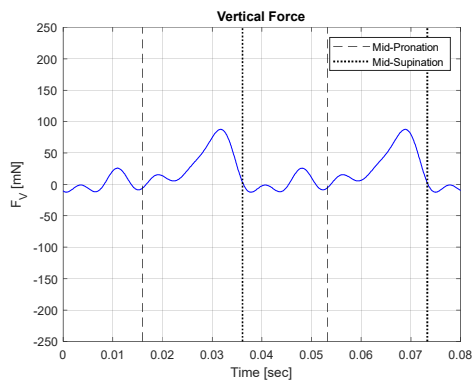
### Sample 17



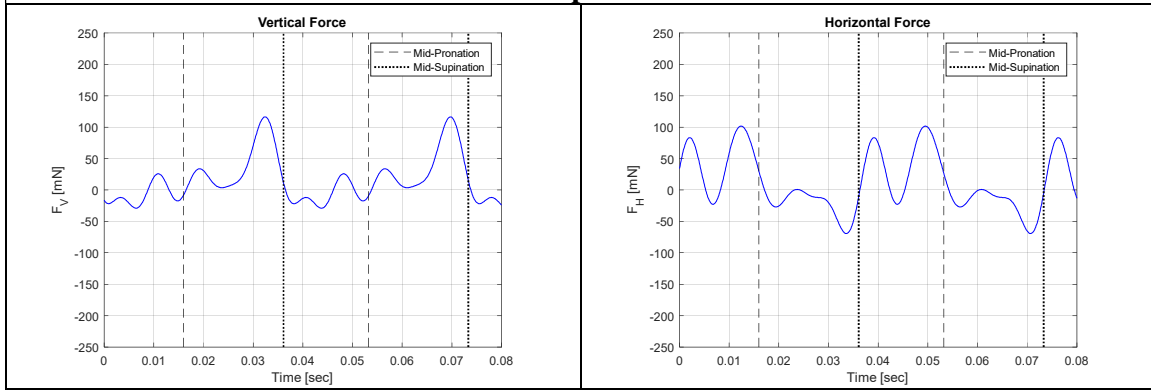
### Sample 18



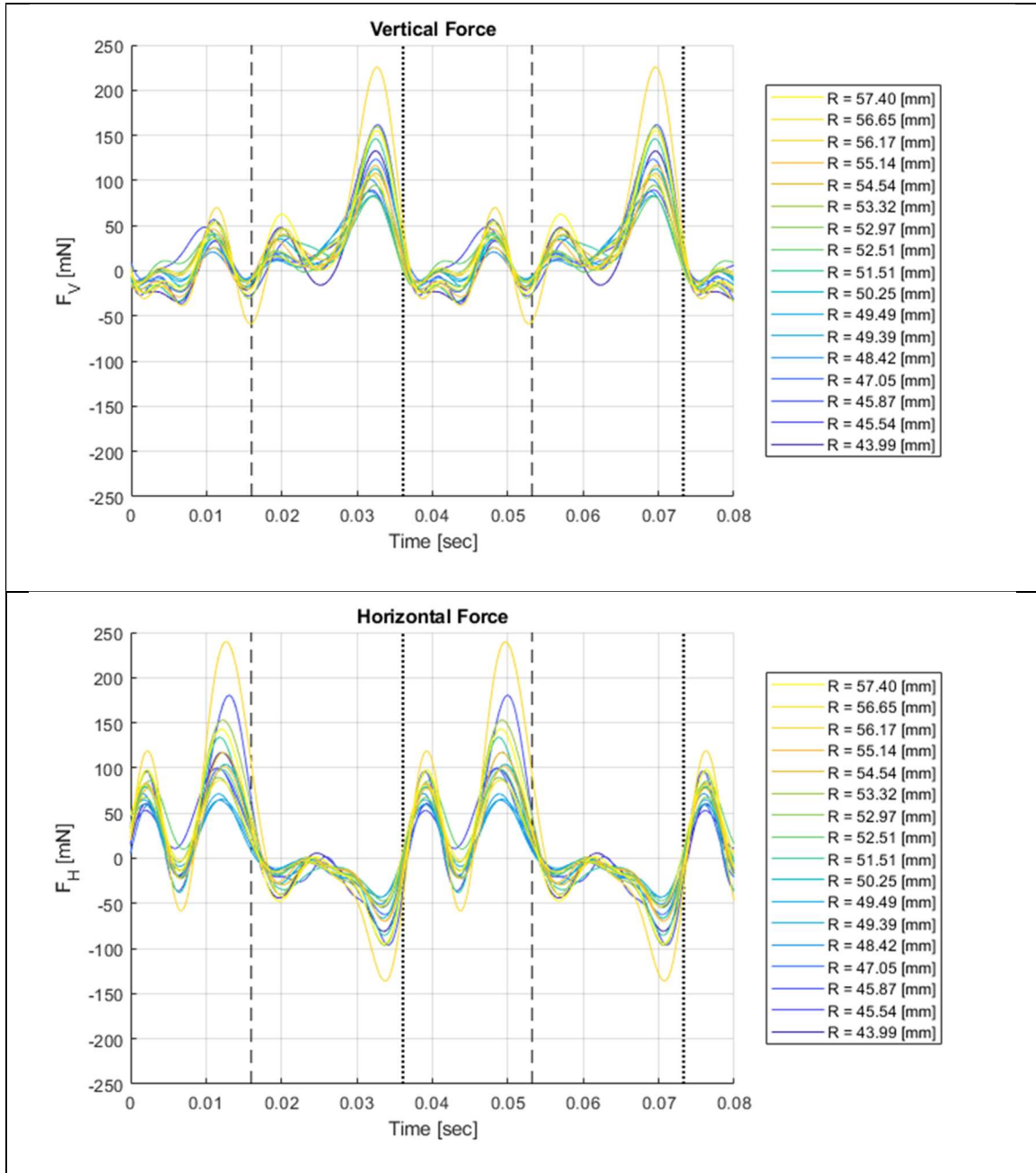
### Sample 19

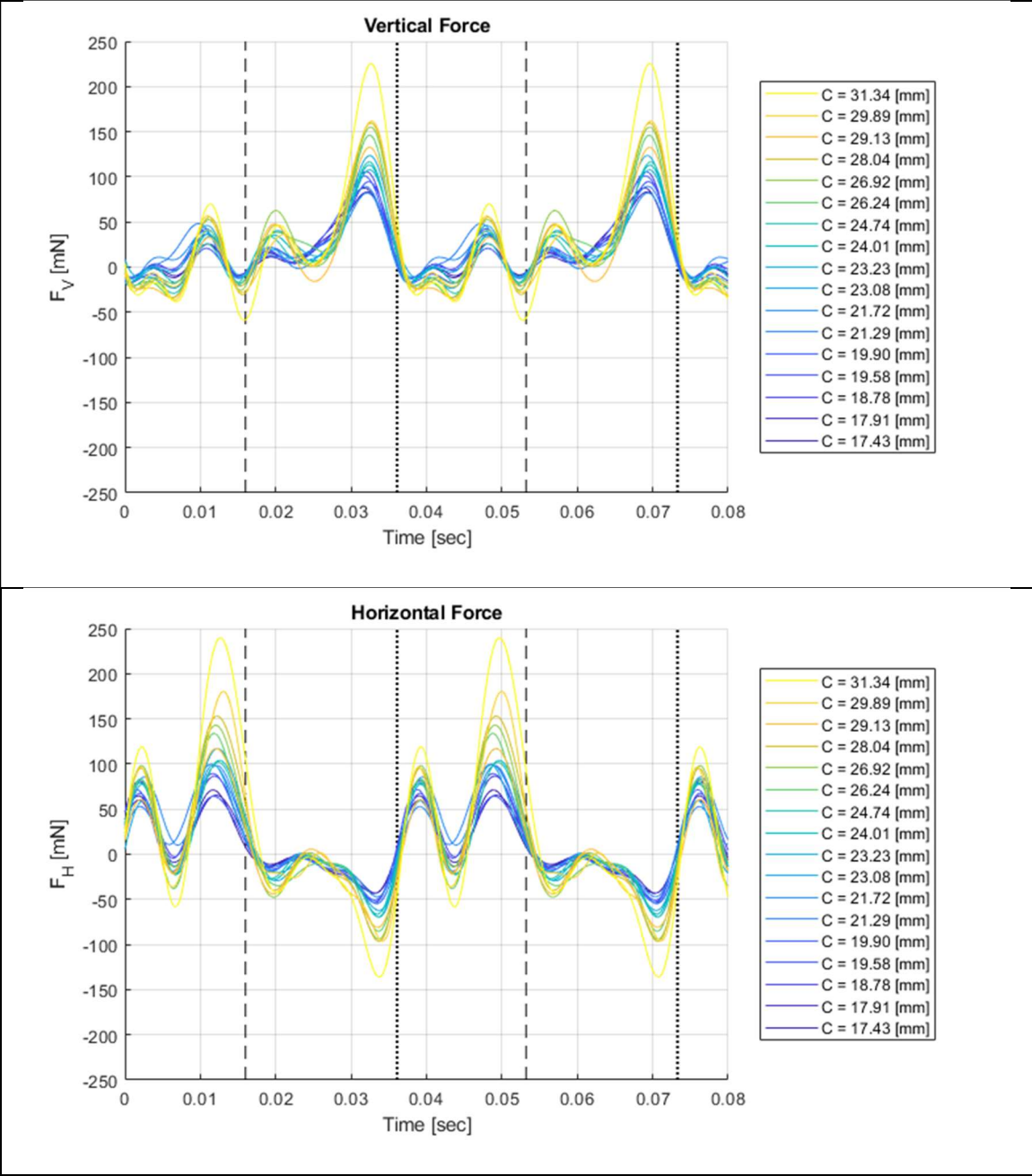


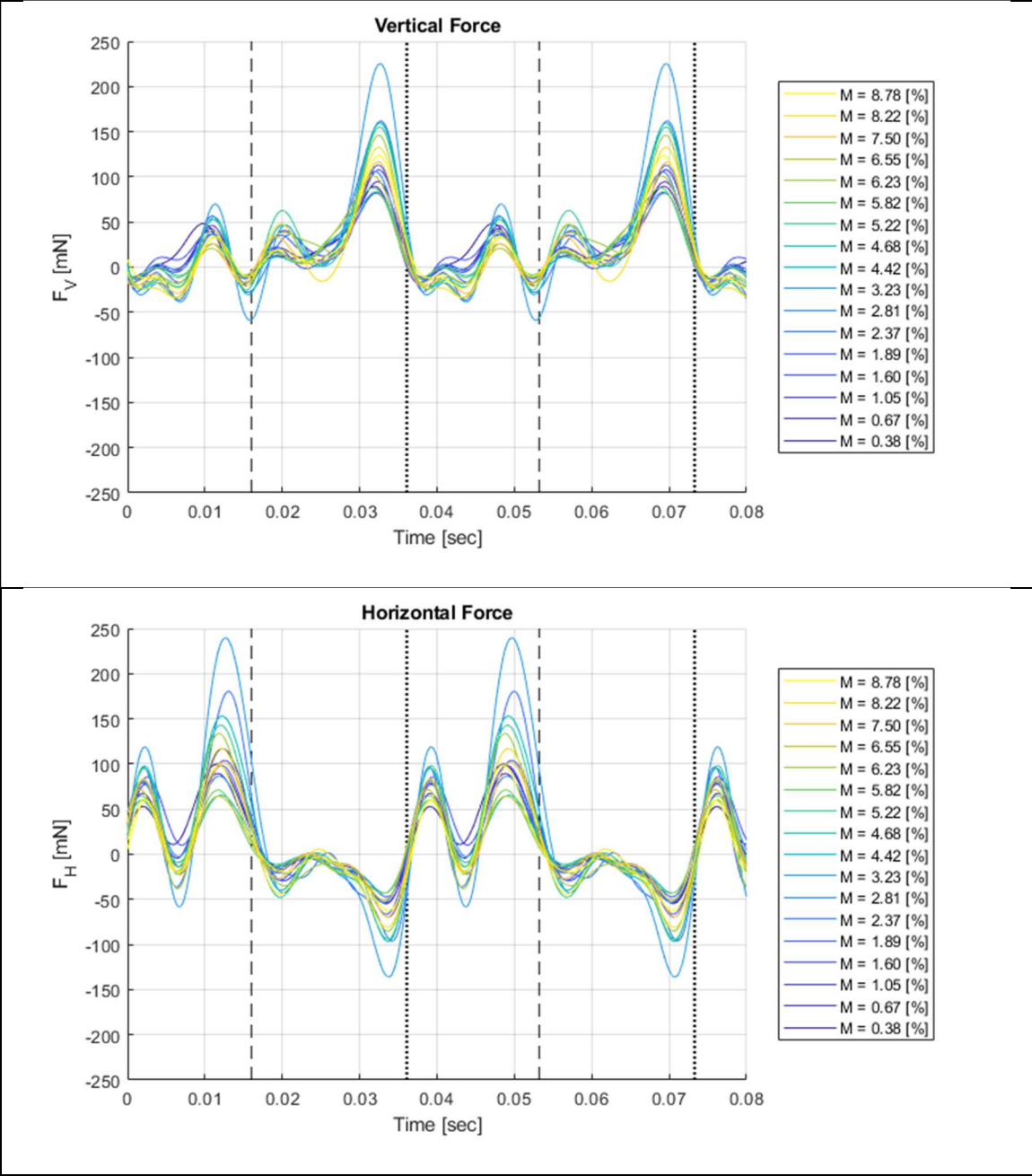
# Sample 20

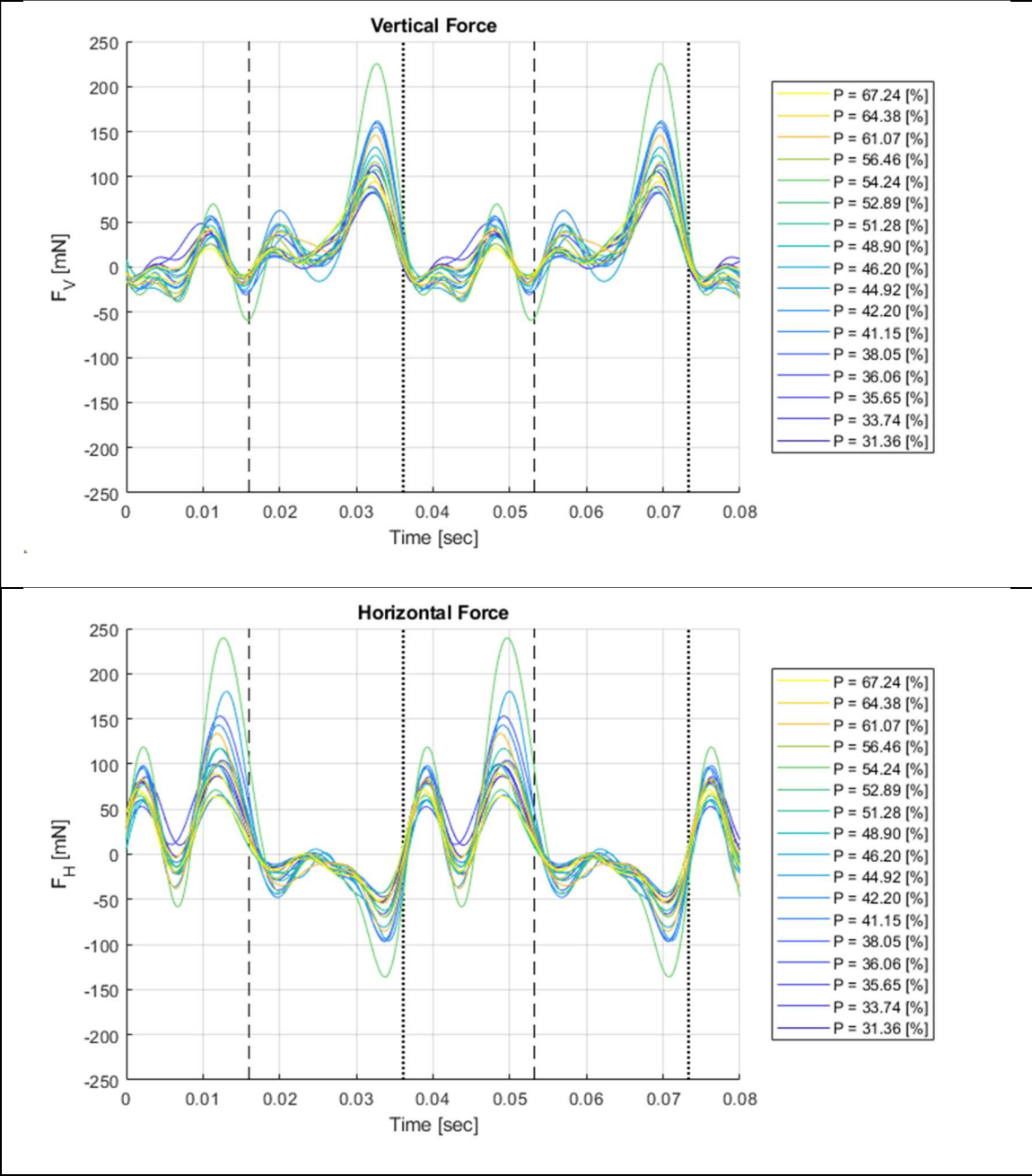


The following are the compiled aerodynamic force results for each wing geometry. The plots are presented in a way such that the effects of each wing geometry parameter has on the aerodynamic forces can be compared.

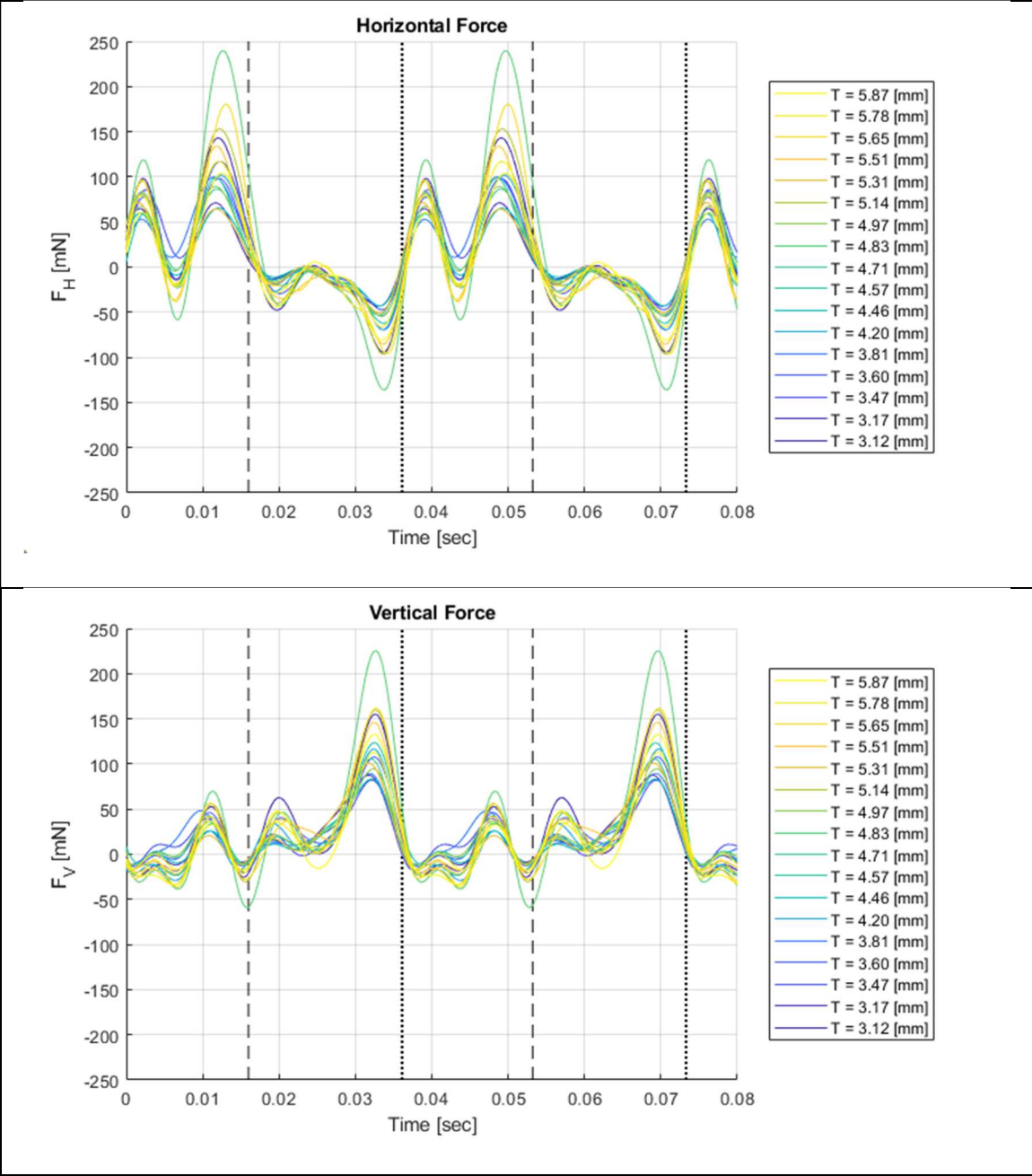








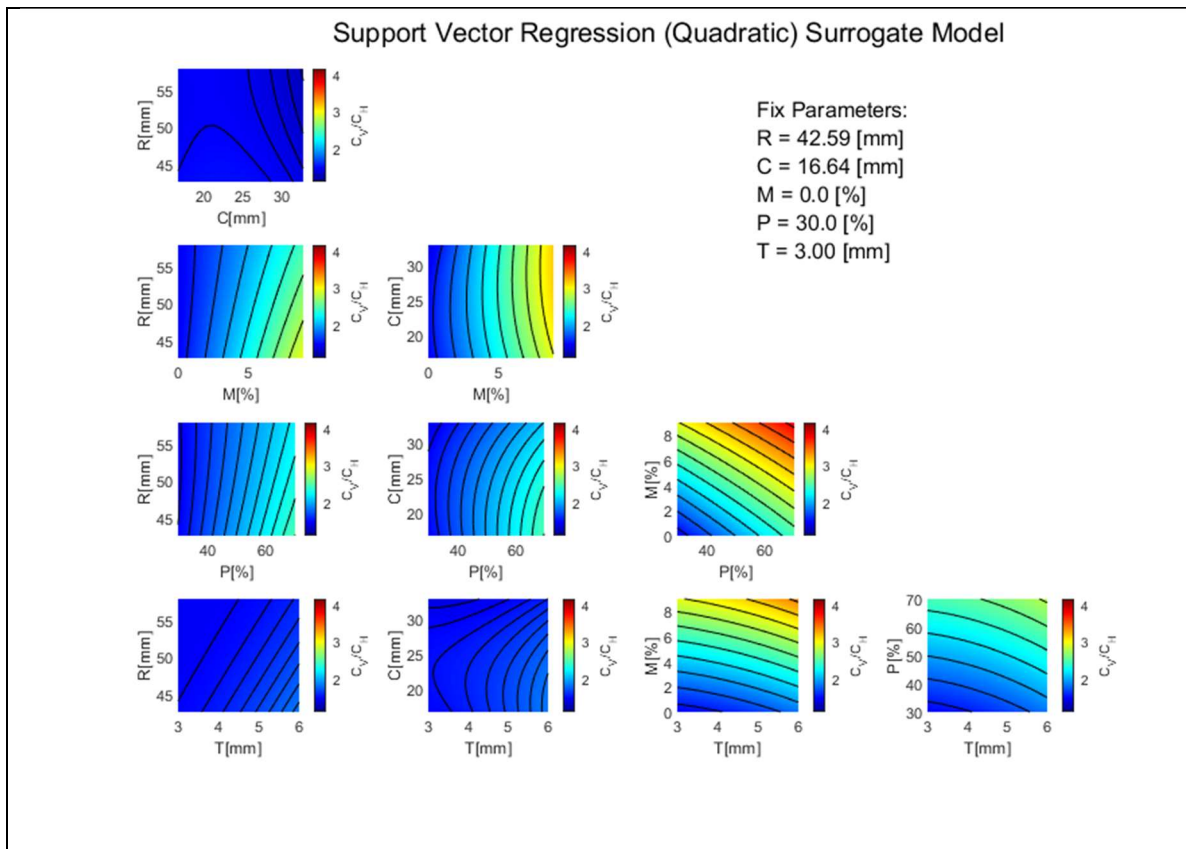




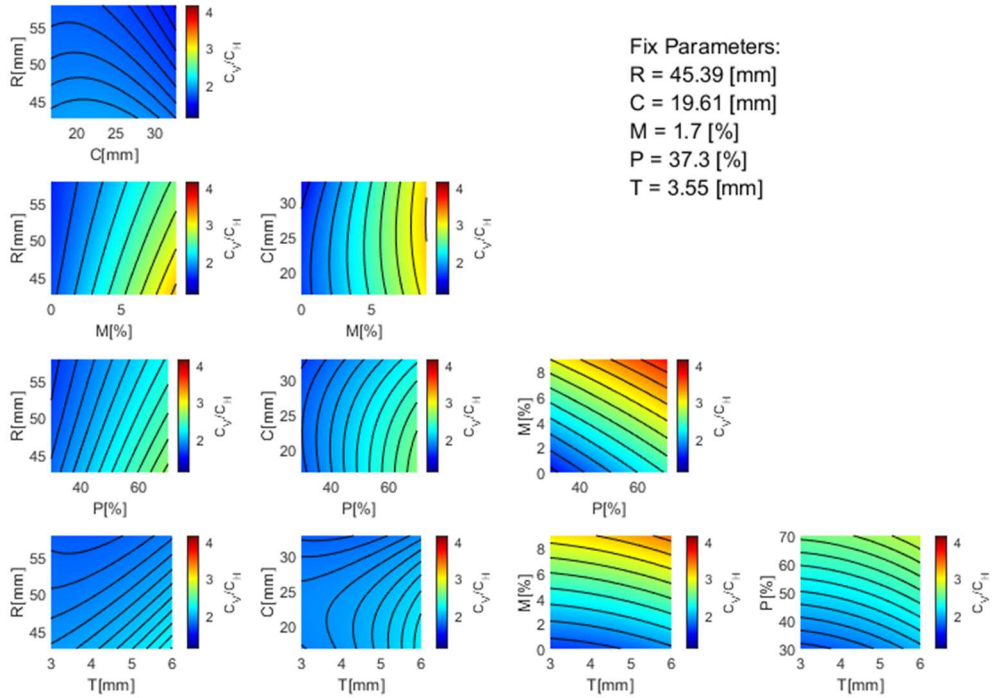
# Appendix C: Quadratic SVR Surrogate Model

## Results

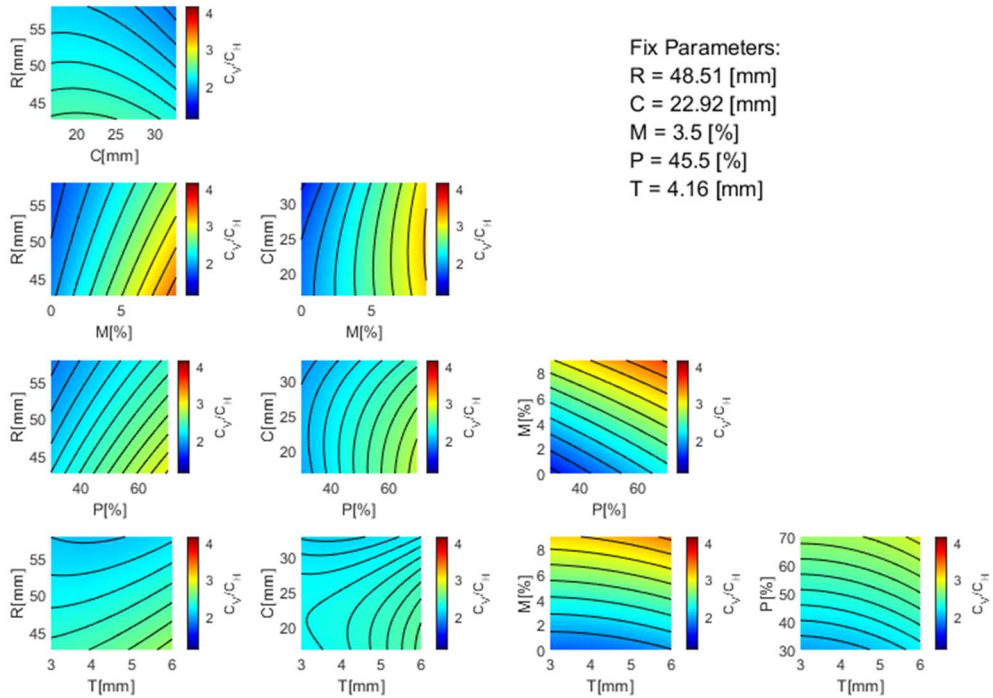
Presented in Appendix C are the frame-to-frame contour maps of the surrogate model lift-to-drag ratio prediction at specified fixed parameter values. After each frame, the fixed parameter values are increased. When two parameter values are presented in one contour map, the other 3 parameters are fixed at the specified fixed values.



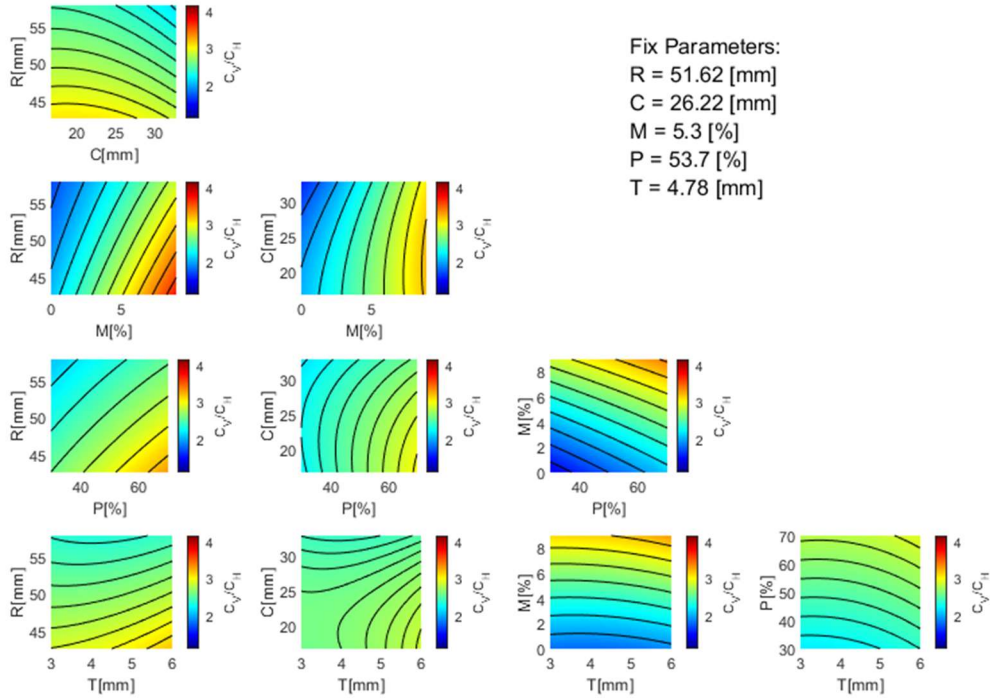
### Support Vector Regression (Quadratic) Surrogate Model



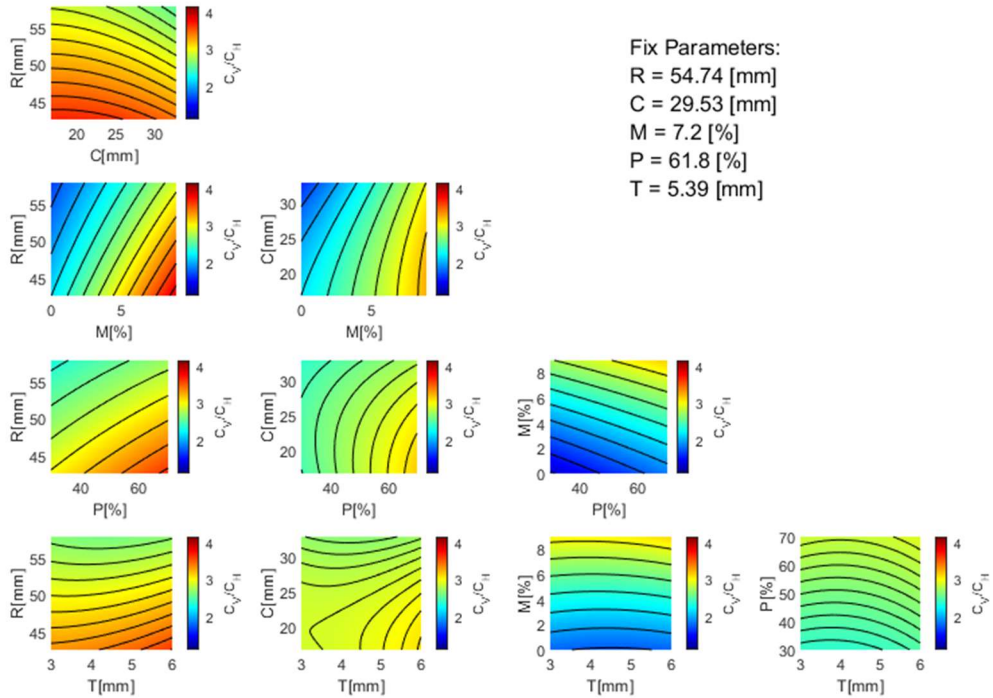
### Support Vector Regression (Quadratic) Surrogate Model



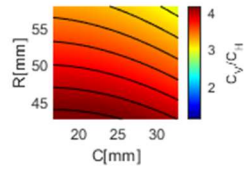
### Support Vector Regression (Quadratic) Surrogate Model



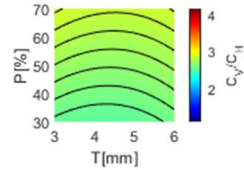
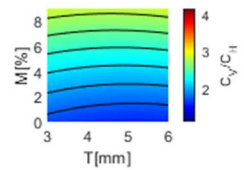
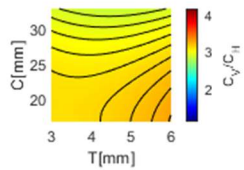
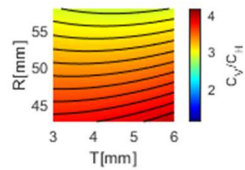
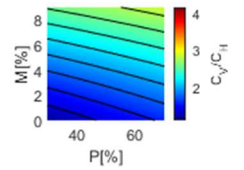
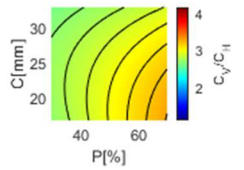
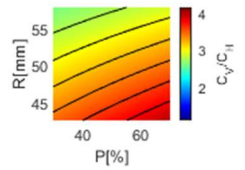
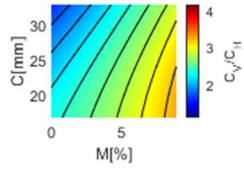
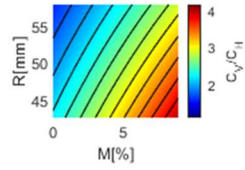
### Support Vector Regression (Quadratic) Surrogate Model



### Support Vector Regression (Quadratic) Surrogate Model



Fix Parameters:  
 $R = 57.85$  [mm]  
 $C = 32.83$  [mm]  
 $M = 9.0$  [%]  
 $P = 70.0$  [%]  
 $T = 6.00$  [mm]



# Bibliography

- [1] O'Hara, R.P., & Palazotto, A.N (2012). "The morphological characterization of the forewing of the *Manduca sexta* species for the application of biomimetic flapping wing micro air vehicles." *Bioinspiration & Biomimetics*, 7(4), 046011.
- [2] O'Hara, R. P. (2012). "The Characterization of Material Properties and Structural Dynamics of the Manduca Sexta Forewing for Application to Flapping Wing Micro Air Vehicle Design." *Theses and Dissertations*. 1057.
- [3] DeLuca, Anthony M. (2013). "Aerodynamic Performance and Particle Image Velocimetry of Piezo Actuated Biomimetic Manduca Sexta Engineered Wings Towards the Design and Application of a Flapping Wing Flight Vehicle." *Theses and Dissertations*. 505.
- [4] Sims, T.W., Palazotto, A.N., & Norris, A. (2010). "A structural dynamic analysis of a *Manduca sexta* forewing." *International Journal of Micro Air Vehicles* 2(3), 119-140.
- [5] Jacobs, E. N., Ward, K.E., & Pinkerton, R.M. (1933). "The Characteristics of 78 related airfoil section from tests in the Variable-Density Wind Tunnel." No. 460. *US Government Printing Office*.
- [6] Willmott, A.P., & Ellington, C.P. (1997). "The mechanics of flight in the hawk moth *Manduca sexta* 1. Kinematics of hovering and forward flight." *The Journal of Experimental Biology*, 200(21), 2705-2722.
- [7] Willmott, A.P., & Ellington, C.P. (1997). "The mechanics of flight in the hawk moth *Manduca sexta* 2. Aerodynamic consequences of kinematic and morphological variation." *The Journal of Experimental Biology* 200(21), 2723-2745.

- [8] Moses, K., Willis, M., & Quinn, R. (2020). “Biomimicry of the Hawk Moth, *Manduca sexta* (L.), Produces an Improved Flapping-Wing Mechanism.” *Biomimetics* 5(2), 25-46.
- [9] Moses, K.C. (2020). *Biomimicry of the Hawk Moth, Manduca sexta (L.): Forewing and Thorax Emulation for Flapping-Wing Micro Aerial Vehicle Development*. (Doctoral dissertation, Case Western Reserve University).
- [10] Moses, K. C., Prigg, D., Weisfeld, M., Bachmann, R. J., Willis, M., & Quinn, R. D. (2018). “Simulating flapping wing mechanisms inspired by the *Manduca sexta* hawkmoth.” In *Conference on Biomimetic and Biohybrid Systems* (pp. 326-337). Springer, Cham.
- [11] Nakata, T., & Liu, H. (2012). “Aerodynamic performance of a hovering hawkmoth with flexible wings: a computational approach.” *Proceedings of the Royal Society B: Biological Sciences*, 279(1729), 722-731.
- [12] Du, X., He, P., & Martins, J. R. (2021). “Rapid airfoil design optimization via neural networks-based parameterization and surrogate modeling.” *Aerospace Science and Technology*, 113, 106701.
- [13] Trizila, P., Kang, C. K., Visbal, M., & Shyy, W. (2008). “A surrogate model approach in 2-d versus 3-d flapping wing aerodynamic analysis.” In *12th AIAA/ISSMO multidisciplinary analysis and optimization conference* (p. 5914).
- [14] Forrester, A.I.J., Keane, A., & Sobester, A. (2008). “Engineering Design via Surrogate Modeling: A Practical Guide.” John Wiley & Sons Ltd.

- [15] Forrester, A. I., Bressloff, N. W., & Keane, A. J. (2006). "Optimization using surrogate models and partially converged computational fluid dynamics simulations." *Proceedings of the Royal Society A: Mathematical, Physical and Engineering Sciences*, 462(2071), 2177-2204.
- [16] Sun, G., & Wang, S. (2019). "A review of the artificial neural network surrogate modeling in aerodynamic design." *Proceedings of the Institution of Mechanical Engineers, Part G: Journal of Aerospace Engineering*, 233(16), 5863-5872.
- [17] Lyzinski, V. (2020). "Cross Validation Resampling." *Introduction to Data Science and Machine Learning*. University of Maryland, College Park. Class Lecture
- [18] Lyzinski, V. (2020). "Supervised Learning." *Introduction to Data Science and Machine Learning*. University of Maryland, College Park. Class Lecture.
- [19] Lyzinski, V. (2020). "Support Vector Machines in for Classification and Regression." *Introduction to Data Science and Machine Learning*. University of Maryland, College Park. Class Lecture.
- [20] Nedungadi, A. (2020). "Governing Equations." *Introduction to Computational Fluid Dynamics*. University of Maryland, College Park. Class Lecture.
- [21] Nedungadi, A. (2020). "Finite Difference Stencils." *Introduction to Computational Fluid Dynamics*. University of Maryland, College Park. Class Lecture.
- [22] Nedungadi, A. (2020). "Consistency, Stability, and Convergence." *Introduction to Computational Fluid Dynamics*. University of Maryland, College Park. Class Lecture.



[23] Byrd, R. H., Gilbert, J. C., & Nocedal, J. (2000). "A trust region method based on interior point techniques for nonlinear programming." *Mathematical programming*, 89(1). 149-185